



## **DISCLAIMER**

This report was prepared as an account of work sponsored by an agency of the United States Government. Neither the United States Government nor any agency thereof, nor any of their employees, makes any warranty, express or implied, or assumes any legal liability or responsibility for the accuracy, completeness, or usefulness of any information, apparatus, product, or process disclosed, or represents that its use would not infringe privately owned rights. Reference herein to any specific commercial product, process, or service by trade name, trademark, manufacturer, or otherwise does not necessarily constitute or imply its endorsement, recommendation, or favoring by the United States Government or any agency thereof. The views and opinions of authors expressed herein do not necessarily state or reflect those of the United States Government or any agency thereof.

This report has been reproduced directly from the best available copy.

Available to DOE and DOE contractors from the Office of Scientific and Technical Information, P.O. Box 62, Oak Ridge, TN 37831; prices available from (615)576-8401, FTS 626-8401.

Available to the public from the National Technical Information Service, U.S. Department of Commerce, 5285 Port Royal Rd., Springfield, VA 22161.

Kinetic Modeling of Petroleum Formation in the Maracaibo Basin

Final Report  
Annex XII

By  
Alan K. Burnham  
Robert L. Braun  
Jerry J. Sweeney  
John G. Reynolds  
Carlos Vallejos  
Sahas Talukdar

July 1992

Work Performed Under Contract No. W-7405-Eng-48

Prepared for  
U.S. Department of Energy  
Assistant Secretary for Fossil Energy

R. E. Lemmon, Project Manager  
Bartlesville Project Office  
P. O. Box 1398  
Bartlesville, OK 74005

Prepared by  
Lawrence Livermore National Laboratory  
P. O. Box 808  
Livermore, CA 94551  
and  
INTEVEP  
S.A., Apartado 76343  
Caracas 1070-A, Venezuela



# Kinetic Modeling of Petroleum Formation in the Maracaibo Basin: A Final Report on Joint Work by LLNL and INTEVEP under Annex XII

Alan K. Burnham, Robert L. Braun, Jerry J. Sweeney, and John G. Reynolds  
Lawrence Livermore National Laboratory  
P. O. Box 808, Livermore, CA 94551

Carlos Vallejos and Suhas Talukdar  
INTEVEP, S.A., Apartado 76343, Caracas 1070-A, Venezuela

## TABLE OF CONTENTS

Abstract.....	2
Introduction.....	3
Background.....	3
Samples.....	5
Atmospheric-Pressure Programmed Pyrolysis.....	6
Programmed Micropyrolysis Kinetics	
Oil Evolution Kinetics	
Gas Evolution Kinetics	
Hydrous Pyrolysis.....	9
General Maturity Trends	
Global Oil and Bitumen Kinetics	
Gas Generation Kinetics	
Detailed Pyrolysis and Expulsion Codes.....	14
PYROL	
PMOD	
Development of a Detailed Pyrolysis Model.....	19
Comparison of Geologic and Laboratory Maturation	
A Detailed PMOD Model for La Luna Source Rock	
Parametric Studies Using PMOD	
Initial Kinetic Modeling of the Maracaibo Basin.....	26
Geologic Modeling Codes	
Initial Paleothermal Histories	
Initial Maturity Calculations and Comparisons	
Testing PMOD with Data from the Maracaibo Basin.....	28
Pore Pressure Modeling in the Maracaibo Basin	
Kerogen and Composition Modeling in the Maracaibo Basin	
Summary and Conclusions.....	35
References.....	37
Tables.....	40
Figures.....	58
Appendix I. Copy of Annex XII	
Appendix II. Theoretical considerations for PMOD	
Appendix III. PMOD chemistry input file for La Luna source rock	

## ABSTRACT

The purpose of this project is to develop and test improved kinetic models of petroleum generation and cracking, pore pressure buildup, and fluid expulsion. The work was performed jointly between LLNL and INTEVEP under Annex XII of an agreement between DOE and the Venezuelan Ministry of Energy and Mines. Laboratory experiments were conducted at both LLNL and INTEVEP to obtain the reaction rate and product composition information needed to develop chemical kinetic models. Experiments at INTEVEP included hydrous pyrolysis and characterization of oils by gas and liquid chromatography. Experiments at LLNL included programmed pyrolysis in open and self-purging reactors, sometimes including on-line gas analysis by tandem mass spectrometry, and characterization of oils by gas chromatography and nuclear magnetic resonance.

As a first step, global hydrocarbon generation kinetics were derived using an activation energy distribution model. These were combined with thermal histories of 80 wells to calculate global maturation across the Maracaibo basin. The thermal histories were initially derived at INTEVEP and were modified slightly at LLNL based on comparison of observed vitrinite reflectance profiles and those calculated from the LLNL EASY%Ro vitrinite reflectance model. Calculated  $T_{max}$  and H/C ratios of the residual kerogen agreed well with observed values, and the calculated fraction of kerogen converted agreed well with the API gravity and sulfur content of oil in Cretaceous reservoirs.

In parallel, a formalism was developed for calculating pore pressures and fluid expulsion. This formalism was first incorporated into PYROL, the detailed LLNL pyrolysis model. The pore pressure-fluid expulsion formalism was tested initially using kinetic parameters for the Green River formation and preliminary kinetic parameters for a generic marine source rock. Although the approach appeared promising, the PYROL code was difficult to modify and use, so a more easily used and flexible code, PMOD, was developed. PMOD enables the user to develop interactively a pyrolysis mechanism that satisfies elemental balance and to automatically calculate many geochemical indicators.

PMOD was used to develop a detailed pyrolysis mechanism from the extensive laboratory data. This mechanism is able to predict yield of bitumen, oil, and gas as a function of time and temperature for such diverse laboratory conditions as hydrous pyrolysis and rapid, programmed, open pyrolysis. Gas species include  $CH_4$ , wet gas,  $CO_2$ ,  $H_2S$ , and  $H_2$ . Oil composition includes sulfur content, H/C ratio, saturate content, API gravity, pristane/phytane ratio, and phytane/ $C_{18}$  ratio.

PMOD calculations were compared to geologic observations for 22 wells in the Maracaibo basin. When permeability parameters are chosen to match calculated pore pressures with measured present day values, the PMOD calculations indicate that organic maturation reactions contribute a significant fraction of the overpressuring during oil generation and early oil cracking. Calculations agreed with observed geochemical maturity parameters of the source rock. The calculated composition of oils in Cretaceous reservoirs below the La Luna formation agreed well with observed compositions as long as it was assumed that the oil matured in the reservoir by experiencing the same thermal history as the source rock from which it came.

## INTRODUCTION

The United States and Venezuela have a mutual interest in improving the ability to predict the occurrence of petroleum in geologic formations. In pursuit of that objective, Lawrence Livermore National Laboratory (LLNL) and INTEVEP, S.A., the research organization of the Petroleos de Venezuela, S.A. (the Venezuelan national petroleum company) have conducted five years of joint research to improve predictive capability for petroleum formation, migration, and overpressuring.

The joint work was started in 1987 under Annex XII of the Implementing Agreement between the U.S. Department of Energy (DOE) and the Ministry of Energy and Mines of Venezuela (MEMV). Annex XII is reproduced in its entirety in Appendix I. Briefly, the work outline described experimental tasks that would be conducted mostly independently at LLNL and INTEVEP and prescribed that the data from these experiments would be combined jointly to develop a kinetic maturation model for the La Luna source rock. The kinetic model would then be jointly tested by comparison to geological and geochemical evidence in the Maracaibo Basin. The primary expertise brought to this project by LLNL was in temperature-programmed pyrolysis measurements, development of chemical kinetic models, and deduction of paleothermal histories. INTEVEP brought an expertise in hydrous pyrolysis and petroleum analysis and a data base of geochemical measurements in the Maracaibo Basin.

The Annex XII work was designed to develop kinetic models of petroleum generation and expulsion for the La Luna Formation like those developed at LLNL during 1980-1985 for the Green River Formation and to test the models in the Maracaibo Basin. It expanded on work from the 1970's, in which the role of time and temperature for the conversion of kerogen to petroleum was generally recognized, although the chemical kinetic models describing it were fairly primitive. In the mid 1980s, LLNL tested the ability of chemical kinetics developed for *in-situ* retorting of Green River Formation oil shale to predict the generation of petroleum in the Uinta Basin (Sweeney *et al.*, 1987). Not only did the kinetic model predict the occurrence of petroleum, it also predicted some aspects of oil composition, suggested that overpressuring was related to petroleum generation, and indicated that most of the petroleum had been expelled from mature source rocks. At the same time, an INTEVEP study (Talukdar *et al.*, 1986) detailed the generation of petroleum in the Maracaibo Basin, indicating that most of the petroleum was generated from the La Luna formation. Furthermore, geochemical and petrographic observations indicated that extensive migration of oil occurred through microfractures.

This report documents the experimental and modeling work conducted under Annex XII. Much of the work has already been published in scientific journals, and relatively more emphasis will be placed on aspects that have not been published. This report demonstrates that the Annex XII work has been a major contributor to general advances in predicting the generation of petroleum and its expulsion from the source rock.

## BACKGROUND

This section outlines some of the general issues and the underlying theoretical approaches used in the Annex XII work. At the beginning of the work, there were significant disagreements concerning which laboratory experiments (if any) could lead to quantitative

predictions of the timing of oil generation, what the primary mechanism of oil expulsion from the source rock was, and how to deduce paleothermal histories.

Once it was demonstrated conclusively by Philippi (1965) that petroleum comes primarily from the thermal transformation of kerogen, many kinetic models have been proposed (Waples, 1984). Some were based on both field and laboratory observations indicating the transformation was a serial process whereby kerogen first decomposed to bitumen (a relatively high-molecular weight, soluble material), which subsequently decomposed to oil and gas. Others were based on the recognition that the heterogeneity of kerogen often prevented the use of first-order rate laws for oil and gas generation. In this case, the distribution of reactivity is described by multiple parallel reactions having a common frequency factor,  $A$ , and a distribution of activation energies,  $E$ . Although any given worker usually emphasizes either the serial or parallel characteristics of the reaction, the two different approaches are not mutually exclusive. Both concepts were used in the Annex XII work.

The activation energy distribution kinetic model is outside traditional chemical kinetics. Because it will be used extensively in this report, a brief explanation is appropriate. Although there is undoubtedly a distribution in both the frequency factors and activation energies involved in pyrolysis of complex organic matter, it is difficult in practice to determine both distributions. Therefore, it is customarily assumed by fossil fuel kineticists that all the reactivity distribution can be ascribed to a distribution in activation energy. The distribution can take any continuous or discrete form. The two most common distributions are (a) Gaussian and (b) discrete with 1 or 2 kcal/mol spacing. The total potential of the reaction is then partitioned across this distribution. The overall reaction rate or extent of reaction is calculated merely by summing the first-order contributions over the distribution.

In the early phases of the Annex XII work, a computer program, called KINETICS, was developed at LLNL that could derive the activation energies from a wide variety of laboratory data. The continued development of this program was supported by a combination of Annex XII funds with those from DOE Basic Energy Sciences and a group of industrial sponsors. Further details of the KINETICS program and the methods of analysis are given elsewhere (Braun and Burnham, 1990b; Braun *et al.*, 1991). The KINETICS program has been acquired by about 15 oil companies and several public research organizations. For the purposes of this report, it is necessary only to note that the activation energy distributions can be either Gaussian or discrete and that the Gaussian distributions can be derived either by rigorous nonlinear regression analysis or by an approximate procedure that uses the width of the reaction profile and the shift of  $T_{\max}$  (the temperature of maximum reaction rate) with heating rate. The latter approach is much faster and generally just as accurate.

Once oil is generated, it must be expelled from the source rock in order to migrate to a reservoir, except in special cases where the fractured source rock serves as the reservoir rock. There have been many models of oil migration proposed, including dissolution in water, diffusion through water or kerogen, pressure driven flow through porosity or kerogen, and capillary action (McAullife, 1979). Based on the observation of bitumen-filled microfractures in the La Luna source rock (Talukdar *et al.*, 1986), it was assumed at the outset that pressure-driven flow of a continuous oil phase was the most important primary migration mechanism. It was further assumed that the flow could proceed either through existing porosity, or if the pressures built up to exceed some high fraction of lithostatic pressure, through the resulting fractures.

In order to use either the generation or expulsion models, it is necessary to have a paleothermal history for the source rock. The primary assumption used in all Annex XII work for deriving paleothermal histories is that conduction of heat from the mantle is the primary means of heating sediments. This assumes that transport of heat by fluids, generation of heat within the sediments by radioactivity, and generation or absorption of heat by chemical reactions are negligible. The sediments constitute an insulating layer over the hot basement rocks. The thermal conductivities of the rocks are assumed to depend on porosity and temperature, which are a function of depth. Many regions of interest have undergone uplift and erosion, and thus are cooler now than at some point in the past. In this case porosity is also a useful indicator of deepest burial. It is of great general interest to develop techniques to quantify paleotemperatures from the present-day condition of the rocks. Analysis of geothermometers such as vitrinite reflectance is one way to accomplish this.

An unplanned advance partially due to the Annex XII work was a new model of vitrinite reflectance maturation. Vitrinite is an organic maceral originating from woody plant material. It is the major component of most coals and a minor component of many sediments. As vitrinite is heated underground, it becomes more carbonaceous and more reflective of light. Vitrinite reflectance has become widely used as an indicator of paleothermal histories. Our model built on historical observations that reflectance correlates well with both the carbon content and H/C ratio of the vitrinite. Our major advance was to derive a kinetic model which could predict vitrinite composition, hence reflectance, at both laboratory and geologic time scales (Burnham and Sweeney, 1989). This model and a subsequent simplification (Sweeney and Burnham, 1990) were useful in deriving paleothermal histories in the Maracaibo Basin.

## SAMPLES

Samples for the Annex XII work were supplied by INTEVEP. Most experiments used one of four samples from the La Luna Formation, the principal source rock of the Maracaibo basin. Properties of these four samples are given in Table 1. Initial experiments at LLNL were done on sample QL7, which is a particularly rich, immature sample that INTEVEP had used in earlier hydrous pyrolysis samples. Unfortunately, not much of that sample was available at the beginning of the Annex XII work. Similarly, the supply of 26D2, a moderate grade sample, had been expended. Therefore, INTEVEP attempted to obtain another rich, immature sample. That attempt was largely unsuccessful. A second 26D2 sample, labeled 26D2', was substantially lower in organic content than the initial sample. Ultimately, the second sample was useful for describing phenomena for the lean end of the spectrum of source rock richness. The final sample investigated, QLN, is reasonably close to the proposed average richness of the La Luna Formation. In addition to the La Luna results, prior hydrous pyrolysis data was supplied for JGE28, a sample from the Querecual Formation from eastern Venezuela, the analog of the La Luna in that basin.

## ATMOSPHERIC-PRESSURE PROGRAMMED PYROLYSIS

Pyrolysis of oil shales at a constant heating rate and atmospheric pressure has been commonly used at LLNL to derive oil and gas generation kinetics. Article 2, Section B, Task 1 of Annex XII prescribes experiments of the Burnham-Singleton (1983) type in a self-purging reactor. These experiments were scaled back considerably from the initial plans. The apparatus originally proposed to do high-pressure kinetic measurements was disassembled to provide space for other experiments on oil shale processing prior to receiving funds for the Annex XII. During the same time frame, a major advance in kinetic technique was made that was not available during the drafting of the work statement (Burnham *et al.*, 1987a). These two developments caused the work plan to be modified by replacing the high-pressure kinetic experiments with programmed micropyrolysis experiments, which had the potential of being more generally useful. The initial programmed micropyrolysis measurements were made on modified Rock Eval II instruments at other laboratories on a service basis, and later measurements were made on a Pyromat II instrument at LLNL. The self-purging reactor was reconstructed in simplified form; oil evolution kinetics were measured for two samples, QL7 and 26D2', at 2 °C/min and 2 °C/h, atmospheric pressure only.

Article 2, Section B, Task 3 of Annex XII prescribes gas evolution kinetics experiments at LLNL. The original intent was that several samples would be examined, but a shortage of organic-rich sample prevented that from being accomplished. Only the QL7 sample was investigated, with measurements at 1 and 10 °C/min. Unfortunately, because of experimental problems, the number of experiments originally envisioned for several materials were needed for this one material to get acceptable data.

Schematic diagrams of the three experimental reactors are given in Figure 1.

**Programmed Micropyrolysis Kinetics.** Initial Rock Eval II kinetic data were obtained from Alain Samoun of Lab Instruments, Inc., and Daniel Jarvie of Humble Instruments and Services. The Lab Instruments data consisted of two sets. The first was obtained in October, 1987, for sample QL7 only and was reported in the 1987 annual report (Burnham *et al.*, 1987b). The second set was obtained in July, 1988, for both QL7 and 26D2'. Data for both samples were obtained in July, 1988, from Humble Instruments. The results for the Humble Instrument set and second Lab Instruments set were reported in the 1988 annual report (Braun *et al.*, 1988). In all cases, sample AP22 was run concurrently to calibrate the temperature according to the original LLNL procedure (Burnham *et al.*, 1987a; 1988). All computer analyses were performed at LLNL.

The rate parameters derived from these early kinetic measurements are summarized in Tables 2 and 3. The temperature correction shown is that derived from the concurrent AP22 measurements so that the shift in  $T_{max}$  for that sample is consistent with  $A = 1 \times 10^{13} \text{ s}^{-1}$  and  $E = 51 \text{ kcal/mol}$ . There are two general conclusions from these first measurements. First, the principal activation energy for hydrocarbon generation is close to 50 kcal/mol. Second, the QL7 and 26D2' samples have very similar kinetics. The absolute accuracy of the kinetic parameters depends on the validity of the temperature calibration procedure, and the degree of similarity between the two samples is limited by the experimental precision.

In early 1989, a Pyromat II apparatus was acquired from Lab Instruments, Inc. This instrument had a more uniform temperature in the sample region than the Rock Eval

instrument and allowed placement of a thermocouple directly in the sample, as shown in Figure 1. In 1989, kinetic parameters were derived for sample QL7 with the Pyromat II. These were used in preliminary form in the first report of oil generation of petroleum in the Maracaibo Basin (Sweeney *et al.*, 1990). Subsequent refinements in the temperature calibration procedure produced slightly different results, which were reported along with kinetic parameters for other samples (Braun *et al.*, 1991). These parameters are also given in Table 4, along with results for samples 26D2' and QLN. One immediately notices that the activation energy for the QL7 sample is slightly higher than that measured earlier on the Rock Eval instrument, but the parameters for the whole 26D2' sample are very similar to previous results. We assume that the most recent parameters are the most accurate because of technique refinement and more accurate temperature measurements. The rates calculated from the most recent discrete model parameters are compared in Figure 2 to the data from which they are derived.

One problem with the kinetics for the 26D2' sample is that about three-fourths of the organic matter in that sample is bitumen rather than kerogen. The presence of bitumen often causes problems with the kinetic experiments at low heating rates because some of the high-molecular-weight organic matter tends to bleed through the system and appears either in a large hump prior to kerogen pyrolysis or as a higher temperature peak if it collects in a cold spot before the detector. A detailed discussion of these problems is given elsewhere (Reynolds and Murray, 1991).

The bitumen content of sample 26D2' raises the issue of how to treat a bitumen intermediate in a kerogen decomposition network. A vacuum residuum was prepared from Boscan oil, a very immature oil from the Maracaibo Basin, and the residuum was further separated into maltenes and asphaltenes by isooctane precipitation. Pyrolysis kinetics were determined for all three samples by Pyromat, and the results are shown in Figure 3. The whole residuum and the maltenes suffer from low temperature contributions that are due to either remaining volatile material or labile bonds. The kinetics of the asphaltenes are very similar to that for the La Luna source rock. It is concluded that, to a first approximation, the kinetics for devolatilization of a high molecular weight intermediate between kerogen and oil are equivalent to those for kerogen devolatilization itself.

**Oil Evolution Kinetics.** The detailed procedure for these measurements and the results for sample QL7 have been published elsewhere (Burnham, 1991). Briefly, 30-50 g of powdered sample was pelletized by a press, and the sample was welded into the reactor. The reactor was heated in a 3-zone furnace with programmable controller. The oil and water evolved were collected in a graduated tube below, and the volumes of water and oil recorded as a function of time and temperature. Material balance information for the QL7 and 26D2' experiments is given in Table 5.

The temperature-conversion curves for these experiments are shown in Figure 4, and kinetic parameters derived for sample QL7 are given in Table 6. A kinetic analysis for the 26D2' sample is not reported because the data show a major influence of mass transport on the observed evolution rates. Also shown in Figure 4 are calculated evolution curves from the micropyrolysis kinetics.

There are several related conclusions that can be drawn from Figure 4 and Tables 4 and 6. First, kinetic expressions derived for sample QL7 from Pyromat and the self-purging reactor are similar to each other. However, the activation energy from the self-purging

reactor is slightly higher. This causes the curve calculated from the Pyromat kinetics to predict a slightly lower oil evolution temperature at 2 °C/h than observed. This difference is even more pronounced for the 26D2' sample. In this case, it appears that evolution of oil below 350 °C is severely inhibited by some process. We have proposed in the past (Burnham *et al.*, 1988; Burnham and Braun, 1990) that inhibition of volatility becomes more pronounced at lower experimental temperatures, and this causes the apparent activation energy to be higher than the true value for a given extent of breakdown of the organic matter. The predicted effect on the activation energy is enhanced under self-purging conditions. The 26D2' sample may be an extreme case because the low organic content enhances the role of adsorption on mineral matter as a means to decrease product volatility. Because of this volatility effect, we have suggested that all the activation energies of samples with high organic content, such as QL7, should be reduced by 2 kcal/mol, with a corresponding change in the frequency factor so that the rate constant is unchanged at 450 °C. That is easily accomplished by dividing the frequency factor by two for every one kcal/mol decrease. For the two kcal/mol decrease, the divisor of the frequency factor is 2<sup>2</sup>, or 4.

Sufficient quantity of oil was collected for sample QL7 that further oil characterization by gas chromatography (GC) and nuclear magnetic resonance (NMR) was possible. Results are summarized in Table 7. Some of these results will be discussed during the comparison to hydrous pyrolysis experiments.

**Gas Evolution Kinetics.** These experiments are conducted under conditions more similar to the Pyromat than the self-purging reactor. The powdered shale is pyrolyzed in a quartz tube swept by a constant flow of argon. Molecules greater than about C<sub>9</sub> are retained in a trap held at 140 °C. The gas composition was analyzed by a triple-quadrupole mass spectrometer (TQMS) as described in more detail elsewhere (Reynolds *et al.*, 1990). Species monitored are given in Table 8. The identification of acetic acid is tentative and could include contributions from isopropanol. Sample temperature was measured by a type K thermocouple. The thermocouple was well-calibrated for the 10 °C/min experiment but not for the experiment at 1 °C/min. Therefore, exact chemical kinetics could not be determined. Instead, the temperatures of the 1 °C/min experiment were adjusted so that the temperatures of complex hydrocarbons were consistent with those from the Pyromat instrument.

Before proceeding to the kinetic analysis, a few general observations concerning the gas evolution process would be useful. Evolution profiles for 13 species are shown in Figure 5. The hydrocarbon profiles are similar to each other, except for methane and ethene, which tend to evolve at higher temperatures. T<sub>max</sub> for the thiophenes, acetic acid, and mercaptans (not shown) tend to be lower than for the hydrocarbons, and di- and tri-atomic molecules tend to have complex evolution profiles portraying multiple generation mechanisms. Most prominent is the CO<sub>2</sub> peak due to calcite decomposition and an associated CO peak at slightly higher temperature due to gasification of residual carbon by the carbonate CO<sub>2</sub> (CO<sub>2</sub> + C → 2CO). In this temperature range, the water-gas shift reactions (H<sub>2</sub>O + CO = H<sub>2</sub> + CO<sub>2</sub>) is important, so the evolution profiles for H<sub>2</sub> and H<sub>2</sub>O are affected. The expanded profile for CO<sub>2</sub> has two small peaks on a broader background, but the sources are not known.

Kinetic parameters were derived for major species of interest. The C<sub>2</sub>-C<sub>4</sub> components have been lumped into a single species for modeling purposes. In preliminary regression analyses, the frequency factor was a variable in the minimization process. Except for acetic acid (where the data are very noisy) and H<sub>2</sub>S, the derived frequency factors for the various

species were similar. In fact, limitations in the data preclude any conclusion that the frequency factors are significantly different, so for convenience during modeling, a second set of parameters were derived by fixing the frequency factor at  $3 \times 10^{13} \text{ s}^{-1}$ , the value determined for total hydrocarbons from Pyromat data. These are given in Table 9 and comparisons between observed and calculated rates are given in Figure 6. This second set of kinetics requires that the progression of the reaction is the same at laboratory and geological conditions. Although this is not necessarily the case, it is justified by the likelihood that the differences in frequency factors are merely statistical variations caused by the broad minimum in regression space. The relative validity of the two sets of kinetic parameters is a matter of continuing research. The implications of the two sets for methyl-thiophene and hydrocarbons are discussed later in the detailed model development section.

## HYDROUS PYROLYSIS

Article 2, Section A of Annex XII outlines a series of sealed-bomb experiments and product analyses to be conducted at INTEVEP. The experimental conditions were understood to be for hydrous pyrolysis, where sufficient water is added to the sealed-bomb so that the source rock is covered by liquid water during pyrolysis (Lewan *et al.*, 1979; Lewan, 1985). This enables oil and gas that are expelled from the rock to be physically separated from the rock by buoyancy as in nature.

Data for five sets of hydrous pyrolysis experiments are given in Tables 10-15. The first three data sets were taken prior to Annex XII work, but were included because of their direct relevance. For example, the second data set (Table 11) comes from sample QL7, on which most of the LLNL experiments were conducted. No distinction was made between expelled oil and extracted bitumen in the early INTEVEP experiments. In the latter two data sets, HPC and HPN, expelled oil and extracted bitumen were recorded separately, which enables further tests of kinetic methods. For example, Lewan (1985) has proposed that the mass of expelled oil during hydrous pyrolysis follows first-order kinetics. In addition, the HPC and HPN experiments used a variety of pyrolysis times in an attempt to test the first-order hypothesis. To keep the total number of experiments within bounds, a smaller number of temperatures were used.

Quantities of interest from the hydrous pyrolysis experiments include the kinetics of oil and bitumen formation as well as the relationship between extent of conversion and maturity indicators such as Rock Eval parameters and oil composition. Pyrolysates were characterized by elemental analysis and gas chromatography. Gas analysis was obtained for some experiments. This section will proceed first with a general discussion of maturity trends, followed by a global kinetic analysis of oil and bitumen generation (including a comparison to Pyromat kinetics) and a comparison of gas generation in hydrous pyrolysis and the TQMS experiments.

**General Maturity Trends.** Since hydrous pyrolysis is a reasonable simulation of the natural maturation process, it would be useful to construct maturity trends from the hydrous pyrolysis data in a form that can be used for eventual comparisons with geologic observations. Important parameters are the gas/oil ratio, the composition of the oil, the

efficiency of oil expulsion, and the elemental composition and Rock-Eval parameters of the remaining kerogen.

The three pre-existing sets of hydrous pyrolysis data provide an initial reference for the temperature range of maturation under the common conditions of 72-h pyrolysis at various temperatures. Figures 7-9 indicate that the maximum bitumen yield is at 310 °C for the La Luna samples (QL7 and 26D2) and about 330 °C for the Querecual sample (JGE28). Although the precise relationships are different for each sample, the polar fraction (resins plus asphaltenes) tends to decrease with maturity, the aromatic fraction tends to increase with maturity, and the saturate fraction tends to go through a maximum concentration at a temperature greater than the maximum bitumen yield. The corresponding plots for experiments HPC and HPN conducted under Annex XII are not possible because time was varied in addition to temperature, but similar maturity trends are evident in Tables 13 and 14. However, the separate report of resins and asphaltenes for the HPN series indicates that the decrease in polar content is really due to a decrease in asphaltene content, while the resin content remains roughly constant. If one considers the asphaltenes to be slightly modified kerogen, they represent potential oil, while the resins are probably mostly heteroaromatic material. These trends will be discussed in further detail in the section dealing with development of a detailed compositional kinetic model.

When considering source rock maturity, a maturity indicator that depends on the kerogen properties is more desirable than one that depends on bitumen properties because the latter depend on the extent of expulsion and possible contamination by migration from other regions of different maturity. Three parameters of general use are the H/C ratio in the kerogen, the Rock-Eval  $T_{max}$ , and the Rock-Eval hydrogen index.  $T_{max}$  values are the most commonly available of these three for the hydrous pyrolysis experiments. Figure 10 shows the dependence of  $T_{max}$  on pyrolysis temperature for 72-h pyrolysis.  $T_{max}$  increases sharply for  $T$  greater than about 330 °C. Figure 11 shows the relationship among the Rock-Eval  $T_{max}$ , Rock-Eval S2, and kerogen H/C ratio. Not all parameters are available for all experiments. About 90% of the drop in pyrolysis potential (S2) occurs as  $T_{max}$  increases from 430 to 440 or 450 °C. At the same time, the H/C ratio drops from 1.25 to about 0.65. Most of the remaining pyrolysis potential decreases by  $T_{max} = 550$  °C, and the H/C ratio of the residual kerogen drops to 0.5. The drop in H/C per unit decrease in S2 is smaller for  $T_{max} < 450$  °C than for  $T_{max} > 450$  °C. This is because the first stage corresponds to generation of mostly oil while the latter stage corresponds to generation of mostly methane.

Since  $T_{max}$  is the only one of three indicators available for all experiments, it provides a common reference for other parameters. Figure 12 shows the relationship of three biomarker ratios to  $T_{max}$ . The left-hand figures are for the three experiments where total bitumen is collected. The right-hand figures are for the expelled oil and extracted bitumen from the HPC-series experiments. Although the absolute values are different for each sample, both pristane/ $C_{17}$  and phytane/ $C_{18}$  decrease sharply for  $T_{max} < 450$  °C. The leveling off at higher maturity may be more a reflection of detection limit than a true trend. The initial decrease is due primarily to dilution by generation of normal alkane. The pristane/ $C_{17}$  ratio tends to drop less, presumably because additional pristane is generated during pyrolysis, while not much additional phytane is formed. Therefore, the pristane/phytane ratio tends to increase as  $T_{max}$  increases from 430 to 450 °C, but there is a great deal of scatter for  $T_{max} > 450$  °C. In fact, Figure 13 indicates that most of the bitumen has been cracked by a  $T_{max}$  of 450 °C. As also shown in Figure 13, the ratio of expelled oil to total bitumen reaches its

maximum value by  $T_{max}$  of 450 °C, indicating that oil cracking is at least as important as additional expulsion after that point. There is no clear difference between the biomarker ratios in the expelled and extracted phases for the HPC series. The possibly lower values of the pristane/phytane ratio in the extracted bitumen could be due to a vapor-pressure-dependent expulsion or recovery effect.

Since most of the important processes occur over a fairly small range of  $T_{max}$ , it would be more valuable to have the corresponding relationships versus Rock Eval pyrolysis potential. Figure 14 shows the ratio of expelled oil to total bitumen for the HPC and HPN series experiments. The transformation ratio (TR) was calculated two ways. For the HPN series, it was calculated from the hydrogen index via

$$TR = (1 - HI / HI_0) / (1 - HI / 1200) \quad (1)$$

and from the S2 directly via

$$TR = 1 - S2 / S2_0 \quad (2)$$

Only the second equation was used for the HPC series because residual TOC measurements were not available, but this is not a problem because the two methods agree well for the HPN series. Figure 14 shows that the expulsion from the two samples is quite different. For the lean, bitumen-rich 26D2' sample, the expulsion is almost linear with TR. For the more typical QLN source rock, most of the expulsion occurs after the TR exceeds 0.7.

**Global Oil and Bitumen Kinetics.** As a first step, the disappearance of TOC and the appearance of bitumen for sample QL7 were analyzed for 1st-order rate parameters by linear and nonlinear regression. The linear regression approach used the equation

$$\ln(-\ln(1-x)/t) = \ln A - E/RT, \quad (3)$$

where  $x$  is the extent of reaction. In effect, a 1st-order rate constant is calculated from each experiment, and  $A$  and  $E$  are calculated from the intercept and slope, respectively, of an Arrhenius plot. The nonlinear regression analysis used the program KINETICS.

Both the linear and nonlinear analyses first required a calculation of  $x$ . For TOC, it was calculated by using

$$x = \{ 11.25 - TOC / [1+(11.25-TOC)/100] \} / 6.4, \quad (4)$$

where 11.25 is the average initial wt % TOC, TOC is the value for the reacted rock after extraction, the quantity in the brackets is an approximate correction for the weight change in the rock during pyrolysis, and 6.4 is the wt % of original TOC that can be converted, chosen so that the residual TOC at peak bitumen generation is reasonable. The extent of conversion for bitumen yield was calculated by first subtracting the initial bitumen content and then dividing by the maximum bitumen increase.

Several sets of kinetic parameters were derived in this manner. It was discovered that the linear regression parameters were very sensitive to which data points were used in the regression and, for the TOC, the value assumed for convertible TOC. Changes in activation

energy of more 20 kcal/mol were obtained for different, apparently reasonable assumptions. Parameters determined from the conversion data by nonlinear regression seemed to be less sensitive. Only they are reported in Figures 15 and 16, which compare observed and calculated TOC and bitumen yields, respectively, for sample QL7. Even so, it is important to realize that neither set of kinetic parameters, and especially those from TOC, are well constrained. Therefore, one final set of parameters was determined for bitumen generation by constraining  $A$  to  $3 \times 10^{13} \text{ s}^{-1}$  as for the gas evolution data. The resulting activation energy of 49270 cal/mol is between those given in Figures 15 and 16.

Kinetic parameters derived from sample 26D2 were even more variable, with activation energies ranging from 22 to 87 kcal/mol. Therefore, only a comparison of the QL7 kinetics with the 26D2 data is presented. Figure 17 shows that although the overall formation is described well by the QL7 kinetics, there is a slower initial formation rate of additional bitumen than predicted. In fact, this effect may be due either to experimental precision related to the high levels of native bitumen or due to secondary destruction reactions that get a head start for this sample. For comparison, bitumen formation from sample JGE28 does not agree well with the QL7 kinetics because bitumen yield has a maximum about 20 °C higher.

For the HPC series of experiments on sample 26D2' and the HPN series of experiments on sample QLN, expelled oil was measured separately from extracted bitumen. Even so, the expelled oil and extracted bitumen from the HPN and HPC data do compare well to the earlier experiments. For the HPN set, considering only the 72-h experiments sets, the maximum yield of bitumen plus oil occurs at 310 °C as in the earlier experiments. For the HPC set, the sum of bitumen and oil does not go through a maximum. The organic matter in sample 26D2' is mostly bitumen. Consequently, the sum is roughly constant until the high temperature decline due to cracking to gas and residue becomes major, but the decline is consistent with that observed for other samples.

Figure 18 gives a quantitative comparison of the QL7, 26D2, and HPN hydrous pyrolysis experiments at 72 h with three sets of kinetic parameters. To facilitate the comparison of rocks with different organic contents, the quantity plotted is the total bitumen minus the initial bitumen. For this comparison, the term bitumen for the HPN experiments means expelled oil plus extracted bitumen so it is comparable to the total extract for experiments where expelled oil was not collected separately. One can easily see that the best agreement with experiment is for the solid curve, which was calculated from the bitumen generation kinetics for sample QL7 derived by constraining  $A$  to  $3 \times 10^{13} \text{ s}^{-1}$ . The curve calculated from the TOC-disappearance kinetics predicts too much reaction in the early stages, reflecting either their greater uncertainty or the generation of a non-bitumen product such as  $\text{CO}_2$ . On the other extreme, the Pyromat kinetics are clearly too slow after the first stages of the reaction. An inspection of the expelled oil formation data in Tables 13 and 14 indicates that the expelled oil maximizes at a higher temperature than the total bitumen, so at least qualitatively, the Pyromat kinetics appear to be a better indicator of expelled oil formation than total bitumen. This agrees with a similar comparison for Posidonia shale from Germany (Burnham, 1990).

The second topic of interest is secondary cracking reactions. One way to consider cracking is the disappearance of total bitumen. For 72-h pyrolysis, the yield decreases systematically with temperature for temperatures greater than 310 °C, eventually becoming less than the original bitumen content. A second way to consider cracking is the disappearance of expelled oil. Both cracking reactions are complicated by the fact that they

are serial reactions, i.e., the concentration of the reactant is not at a maximum at time zero. They are also complicated by presence of unreactive or slowly reacting components, as exemplified in experiments HPC-4, HPC-9, HPN-7, and HPC-8 by the very small change in extracted bitumen between 72 and 216 hours at 370 °C. A third way is to consider the transformation of extracted bitumen to expelled oil as a chemical reaction and not as a physical process.

The experiments on sample 26D2' (HPC series) provide a way, in principle, to derive kinetics for total bitumen cracking because most of the original organic matter is bitumen. In fact, the maximum total bitumen yield was obtained from the raw sample. Unfortunately, such an approach was not successful. There are relative few data points, and there are some unresolvable problems. For example, the total bitumen yield for 72-h pyrolysis is identical at 340 and 370 °C, but both are significantly less than the bitumen yields at 320 °C and below. Moreover, the fraction reacted at 320 °C and below depends strongly on the assumed initial bitumen content, which is not known accurately and indeed may vary because of sampling issues. When an initial bitumen content of 7200 ppm is assumed, nonlinear regression produced an activation energy of 28 kcal/mol. For an assumed Gaussian distribution of activation energies, the activation energy increased to 40 kcal/mol with  $\sigma = 2$  kcal/mol. However, probably the strongest statement that can be made from this data is that the global rate constant at 370 °C is about  $1.4 \times 10^{-6} \text{ s}^{-1}$ .

The HPC and HPN series experiments provide an estimate of the rate constant for oil cracking. Again, it is necessary to remember that during much of the reaction, oil is being simultaneously generated and cracked. From the observed small changes in extracted bitumen from 72 to 216 h, it is probably safe to assume that no more oil is being generated. Therefore, the decrease in expelled oil yield between these two times should provide an estimate of the rate constant. For samples 26D2' and QLN, the expelled oil yields decrease by factors of 2.1 and 1.8, respectively. A twofold decrease in 144 h is approximately equal to a time constant of 200 h, which again implies a rate constant at 370 °C of about  $1.4 \times 10^{-6} \text{ s}^{-1}$ .

The close correspondence between the rate constants for total bitumen and expelled oil probably occurs because the region in which the total bitumen decreases most markedly is also the region where most of the total bitumen is expelled oil, especially for sample 26D2'. However, this does not explain the relatively rapid decrease in total bitumen for other samples in the 310-340 °C region. As an alternative approach for bitumen cracking, the conversion of extracted bitumen to expelled oil was considered as a pure chemical reaction. This means that the oil is expelled during hydrous pyrolysis with negligible mass transfer resistance as soon as it is transformed by some undefined chemical reaction from bitumen retained in the rock. To account for the serial reaction aspect of the problem, an induction time was subtracted from the reaction time to account for the time required for the bitumen to be formed. These times were calculated from a preliminary serial reaction model and were 60, 5, and 0.5 hours, respectively, at 310, 340, and 370 °C. The fraction of bitumen cracked was then calculated assuming a maximum bitumen concentration of 26000 ppm, and the resulting data fitted to a Gaussian activation energy model. Kinetic parameters determined were  $A = 5.6 \times 10^{13}$ ,  $E_0 = 52660 \text{ cal/mol}$ , and  $\sigma = 4.2 \%$  of  $E_0$ . These are very similar to the kinetic parameters derived from Pyromat data. In fact, the calculated peak reaction rates for the two parameter sets are within 4 °C of each other for linear heating ranging from a few °C/h to a few °C/min. This is well within experimental accuracy. Moreover, the largest deviation

between observed and fitted bitumen yields is at the highest temperature, where some bitumen appears to be more stable than can be accounted for by a Gaussian distribution model. The discrete distribution derived from the Pyromat data is asymmetric, with more reaction at higher energies than the principal energy at 52 kcal/mol, so it would appear that the Pyromat kinetics can be used quite well for the disappearance of extracted bitumen in hydrous pyrolysis. This confirms the conclusion derived in a earlier section from Pyromat measurements on vacuum residuum from Boscan oil.

The discussion of cracking is now concluded by returning to the cracking of expelled oil. There is insufficient information to derive both A and E. At best, either A or E can be chosen and the other calculated by solving for the value that gives  $k = 1.4 \times 10^{-6} \text{ s}^{-1}$ . If A is again constrained to  $3 \times 10^{13}$ ,  $E = 56880 \text{ cal/mol}$ , which is in the range of that generally used for oil cracking.

**Gas Generation Kinetics.** The second step in the kinetic analysis of hydrous pyrolysis is an assessment of gas generation. The simplest possibility would be that gas generation during the early stages of pyrolysis (before oil cracking becomes important) is described well by rate parameters derived from the TQMS experiments. This possibility was tested by calculating the gas yields for 72-h pyrolysis at various temperatures. These calculations are compared to measured hydrous pyrolysis yields for  $\text{H}_2$ ,  $\text{CH}_4$ ,  $\text{CH}_x$ ,  $\text{H}_2\text{S}$  in Figure 19. In fact, the TQMS rate parameters and product yields do seem to predict the hydrous pyrolysis yields fairly well. The best agreement is with  $\text{CH}_4$  and  $\text{H}_2\text{S}$ . For  $\text{CH}_x$ , the TQMS kinetics are too fast, suggesting that long-chain alkyl groups are cracked more readily in the TQMS experiment. This may be because primary radicals undergo too many decomposition and chain-transfer reactions before being quenched at atmospheric pressure. Probably the most surprising result is that the hydrogen yields from hydrous pyrolysis lead the predictions of the TQMS kinetics. However, there is some question concerning the accuracy of the hydrogen yields reported for hydrous pyrolysis.

$\text{CO}_2$  is the other major gas of interest. Since it was not possible to derive satisfactory  $\text{CO}_2$  kinetics from the TQMS experiment for reasons described in a previous section, a simple rate expression was derived from the hydrous pyrolysis data.  $\text{CO}_2$  is formed early in the pyrolysis process, with most of the primary  $\text{CO}_2$  formed by 280 °C. Again constraining A to  $3 \times 10^{13}$ , a simple distribution of 0.1, 0.4, 0.4, and 0.1 of the reaction occurring with activation energies of 44, 46, 48, and 50 kcal/mol, respectively, reproduced the  $\text{CO}_2$  generation for temperature less than 340 °C. Carbonate decomposition becomes important at higher temperatures, and the  $\text{CO}_2$  yields at 375 and 400 °C are consistent with mineral  $\text{CO}_2$  content. These rate parameters are also compared to  $\text{CO}_2$  generation during hydrous pyrolysis in Figure 19.

## DETAILED PYROLYSIS AND EXPULSION CODES

The ultimate goal of the Annex XII work is to develop both a framework for calculating petroleum generation and migration as well as the parameters specific for the La Luna source rock of the Maracaibo Basin. Between 1987 and 1989, all geologic calculations for the Maracaibo Basin used a simple parallel reaction model for oil generation only. In a parallel effort, the complex computer code PYROL was transported from the Cray mainframe

computer system to Sun workstations and modified to calculate rock compaction and oil expulsion. Kinetic parameters for a generic type II source rock were also derived, and parametric studies were conducted to assess the importance of heating rate, porosity, and source rock permeability on oil expulsion efficiency, expelled gas/oil ratios, and oil API gravity. However, the extensive kinetic parameters needed to run PYROL for the Maracaibo Basin were never derived because 1990 efforts were shifted to a new vehicle, PMOD (Braun and Burnham, 1992). PMOD uses many of the insights gained from PYROL development, but it is written in such a way as to be easily modified for new reaction networks. It also streamlines certain aspects of the calculations so that problems take only tens of seconds to a few minutes on a 386 PC. This section will briefly describe the conceptual advances made with PYROL and the current state of the PMOD code. A detailed description of the PYROL model as revised under Annex XII has been published elsewhere (Braun and Burnham, 1990a). The application of PMOD to the La Luna source rock is given in a following section.

**PYROL.** PYROL was first derived in an attempt to understand the relationship between many types of Green River oil shale pyrolysis experiments (Burnham and Braun, 1985). It coupled an extensive chemical reaction network with a mass transport model that made it possible to calculate both liquid and gas residence times within an open reactor at any pressure. Gas-liquid equilibria were calculated via Raoult's Law by a new approach that used a first-order "vaporization reaction" whose rate depended on the distance away from equilibrium. The initial PYROL model agreed well with laboratory experiments at a variety of heating schedules and pressures.

Over the years, the PYROL mechanism and parameters for Green River oil shale were gradually improved. Relatively few changes had been made by the time it was used in the initial Uinta Basin study (Sweeney *et al.*, 1985; 1987). Shortly thereafter, reactions were added for cracking of C<sub>2</sub>-C<sub>4</sub> gases to methane, reaction of H<sub>2</sub> with residual carbon to form methane, and tracking bitumen. These changes are important to calculate products of interest under geological conditions. A significant effort also went into developing a formalism to make the primary kerogen products themselves a function of H<sub>2</sub> pressure, but that work was never successful enough to be adopted. The overall reaction framework for PYROL as revised under Annex XII is given in Figure 20.

The major changes in PYROL under Annex XII (article 2, paragraph D) were directed towards developing a model of oil expulsion. Raoult's law does not calculate accurate product volumes at geologic temperatures and pressures. The problem was solved by using an equation-of-state model to calculate gas-liquid equilibria and volumes. Initial efforts were described in the 1988 Annual Report (Braun *et al.*, 1988). Both the Peng-Robinson and Redlich-Kwong-Soave (RKS) equations of state were investigated, and it was ultimately decided that the RKS approach with volume translation corrections was the optimum choice when both accuracy and execution time are considered. The conventional flash-equilibrium method was tested in addition to the kinetic-approach-to-equilibrium method, and it was shown that the kinetic approach was more compatible with the solver used for the differential equations describing the chemical reactions.

The final aspect needed to model oil expulsion is a method to calculate rock compaction during burial. It has been known for many years that the porosity of rocks tends to decrease as burial depth increases, but compaction can be hindered by the buildup of excess pore pressure if fluids cannot escape. The model adopted in PYROL for these effects

is given in Figure 21a. If the compaction option is chosen, PYROL solves differential equations for porosity, fluid leakage, and pore pressure simultaneously with those for chemical reactions. Fluid escape is governed by a global permeability, which is related to the hydraulic conductivity divided by the migration distance squared. Porosity is governed by an exponential function relating the equilibrium porosity to the lithostatic pressure minus the excess pore pressure.

The first contribution of PYROL to the Annex XII work was to assess the importance of pressure, sweep gas rate, and heating rate on kinetics derived from programmed pyrolysis (Burnham *et al.*, 1988; Braun *et al.*, 1988). This work was done prior to the inclusion of equation-of-state calculations and compaction into PYROL because those features were not needed for this problem. The underlying issue was one of temperature calibration and how relatively minor variations in experimental technique might cause real differences in observed pyrolysis temperatures. Variations in atmospheric pressure were found to be insignificant ( $< 1\text{ }^{\circ}\text{C}$ ), but a change in sweep gas rate from about 0.4 void volumes per second to none would increase the apparent pyrolysis temperature at  $2\text{ }^{\circ}\text{C}/\text{min}$  by about  $2\text{ }^{\circ}\text{C}$  because of slower product evaporation. More seriously, the calculated evaporation lag becomes more pronounced at lower heating rates, which would cause the apparent activation energy to be too high in the absence of a sweep gas. These calculations provided the basis for explaining the higher activation energy derived from the self-purging reactor, as described in an earlier section, and the hypothesis that even the activation energy from the Pyromat II apparatus may be too high by 1 or 2 kcal/mol, which would result in geologic extrapolations that are 3 to 6  $^{\circ}\text{C}$  too high.

The second contribution of PYROL was to provide a basis for evaluating the validity of kinetic expressions derived from hydrous pyrolysis data. It had been found early in the Annex XII work that the La Luna source rock, as other marine source rocks, requires an activation energy distribution with a mean of about 50 kcal/mol to describe its programmed-pyrolysis profiles. In contrast, Lewan (1985) reported first-order rate constants for Phosphoria shales of 43 kcal/mol. Braun and Burnham (1987) demonstrated that the assumption of a 1st-order rate law when a distribution of reactivity was present, for a data set where temperature and conversion are not decoupled, would lead to an activation energy that was substantially lower than the true value. This would suggest that Lewan's rate parameters are in error and that care must be taken in the design of the INTEVEP experiments to ensure that conversion was decoupled from temperature by using experiments with different pyrolysis times. However, Lewan's activation energies were higher than those estimated from the calculations of Braun and Burnham (1987), and it was also suggested that mass transport limitations had a partially counterbalancing effect.

PYROL simulations of Green River and generic marine source rocks were able to establish the relative effects of activation energy distributions and mass transport limitations on the apparent 1st-order rate constants (Burnham and Braun, 1990). Hydrous pyrolysis is difficult to model with PYROL because it consists of an open system (the rock chips) inside a closed system (the pyrolysis vessel). This was solved by a two step calculation whereby the system as a whole was modeled first as a closed system, then the calculated pressures from the first calculation were used as input pressures for the rock chips, which were modeled as an open system. A principal activation energy of 51 kcal/mol was used for both the Green River shale and generic marine source rock.

We found that the excess volume generated by pyrolysis was insufficient to expel as much oil as observed for Green River (Huizinga *et al.*, 1988) and Woodford (Lewan, 1985) rocks. In contrast, the amount of expelled oil correlated well with the amount of oil vapor in the reactor, suggesting that another mechanism such as diffusion may be important for oil expulsion in conventional laboratory hydrous pyrolysis. Moreover, analysis of the calculated oil vapor yields for 72-h pyrolysis at various temperatures supported the hypothesis that mass transport and activation energy distributions have opposite effects on the apparent 1st-order activation energy. The activation energy for Green River shale, where the reactivity distribution is negligible, was 13 kcal/mol *higher* than the input energy for kerogen pyrolysis, while the apparent activation energy for the generic marine shale was 9 kcal/mol *lower* than the input energy. Although a lack of programmed micropyrolysis and hydrous pyrolysis data for identical samples, along with the simple assumptions in the PYROL model, limit certainty of these results, the calculations provided valuable guidance on how to set up and interpret the INTEVEP hydrous pyrolysis experiments.

The final contribution of PYROL was to provide a test of the RKS-PVT and simple permeation-compaction approaches. Extensive parametric studies were carried out investigating the importance of heating rate and organic content on the amount of overpressuring and its effect on porosity, the timing and efficiency of oil expulsion relative to oil generation, and the gas/oil ratio and API gravity of the expelled petroleum (Braun and Burnham, 1990a; Burnham and Braun, 1990). Conclusions from this work will be summarized only briefly here. Excess pore pressure depends strongly on organic content, and hydrocarbon generation is more important than native pore water for producing overpressures for rich source rocks. Pore pressures reach pressures sufficient to fracture the rock only for simultaneous high TOC and high heating rates. Oil expulsion efficiency depends strongly on TOC, moderately on kerogen type, and weakly on heating rate, and the API gravity of the expelled oil is inversely related to expulsion efficiency. Expelled gas/oil ratios depend strongly on TOC and kerogen type and weakly on heating rate, and residual gas volume in the source rock is roughly independent of all three parameters. These conclusions are qualitatively consistent with prevailing opinion, but no specific confirmation by geological evidence was attempted. However, the unexpelled oil concentrations in the source as calculated by PYROL do agree fairly well with those reported in the literature for sediments, which implies that other related aspects of the calculations are on the right track.

Subsequent to the published studies, additional calculations addressed the effect of the porosity function. The porosity of the La Luna formation is substantially less than that assumed in the initial parametric studies, being only 1-3 percent in the oil window (Talukdar *et al.*, 1987). The effect of porosity on overpressuring and oil expulsion efficiency for a lacustrine source rock is shown in Figure 22. This indicates that low porosity in the range observed in the La Luna Formation substantially increases the likelihood of source rock fracturing as well as improves the oil expulsion efficiency. Bitumen-filled microfractures are observed in the La Luna shale (Talukdar *et al.*, 1987). This indicates that the compaction-overpressuring-fracturing approach in PYROL shows promise for predicting the conditions of migration through fractures.

Although PYROL was, to our knowledge, the first program to fully couple chemical reactions, compaction, and overpressuring, it was too slow to be useful on personal computers. The primary reason for its slowness is the two-phase equilibrium calculation. Fortunately, PYROL calculations showed that the hydrocarbon system existed as one phase

under nearly all conditions of geologic interest. Second, the reaction system used a Gaussian distribution for only some reactions, and memory and integration time needed for that mathematical approach seemed to make it too cumbersome for all reactions. Finally, PYROL was fairly difficult to modify for new circumstances, both for changes in reaction coefficients and conceptual changes. These factors together resulted in the conclusion that PYROL was too unwieldy a code to satisfy the requirements of Article 2, Paragraphs C and D of Annex XII and that a new computer code should be developed that would incorporate many of the conceptual advances of PYROL in a form that would be more easily and generally used.

**PMOD.** One of the primary guiding tenets of PMOD development was that it should be easy to use and modify by a variety of researchers. In a research area such as generation, expulsion, and overpressuring, it is difficult to construct a model that will be satisfactory to a given researcher under various circumstances, let alone different researchers. For example, different situations may call for different degrees of complexity in either the chemical or physical processes to be modeled. PMOD was therefore developed so that the user could tailor the model to any given set of circumstances. PMOD was written as a set of modules that treat chemical reactions, volumetric calculations, and rock compaction and overpressuring, shown in Table 16. A user sets up a problem by choosing the appropriate modules and creating the input files in an interactive manner. It is written in Fortran 77 and has operating versions for PCs, Sun workstations, and VAX computers, thereby satisfying Article 2, paragraph C of Annex XII.

The first module, called KEMMOD, was developed as follows. It is difficult (if not impossible) to develop a specific network that everyone will agree to, and it is mathematically tedious to derive the stoichiometric coefficients for complex networks. During late 1988 and early 1989, a computer program called PYROL Jr. was developed that used elemental balance constraints to calculate stoichiometric coefficients from user-specified reactant compositions and product ratios, but the reaction network was fixed. During the same time frame, interactions between LLNL and a basin-analysis-software company, Platte River Associates, led to the concept of a user-specified reaction network. The concepts of a user-specified reaction network and "automatic" elemental balance calculated from user-specified elemental compositions and product ratios were combined in early 1990 in KEMMOD, an "expert system" computer program.

To construct a chemical model, the user first defines the empirical formula of the desired chemical components chosen from the list shown in Table 17. The user is then asked to define the reactants and products desired in each reaction sequentially. After each set of reactants and products, KEMMOD determines which of a predetermined set of constraints (ratios of products) are needed to calculate the stoichiometric coefficients and asks the user to provide the needed constraints. KEMMOD then calculates stoichiometric coefficients that conserve elemental balance for C, H, O, N and S. The user-definable chemistry model can accommodate various models proposed in the literature as well as several new models for all kerogen types. These reaction models include various combinations of parallel and serial reactions. Further information concerning this process is given in Appendix II.

By the appropriate choice of options in other modules, PMOD can simulate a closed system, a compacting open reactor where all excess fluids are expelled (similar to that in Ungerer *et al.*, 1988), and a compacting leaky reactor where the rate of fluid expulsion is governed by a global permeability coefficient and the difference between the external and

internal fluid pressures (similar to that in PYROL, Braun and Burnham, 1990a). The Ungerer-like expulsion model uses constant product volumes while the PYROL-like expulsion model uses RKS equation-of-state calculations for an assumed single hydrocarbon phase. The Ungerer-like model is a few times faster but provides no information on overpressuring. Both models are described further in Appendix II.

During the course of PMOD development, we made one significant change in the compacting leaky reactor expulsion model, as shown in Figure 21b. The initial model assumed that porosity decreases exponentially with the pressure resulting from weight of rock above, which was assumed to be 2.2 times the pressure of an equal height of water, and that compaction deviated from that exponential according to the excess pore pressure, i.e., the fluid pressure in excess of hydrostatic. In fact, the correct treatment (Hubbert and Rubey, 1959), shows that compaction follows the total stress, which is proportional to the total overburden pressure (water-saturated rock  $\approx$  2.4 hydrostatic) minus hydrostatic pressure, which gives a net compaction pressure of about 1.4 times hydrostatic. This aspect is discussed further in Appendix II. The PMOD model gives a lower sensitivity of pore pressure on TOC.

Of considerable interest is the ability to simulate standard geochemical measurements, such as elemental analysis and Rock-Eval analysis. For this purpose, extractability and volatility parameters were established. For example, a heavy oil component may be nonvolatile and only partially soluble in a particular solvent. Nonvolatile components undergo further cracking reactions while volatile components contribute to the Rock-Eval signal. Nonextractable components are considered as a part of kerogen for TOC calculations.

The output from PMOD occurs in two files: a binary file for plotting and an ASCII file which records values for a few parameters at user-specified intervals. A companion program, PLOTPMOD, is used to create plots from the binary file. The binary file contains up to 36 general variables, including standard Rock Eval parameters, plus concentrations of all chemical species and amounts of all expelled fluids. The user can plot these variables plus ratios of and differences or sums of these variables versus time, temperature, depth, vitrinite reflectance, Rock Eval T<sub>max</sub>, transformation ratio, or any one of the general variables.

## DEVELOPMENT OF A DETAILED PYROLYSIS MODEL

**Comparison of Geologic and Laboratory Maturation.** Article 2, paragraph C of Annex XII specifies that the experimental results will be used to develop a numerical model for pyrolysis of La Luna shale. To increase the likelihood that the detailed pyrolysis model has the ability to predict geologic oil and gas composition as a function of time and temperature, it is necessary to examine how closely the maturity trends observed in the laboratory follow those in nature. A major goal, of course, it to be able to assist the prospect ranking process by predicting (before drilling!) important economic properties such as oil API gravity, sulfur content, metals content, and gas/oil ratio.

The first comparison to establish the link between laboratory hydrous pyrolysis and natural maturation is shown in Figure 23, which gives the decrease in pyrolysis yield and H/C ratio as a function of T<sub>max</sub> for numerous samples of the La Luna source rock from wells throughout the Maracaibo Basin. As for laboratory maturation as shown in Figure 11, most of the hydrocarbon potential has been generated by the time T<sub>max</sub> reaches 450-460 °C. At the

same time, the atomic H/C ratio has decreased to about 0.7-0.65. In fact, the geological and laboratory maturation trends are indistinguishable within experimental error.

The bitumen extracts from the geological samples show maturation trends similar to those generated in hydrous pyrolysis. In Figure 24, as  $T_{max}$  increases from 430 to 460 °C in geologic samples, saturate content increases, aromatic content is variable, and resins plus asphaltenes decrease. Similar laboratory maturity trends are evident in Figures 9-11, but to facilitate the comparison, the experimental hydrous pyrolysate compositions have been replotted versus  $T_{max}$  in Figure 25. The laboratory samples extend to considerably higher maturity. Therefore, it is not certain whether the decrease in saturate content and increase in aromatic content is observed in nature. In Figure 26, three biomarker ratios from geologic samples are plotted versus  $T_{max}$ . The rapid decrease in the pristane/C<sub>17</sub> and phytane/C<sub>18</sub> ratios are very similar to those shown in Figure 12. The noisy increase in pristane/phytane ratio between 430 and 460 °C is confirmed by the geological samples. The decrease near 470 °C could be due either to measurement noise or to molecular-weight-dependent expulsion efficiency.

It is well known that for a given source rock, important economic properties of reservoir oil tend to follow related trends. Oil composition data was provided by INTEVEP for 26 oil wells in Cretaceous reservoirs in the Maracaibo Basin. As a start, Figures 12 and 26 established that the pristane/C<sub>17</sub> and phytane/C<sub>18</sub> ratio decreases as maturity increases and the pristane/phytane ratio increases with maturity. Figure 27 shows that the saturate content increases with pristane/phytane ratio while the sulfur, aromatic, and polar fractions tend to decrease. Opposite trends but with slightly more scatter were observed with the phytane/C<sub>18</sub> ratio. Similar plots with pristane/C<sub>17</sub> showed significantly more scatter.

API gravity is another indicator of maturity. Figure 28 shows the relationship between API gravity and sulfur, saturate, aromatic, and polar (resin plus asphaltene) content in the reservoir oils. The sulfur plot also contains 7 Maracaibo crude oils listed in the Oil and Gas Journal Data Book (PennWell, 1990), and these follow the same trend. As API gravity increases, saturate content increases while sulfur, aromatic, and polar content decreases. Polar content decreases more than aromatic content, so the ratio of aromatic to polar increases from about 1 for low API gravity crudes to more than ten for gas condensates. Metals contents are not available for the INTEVEP oils, but the PennWell oils show a clear decrease in nickel and vanadium content as API gravity increases (Figure 29).

An important question for constructing a chemical mechanism is whether these maturity trends are due to dilution or transformation. For example, generation of large quantities of saturated and small amounts of aromatic hydrocarbons from kerogen could dilute the sulfur, polar, and metal content of the initial oil. On the other hand, the heteroatomic molecules could undergo chemical reactions that remove non-hydrocarbon functional groups. In addition, sulfur has a higher specific density than carbon, so how much of the change in API gravity is due to a change in chemical type and how much is due to changes in molecular weight (boiling point distribution)?

The first question can be answered partially by plotting the absolute yields of saturates, aromatics, and polars versus temperature as in Figure 30. All three classes are generated up to about 310 °C for 72-h hydrous pyrolysis, but the saturate fraction has increased proportionately the most. By that point,  $T_{max}$  has increased slightly from 430 to 439 °C. Above that temperature, the aromatic and polar fractions are depleted, but the aliphatic yield remains roughly constant up to about 360 °C, presumably because the rate of

saturate cracking is balanced by additional generation from the aromatic and polar fractions. By that time,  $T_{\max}$  has increased to 450-455 °C. Above that temperature, all fractions are consumed, but the polar fraction decreases the most. The aromatic fraction appears to have a refractory portion that is highly resistant to cracking, so it becomes the dominant fraction at the highest temperatures.

The decrease in sulfur content with maturity appears to be predominantly via removal rather than dilution. Figure 31 shows the sulfur content for various boiling point fractions. With the exception of the lightest fraction in Tia Juana heavy and all fractions of Boscan, the sulfur contents tend to be similar for a given boiling point range. One would expect that the maturation process includes the disproportionation of heavy fractions into light fractions and residue. Because the sulfur content of the heavy fraction appears to be relatively independent of maturity, it would then follow that the disproportionation process converts the sulfur to either residue or gas. Unfortunately, this thesis could be tested only partially with the hydrous pyrolysis experiments. Tables 11 and 15 indicate that  $H_2S$  yields increase during oil cracking conditions. At the same time, the sulfur content of the non-volatile fraction of both expelled oil and extracted bitumen are roughly constant (Table 14). However, no boiling-point information is available so material balance calculations are not possible. Furthermore, there may be some distinct difference in sulfur reactions between the hydrous pyrolysis and nature because the sulfur content of the non-volatile fraction is higher than most Maracaibo crudes and is close to that in Boscan.

**A Detailed PMOD Model for La Luna Source Rock.** The goal of a detailed pyrolysis model for the La Luna source rock is to provide a basis for predicting economically important petroleum properties, such as gas/oil ratio, API gravity, sulfur content. The petroleum maturation process is far too complex to model in terms of fundamental chemical reactions, so even a detailed pyrolysis model will use lumped chemical species and reactions. The object, therefore, is to reach the appropriate compromise between complexity and simplicity so that important properties can be predicted with a tractable model.

One of the complications of developing a predictive chemical reaction mechanism is that the product properties are determined by a combination of what are normally called primary and secondary reactions. For example, generation of oil is a primary reaction and cracking of oil to gas is a secondary reaction. A given product could be formed by both primary and secondary reactions, i.e.,  $H_2S$  can be generated both directly from kerogen and from cracking of oil. Unfortunately, the distinction between primary and secondary reactions is often fuzzy. For example, methane generation from the insoluble organic matter continues after oil potential has been extended. Should this higher temperature generation be considered as primary generation from kerogen or as secondary generation from the residue of kerogen decomposition?

The reason for attempting to develop a good separation between primary and secondary reactions is that the extent of secondary reactions usually depends on the rate of transport out of the oil generation "kitchen". In fact, for the excess volume expulsion models in PYROL and PMOD, the rate of expulsion from the source rock and the extent of secondary reactions are intimately related. Any given laboratory experiment used to calibrate a chemical kinetic model will probably have a different transport mechanism, and a good kinetic model should be able to account for differences in composition based on the secondary residence time in the reactor.

The first issue to be faced is what lumped chemical species should be included in the chemical mechanism. PMOD has the capability of including up to 9 gases and 12 oil fractions. Are they all necessary? Little information was available for nitrogen content of the products, and the nitrogen gas reported for the hydrous pyrolysis experiments could be carbon monoxide instead. Also, nitrogen gases are not a significant exploration concern in the Maracaibo Basin, so nitrogen was excluded from the mechanism. Similarly, carbon monoxide was not well characterized in the laboratory experiments and is not a significant geochemical gas, so it was excluded. This leaves CH<sub>4</sub>, CH<sub>x</sub>, H<sub>2</sub>, CO<sub>2</sub>, H<sub>2</sub>S, and H<sub>2</sub>O in addition to the oil and kerogen species. For material balance, all oil and kerogen species were assigned a C, H, O, and S content.

The twelve oil species in PMOD nominally represent 4 boiling point ranges and three chemical types. The most obvious definitional approach of chemical type would be according to the SARA classification: saturates, aromatics, and resins plus asphaltenes. However, it is not possible to develop such scheme. The reaction mechanism needs to have a stoichiometry for the decomposition of each oil type, which depends on its chemical composition. However, the composition of each aromatic and polar fraction is undoubtedly itself a function of maturity. For immature oils the aromatic and polar fractions include aromatic and polar groups attached to long alkyl chains. As the oil matures, these alkyl groups are cracked off, leading to additional saturates plus methylated aromatic rings, both hydrocarbon and heteroatomic. PMOD is unable to deal with a chemical fraction having non-constant properties. Instead, three chemical types were defined: (1) saturates, (2) dealkylated aromatics plus polars, and (3) alkylated aromatics plus polars. The oil cracking reactions followed these predominant trends: type (3) fractions crack to type (1) and (2) and smaller type (3) fractions; type (2) tends to coke; and type (1) forms smaller type (1) fractions and ultimately gas.

The chemical reaction network is shown in simplified form in Table 18, and a PMOD input file, including all stoichiometric and rate constants, is given in Appendix III. The overall reaction scheme uses 5 kerogens, 9 oil species as oil fractions, 3 oil species as biomarker concentrations, five gas species, and water. The initial kerogen is split into two parts: kerogen 1 yields early water, CO<sub>2</sub>, H<sub>2</sub>S, and small amounts of CH<sub>4</sub> and CH<sub>x</sub>. Kerogen 2 yields heavy bitumen (HO3), early oil and gas, and kerogen 4. The heavy bitumen and kerogen 4 then break down with identical rate constants (as suggested by the Boscan residuum and asphaltene experiments) to oil, gas, and a carbonaceous residue. Each chemical species has an empirical chemical formula designed to mimic maturation trends. Rate constants of the various reactions were chosen in a trial-and-error fashion in an attempt to mimic the important trends demonstrated by the Pyromat, pyrolysis-TQMS, and hydrous pyrolysis experiments. Constraints on frequency factors and activation energies were based on past experience.

As a first test of the mechanism, consider the effective kinetics for total hydrocarbon generation as in a Rock-Eval or Pyromat instrument. The calculated T<sub>max</sub> at 25 °C/min is 467.5 °C, which is at the upper end of the range measured for La Luna samples QL7 (463 °C) and QLN (468 °C). The calculated Rock-Eval (true T<sub>max</sub> minus 35 °C) is within the range of measured values. Analysis of simulated Rock-Eval evolution profiles at heating rates of 2.5 and 25 °C/min gives kinetic parameters very similar to those in Table 4 for samples QL7 and QLN. The approximate and rigorous Gaussian distribution parameters were 3.0 and 3.1%, respectively. The discrete model parameters were  $A = 2.7 \times 10^{13}$  and an energy distribution

(E in kcal/mol-%) of 49–14.8, 51–39.3, 52–19.8, 53–11.4, 54–4.2, and other minor fractions up to 62 kcal/mol.

A second comparison is with the gas evolution profiles from the pyrolysis-TQMS experiments. The calculated profiles given in Figure 32 can be compared to the measured profiles given in Figure 5. The total amounts of CH<sub>4</sub>, CH<sub>x</sub>, and H<sub>2</sub>S are within 10% of the measured values, and H<sub>2</sub> is similar for that generated below 600 °C. Except for CO<sub>2</sub>, the calculated and measured T<sub>max</sub> values are within 10 °C of each other, which is quite satisfactory considering that the gas generation rate kinetics are known less precisely than the total hydrocarbon kinetics. In addition, the incorporation of gas generation into a more complete reaction network rather than using individually optimized activation energy distributions provides additional constraints. The discrepancy for CO<sub>2</sub> is due to an incompatibility between the TQMS and hydrous pyrolysis measurements. The hydrous pyrolysis experiments (Figure 19) indicate that most of the "organic" CO<sub>2</sub> is generated very early in the reaction. In contrast, the TQMS results indicate a broad background evolution, which may be due to inorganic carbonate decomposition with a small "organic" peak at about 450 °C. The CO<sub>2</sub> kinetics in the detailed mechanism have been chosen to be compatible with the hydrous pyrolysis results. Carbonate decomposition has been ignored. An additional discrepancy is that the measured H<sub>2</sub>O profile has additional peaks, which may be due to either organic or inorganic sources.

A third comparison is with the INTEVEP hydrous pyrolysis experiments. The calculations are for a closed system in which no distinction was made for expelled and unexpelled oil. The total bitumen yield and fraction of remaining insoluble organic carbon is shown in Figure 33. Only the measurements for sample QL7 are shown, but the peak bitumen generation occurs at the same temperature for other samples as indicated in Figure 18. The measured bitumen yield agrees better with the calculated bitumen yield not including the naphtha fraction. Experimentally, most of the naphtha fraction may have evaporated during handling. The calculation indicates a minimum in the amount of insoluble organic carbon. It is difficult to say whether a minimum is observed experimentally. The data scatter and lack of a good organic carbon balance preclude any firm conclusion.

A comparison of the measured and calculated gas generation is given in Figure 34. The measured H<sub>2</sub>S yields are slightly lower than calculated in the mid-temperature range, but this could be caused by sulfur-gas capture on the reactor or sample bottle. Also, the model calculation tends to underestimate the increase in H<sub>2</sub>S at temperature greater than 320 °C, suggesting that the model underestimates H<sub>2</sub>S generation from oil cracking or residual kerogen. The discrepancy in CO<sub>2</sub> generation at 340 °C and higher temperatures is due to carbonate decomposition, which is not included in the model. The largest discrepancy is for H<sub>2</sub>, for which the model predicts less than observed. However, it is likely that the high measured H<sub>2</sub> yields are erroneous because of interferences. It is noteworthy that an experiment from the most recent series (HPN) produced a lower amount of H<sub>2</sub>, which is consistent with model calculation. The decrease in calculated hydrogen at 400 °C is due to a hydrogen consumption reaction that is designed to largely eliminate H<sub>2</sub> at geological conditions. Some of the counter-balancing high temperature H<sub>2</sub> generation reactions have been neglected. The calculated hydrocarbon gas yields agree reasonably well with measured values, but there tends to be too little calculated at low temperature and too much in the mid-temperature range. Although the hydrocarbon gas generation per unit TOC is fairly independent of sample, the differences in bitumen potential cause the hydrocarbon gas/oil

ratio to vary with sample. By intent, the model calculation agrees best with the QL7 gas/oil ratio. The calculated gas wetness ratio peaks during peak oil generation and is intended to be consistent with geologic observations, but the measured hydrous pyrolysis values have too much scatter to either confirm or deny the model.

Calculated oil composition varies during the course of pyrolysis, as shown in Figure 35. The common feature between the model and the SARA separation procedure is the saturate content of the oil. Saturate content was calculated for the LO+ oil (no naphtha), since all light ends are lost during the separation procedure. The model agrees well with experiment except in the 370-375 °C region. Here the model calculates a higher peak saturate content at 370 °C while the experiment indicates that saturate content has declined substantially by 375 °C. Another oil composition feature calculated by the model is biomarker content. The calculated biomarker ratios of pristane/phytane and phytane/C<sub>18</sub> agree well with measured values.

Another consideration is the sulfur content of the oil. The maximum possible sulfur content of bitumen in PMOD is 4.3%, which is slightly lower than the 7.6% measured for sample HPN-5 (Table 14). On the other hand, the sulfur content in crude oil residuum samples shown in Figure 31 is more typically about 3%, with Boscan being about twice as high. Other data in Table 14 indicate that the sulfur content of heavy oil, that is, the material remaining after evaporation at room temperature for many days, is always about 6-7%. In contrast, the sulfur content calculated by PMOD for the MO+ fraction, which may represent the non-volatile samples received from INTEVEP, decreases from 4% to 2% as pyrolysis temperature increases. Perhaps this indicates that the sulfur content of the MO2 fraction (dealkylated aromatics) is too low, but there is insufficient evidence to warrant a change in the mechanism at this point.

All comparisons between measured and calculated hydrous pyrolysis presented to this point have been for 72 hour pyrolysis, but some additional experiments were conducted for other times. The Rock-Eval T<sub>max</sub> of the pyrolysis residue provides a common reference. The increase in T<sub>max</sub> upon 72-hr pyrolysis as well as a crossplot of T<sub>max</sub> with other diagnostic variable is given in Figure 36. The model follows observed trends well.

**Parametric Studies Using PMOD.** Before proceeding to test the validity of the kinetic models in the Maracaibo basin, it is useful to demonstrate the capabilities of PMOD under generic geologic conditions to get some idea of the importance of different variables. The La Luna chemistry mechanism described earlier was used in a series of generic parameter sensitivity studies using typical geological conditions. This discussion will be limited to the parameter ranges shown in Table 19, which encompass the nominal extremes to be expected. The first two columns give the parameter name and its definition. A base case run was made with the middle value of each parameter. Additional runs were made, changing one parameter at a time to its lower or higher value, while keeping all others at their base values. A lithostatic/hydrostatic pressure ratio of 2.4 was used for all runs. The parabolic relative permeability curves shown in Appendix II were used in the expulsion calculations.

Figure 37 shows some of the results for the base case. In these plots we use temperature as the x-axis variable, although PMOD is capable of using time, depth, Rock Eval T<sub>max</sub>, vitrinite reflectance, or many others. In this study we use a constant geothermal gradient of 25 °C/km, so the depth range spanned in the plots is 0 to 7 km. To simulate a bitumen-like material and a heavy, dealkylated aromatic/polar material, two species (HO3

and MO<sub>2</sub>, respectively) are assigned a volatility of zero and, thus, do not contribute to the hydrogen index. The two species are still permitted to be expelled, although at a reduced rate, by assigning expellability factors of 0.2 and 0.1, respectively. Thus, one can note in the upper left graph that the hydrogen index is significantly less than the amount of generated oil and even somewhat less than the expelled oil. The amount of oil that has cracked is not shown, but is equal to the generated oil minus the unexpelled oil and the expelled oil. At 200 °C the final oil yield is seen to be 72.5% of the generated oil.

Most of the other graphs of Figure 37 are self explanatory and illustrate a few of the capabilities of PMOD. Note in the porosity plot that the partial porosity not filled with heavy and medium oil is much less than the total porosity during kerogen pyrolysis. This partial porosity is probably the quantity that should be compared with the measured porosity of unextracted field samples. If such measured porosity were mistakenly used to tune the model parameters to attempt to match the calculated total porosity instead of the partial porosity, greatly different calculated pore pressures and other results would be obtained. This emphasizes the importance of making sure that comparisons between model calculations and field data are well thought out.

Figures 38 through 43 show the most significant results of the parameter sensitivity study. The same quantity or quantities are plotted in all graphs of a given figure. The parameter that is being varied is shown in the upper left corner of each graph. Results for the base value of the parameter are shown by the solid lines, while results for the lower value are shown by the small-dashed line and for the higher value by the larger-dashed line, using parameter values from Table 19. In Figure 38 note that the organic carbon content (TOC), the compaction coefficient (EPSC), and the hydraulic conductivity coefficient (KPRES) have significant effects on the quantity of expelled oil, since these parameters all have an important effect on the residence time of the oil in the source rock and, therefore, on the extent of oil cracking. In Figure 39 the pore pressure is largely determined by EPSC and KPRES. One might think that TOC should have a larger effect on pore pressure. This is not the case, because a higher TOC is also associated with a higher porosity, as shown in Figure 40, which tends to alleviate the pore pressure somewhat. Figures 41, 42, and 43 show that the API gravity of the expelled oil, its saturate mass fraction, and the expelled gas/oil mass ratio depend mainly on the fluid residence time in the source rock and, thus, mainly on TOC, EPSC, and KPRES.

Figure 44 shows six more diagnostic quantities. These were found to be less sensitive to the parameters that were studied and, consequently, only the effects of TOC are shown. Effects of EPSC and KPRES were similar to these, while effects of the other parameters were less. The effects of heating rate, for example, are simply an offset in temperature (or equivalently in time or depth), without any appreciable change in the magnitudes.

An important result of the parameter study is that many properties of the expelled oil depend on the fluid residence time in the source rock. The residence time is, to a first approximation, directly proportional to the TOC and inversely proportional to the porosity. In Figure 45 we plot six quantities as a function of TOC/POR, where POR is the total porosity at the midpoint of oil generation. A very good correlation is seen in all cases. The similarity of the correlations suggests that these quantities are well correlated between each other. This is confirmed in Figure 46 for several important properties of the expelled oil. The calculated trend can be compared to the natural trends shown in Figure 28. The API gravity-saturate

trends agree very well. The calculated API gravity-sulfur content trend is in the right direction but too weak.

Finally, Figure 47 examines differences in various properties depending upon whether or not the material was first subjected to solvent extraction for the PMOD base case calculation. The solid lines are without extraction and the dashed lines are with extraction. At first glance, it might seem anomalous that the hydrogen index is nearly independent of the extraction and, in fact, is even slightly higher for the extracted material. This is a consequence of both S<sub>2</sub> and the remaining TOC decreasing with extraction, with TOC decreasing slightly more than S<sub>2</sub>. T<sub>max</sub> and transformation ratio are likewise nearly independent of extraction, while S<sub>2</sub> for methane is lower for the extracted material until all of the bitumen is either expelled or cracked.

## INITIAL KINETIC MODELING OF THE MARACAIBO BASIN

Application to a basin where hydrocarbons are being recovered (as specified in Article 2, paragraph F of Annex XII) is the ultimate test of the kinetic approach to modeling hydrocarbon generation, expulsion, and migration. The level to which predicted characteristics of generation, expulsion, and migration can be compared to the real situation depends on (1) the level of detail in the geochemical model, (2) the quality and quantity of the geochemical data obtained from the basin, (3) the quality and quantity of geological data that can be used to develop paleothermal histories of the basin rock formations, and (4) the complexity of the basin: how well it conforms to the idealized cases that are within our ability to model. The acquisition of geologic and geochemical data in hydrocarbon producing basins is expensive and generally is done in order to satisfy exploration and production needs rather than research needs. In this sense, producing basins are at best imperfect laboratories for testing geochemical concepts, but they are the only ones available.

Paleothermal history models of sedimentary basins can range from simple models that can be computed with a hand calculator to complex models requiring large mainframe computers. The simplest models involve determining (1) the present-day thickness of the basic stratigraphic units, (2) the ages of the rocks at the stratigraphic contacts, (3) estimates of the timing and duration of periods of hiatus or uplift, (4) the amount of uplift, and (5) an estimate of the geothermal gradient—usually made from measured bottom hole temperatures. The most complicated models incorporate all of the above, but also include knowledge of the physical properties of the rocks relative to compaction, heat flow, heat production, and fluid transfer. The applicability of these complex models is greatly limited by the amount of physical property, thermal, and hydrologic data available in a given application. Incorporation of rigorous mathematical expressions for coupled compaction, heat flow, and fluid flow in the modeling of even the most rudimentary basins is still a frontier research area.

**Geologic Modeling Codes.** In the early stages of the Annex XII work, Lotus 123 spreadsheets were developed to calculate the extent of reaction from a distribution of activation energies and to calculate vitrinite reflectance at a given depth (which has a unique time-temperature history). The spreadsheets were not an efficient way of carrying out multiple calculations with different time-temperature histories needed when calculating profiles of vitrinite reflectance with depth or calculating the extent of oil generation for a

number of wells. In addition, a capability to calculate basin thermal histories with a simple one-dimensional heat conduction model that also accounted for the effects of compaction was needed. These requirements were achieved with the development of the codes VITMAT, BASINVIT, and BASINMAT2 documented elsewhere (Sweeney, 1989; Sweeney, 1990). VITMAT was used to determine thermal histories via a 1-D heat conduction model incorporating sediment compaction which was then used in the program to calculate vitrinite reflectance. BASINVIT and BASINMAT2 used a time-temperature history as an input file and calculated the extent of conversion of the kerogen at one million year time steps, vitrinite reflectance at each major formational time boundary, and the final value of  $T_{max}$  of the kerogen. Both of these codes could be run in a batch mode to quickly and easily calculate kerogen conversion for a number of wells and for a number of depths in an individual well. By the middle of 1989, Platte River Associates had incorporated the LLNL EASY%Ro vitrinite reflectance model into their 1-D basin thermal history code BasinMod, which LLNL had acquired through a technology transfer agreement with them. VITMAT and BASINMAT2 proved to be useful in cross-checking the calculations of BasinMod. More recently, BasinMod has been improved further with the addition of the capability to handle combined serial and parallel reaction schemes and the calculation of the kinetic  $T_{max}$ . These improvements were made with technical advice from LLNL under the technology transfer agreement. As a result, BasinMod was used almost exclusively in the latter stages of the Annex XII work.

**Initial Paleothermal Histories.** Thermal histories for about 80 wells in the Maracaibo Basin had been developed by INTEVEP and used to estimate oil generation characteristics and timing with an empirical kinetic method (Talukdar *et al.*, 1986). The thermal histories used in the study were developed at INTEVEP from bottom hole temperature data (used to estimate average geothermal gradients), knowledge of the stratigraphy both regionally and from picks in individual wells, and from estimates of amounts of Miocene and Eocene erosion, which varied considerably over the basin area. Because little was known about the thermal properties of the rocks in the basin, heat flow and detailed temperature profile data were not available, and there were large uncertainties in the estimates of the amount of erosion, it was felt that more detailed thermal history modeling was not warranted.

These initial paleothermal histories for 80 wells were supplied by INTEVEP and used, with the code BASINMAT2, to calculate the extent of conversion of the kerogen in the La Luna Formation throughout the Maracaibo Basin and make estimates of the timing of the onset of expulsion and secondary gas generation. INTEVEP also had vitrinite reflectance data for 22 of the wells for which thermal histories had been determined. The amount of vitrinite data for an individual well ranged from a single measurement at depth to profiles with up to 15 or 20 determinations over depths of several thousand feet. These data were used, with the vitrinite reflectance model, to cross check the consistency of the thermal histories with the vitrinite data and make appropriate, generally minor, changes in the thermal histories.

In order to minimize complications caused by long distance migration, it was decided that comparison of predicted and measured characteristics of the hydrocarbons should be confined solely to kerogen of the Cretaceous La Luna Formation marine shale source rock and oils recovered in nearby (stratigraphically above and below the La Luna) Cretaceous

reservoirs. Thermal histories had been determined from only about one-third of the wells for which INTEVEP had geochemical data from Cretaceous source rocks and reservoirs. Thus additional thermal histories had to be developed by LLNL using the 1-D thermal conduction codes VITMAT and BasinMod, stratigraphic data for the additional wells supplied by INTEVEP, and by extrapolating relevant data from other parts of the basin.

In order to use the 1-D thermal conduction model to develop a thermal history, values must be known for (1) the local heat flow from the basement, (2) porosity-depth characteristics of the rocks in each formation, (3) rock matrix thermal conductivities, and (4) amounts of erosion during uplift occurring during the Eocene and Miocene. None of these data were available to us for these additional wells and nothing was known about true temperature-depth profiles for any wells other than estimates from the thermal gradients used in the thermal histories supplied by INTEVEP; thus the problem was very poorly constrained. However, the general lithologies of the different formations were known and good profiles of vitrinite reflectance versus depth were available for about 5 wells. The first step was to develop thermal models for these 5 wells that closely matched the vitrinite data. Estimates of the physical properties of the rocks were made from general descriptions of the formation lithologies and using the default parameters in BasinMod. For all 5 wells a self-consistent set of parameters were obtained, with an assumed regional heat flow value of about 45 mW/m<sup>2</sup>, that both matched the vitrinite data and resulted in thermal histories not much different from those originally developed by INTEVEP using the simpler gradient method. The parameters developed for these 5 wells were then used, with the given lithologic data and estimates of erosion amounts from regional trends, to calculate thermal histories for the additional wells needed to make a more complete comparison with the geochemical data.

**Initial Maturity Calculations and Comparisons.** All of the above thermal history determinations were used to make initial calculations of kerogen conversion in the basin. These calculations, reported in Sweeney *et al.* (1990), compared the predictions from four different sets of kinetic parameters determined from sample QL7. The calculations showed that, because of differences in the thermal histories in different areas, the basin could be divided into four regions with different maturity characteristics, shown in Figure 48. From the calculations of kerogen conversion, estimates were made of the timing of the beginning of oil expulsion and secondary gas generation and contour plots were produced showing the variation of these throughout the basin. Calculations of the H/C ratio and T<sub>max</sub> of the residual kerogen agreed very well with measured values. Measured values of API gravity showed the expected gradual increase with the calculated increase in the extent of kerogen conversion. In some areas of the basin notable differences in the maturation-time profiles were seen for the different kerogen kinetic parameters used, but no significant differences were noted in the predictions of present-day values of T<sub>max</sub> and H/C.

The primary conclusion of this preliminary modeling is that uncertainties in the laboratory-derived global chemical kinetic parameters are insignificant compared to the uncertainties in the thermal histories and that the overall kinetic approach showed excellent agreement between predicted and measured characteristics for this level of geochemical comparison. In addition, it appears possible that the overall properties of the oil may be correlated with an overall maturity indicator. On the other hand, it is not certain that such a global approach could lead to reliable correlations for pore pressures and expulsion

efficiencies, nor could it predict possible second-order relationships among rock properties, expulsion timing, and oil and gas composition.

## TESTING PMOD WITH DATA FROM THE MARACAIBO BASIN

The ultimate test of the generation, pore pressure, and expulsion models envisioned in Article 2, paragraph F of Annex XII involves a detailed comparison of model predictions with geologic data. INTEVEP provided LLNL with geochemical data from oils recovered from Cretaceous reservoirs and extracts of residual organic matter from the La Luna source rock. Data from oils in Cretaceous reservoirs is especially useful for checking PMOD calculations because the oils will not have migrated very far from their Cretaceous La Luna source rock and they will have suffered minimal post-expulsion modification. In addition, INTEVEP provided a profile of fluid pressure versus depth for the VLE686 well. This well is overpressured at the present day and this data set has been used to help calibrate parameters in PMOD that affect expulsion and pressure development.

Compositional changes of the organic constituents with increasing temperature and pressure due to burial are highly dependent on whether oil and gas are expelled from the system. The timing and amount of expulsion are also important. Because of this, the procedure for testing the model is to first use the pressure-depth data from VLE686 to constrain parameters affecting expulsion and then, because there is no way to constrain the parameters for other well locations, use the same values to model the chemical changes in the organic matter for the rest of the wells for which data is available for oils and extracts. Calculated chemical properties that can be compared to the data are (1) the expulsion efficiency (calculated from Rock Eval S1 and S2 and inferred from trends of the amount of extractable organic matter (bitumen) remaining in the rock as a function of maturation); (2) API gravity of the reservoir oils; (3) Rock Eval  $T_{max}$ , hydrogen index, and H/C ratio of the organic matter remaining in the source rock; (4) the saturate content of the oils and extracts; and (5) the pristane/phytane and pristane/ $C_{18}$  biomarker ratios of the oils and extracts.

In order to test the hypothesis that the oils in Cretaceous reservoirs have not moved very far from the source rock (and thus suffered the same temperature history as the source rock), calculations were carried out for two extreme cases; (1) the closed system, in which there is no expulsion, and (2) the leaky system, in which expulsion depends on properties that govern the flow of fluids out of the rock such as permeability, porosity, and fluid viscosity. Chemically, oils in the closed system calculation will be the same as those in a reservoir that is in or very close to the source rock. The chemistry of leaky system oils will depend on the timing of expulsion and whether the expelled oils continued to be heated after being released from the source rock.

**Pore Pressure Modeling in the Maracaibo Basin.** The leaky system option calculates the pore pressure, but several important parameters that affect expulsion characteristics that must be known or estimated. These are the TOC of the source rock, EPSZ—the initial porosity, EPSC—the rock compaction coefficient, FLITH—the ratio of pore pressure to lithostatic pressure at which the rock is assumed to fracture, RLITH—the ratio of lithostatic pressure to hydrostatic pressure (dependent on rock density), the relative permeability coefficients, and KPRES—the hydraulic conductivity coefficient. The average

present-day TOC of the La Luna shale is about 3.8% (Talukdar *et al.*, 1987); INTEVEP provided measurements of the present-day TOC of the La Luna for ten wells in the Maracaibo Basin. Typical values of FLITH observed in hydrofractured rocks have been estimated to be between 0.8 and 0.9 (Palciauskus and Domenico, 1980; Lerche, 1990). The lithostatic gradient estimated by INTEVEP for well VLE686 corresponds to a value for RLITH of 2.3. Values for the other expulsion-related parameters listed above can only be estimated. The results of the calculations for the leaky system case can be tested, however, by comparing the prediction of pore pressure with that measured in well VLE686 (see Figure 49a).

In modeling pore pressure development in VLE686, the approach taken was to use reasonable values for the compaction and relative permeability coefficients, a TOC of 9.0% (which resulted in a present-day TOC of about 3.5% for the various cases) and a value of 0.85 for FLITH. KPRES was then varied to reproduce the measured value of pore pressure at the present-day depth of the La Luna shale. In Figure 49a the measured pore pressure at the location of the La Luna formation (approximately 4700 m - 15,500 ft depth) is about 86 MPa (0.82 times lithostatic). Porosity is constrained by present-day measured values to be less than about 2% at depths of 4-5 km (Talukdar *et al.* 1987). However, the measured present-day porosity is a function of the burial history of the formation because overpressuring and kerogen conversion can retard porosity development or even create new porosity. In addition, values of present-day measured porosity may be affected by the presence of bitumen or heavy oil that looks like rock matrix to the porosity measurement system. In PMOD, bitumen and heavy oil are treated as filling the porosity; if bitumen and heavy oil are present, measured porosities may underestimate the true (non-rock matrix) porosity. Values of pore pressure calculated by PMOD are very sensitive to the values of EPSC and KPRES used. If EPSC is decreased to make the porosity lower, the pore pressure may increase more readily, causing the final porosity to be larger than intended. In modeling the pore pressure profile of well VLE686, it was found that the values of EPSC and KPRES were tightly constrained by the need to obtain a final porosity that was low and still get the proper values of pore pressure at depth. A value of 0.6 for the initial fractional porosity of the La Luna shale was used, with values for the relative permeability coefficients the same as those (see above) in the base-case PMOD model.

Different values of KPRES and EPSC were tried until the pore pressure of the model calculation matched the measured value of present day pore pressure at the depth of the La Luna Formation (4700 m) in VLE686 within 1% and the final porosity was less than 0.02. For EPSC equal to  $2 \times 10^{-7} \text{ Pa}^{-1}$  a value of KPRES of  $1 \times 10^{-20}$  was needed to obtain a present-day pore pressure of 87.7 MPa with a present-day porosity of 0.015.

Plots of the calculated and measured pressure-depth profiles for VLE686 for the above parameters are shown in Figure 49b. The system is assumed to be in pressure equilibrium and all of the excess pore pressure (pore pressure minus hydrostatic pressure) is developed in the La Luna formation at 4700 m depth and pore pressure decreases linearly above (into the Colon Formation - a thick shale seal) and below into the fractured limestone Cogollo Formation (which has higher permeability). The match between calculated and measured pore pressures can be improved (Figure 49c) by allowing some pore pressure build-up in the Colon Formation due to compaction disequilibrium. This was done by running a calculation for the thermal history at 4328 m with no organic matter (0.0 mass fraction TOC in the model), a value of EPSC of  $8 \times 10^{-8} \text{ Pa}^{-1}$  and a value of KPRES of  $1 \times 10^{-20}$ , which results in an additional 10.2 MPa of excess pressure needed to match the measured values at that

depth. (The true pressure-depth profile will be more complicated than that modeled here, so this value should be considered to be minimal estimate of the amount of excess pressure needed in the Colon shale). Calculations carried out with different values of TOC in the La Luna at 4700 m depth indicate that the present-day pore pressure in this well is only slightly affected by organic richness, but it could be important if, at the time of maximum oil generation, the pore pressure reaches the fracture limit and creates microfracture pathways for primary migration. What these calculations mean is that a large portion of the excess pressure in well VLE686 can be explained by pressure development in the La Luna formation with a significant contribution due to compaction disequilibrium in the overlying Colon shale. Calculated pressures are consistent with the observation that porosities and permeabilities are somewhat higher in the overlying Colon Formation than in the La Luna Formation and with the Colon Formation being barren in organic matter.

The development of pore pressure with time in the La Luna Formation (4700 m depth) in well VLE686 is shown in Figure 50 for both 9.0% and 0.0% initial TOC. During the initial peak in oil generation and pressure development at 62 m.y. time (38 Ma), about 25% of the excess pressure is caused by organic maturation, the rest by compaction disequilibrium. The second peak in oil generation occurs at about 90 m.y. time (10 Ma) and 34% of the excess pressure is caused by organic maturation. At the present day, 100 m.y. time, organic maturation has slowed because reactant is beginning to run out due to the advanced stage of maturation and only 8% of the excess pressure is due to organic maturation.

The same parameters used to model pore pressure generation in VLE686 were also used, with the corresponding respective thermal histories, to run PMOD for an additional 21 wells in the Maracaibo Basin. The additional 21 wells were those for which oil composition, Rock-Eval, or extract composition data were available. Results of the pore pressure calculations for wells representative of the four different oil maturity characteristics (Figure 48) are shown in Figure 51. The plots of pore pressure for the different areas indicate that excess pore pressure can be expected to exist in the La Luna Formation at the present day in all four areas, but the level of overpressuring can be very different in each case depending on the level of maturation and the maturation history.

Calculated present day porosity of the La Luna Formation is shown in Figure 52. Both the total porosity (which includes void space filled with bitumen, which we define as heavy and medium oil for this purpose) and partial porosity (total porosity less that fraction filled with bitumen) are shown in the figure. The partial porosity is that which would be actually measured on an unextracted sample of source rock. The calculated total porosities range from about 0.01 to 0.085 and the partial porosity ranges from about 0.005 to 0.02. The scatter in the calculated values is due to the different thermal histories for each well and resulting different effects of pressure development or new porosity development (from the conversion of kerogen when pore pressure is sufficient to hold open the porosity) during hydrocarbon generation and expulsion. Talukdar *et al.* (1989) reported present day porosities (partial porosities of unextracted samples) of about 0.01 to 0.02.

Expulsion efficiency calculated by PMOD is shown in Figure 53. The calculations match the trend of the measured values quite well over the range of measured  $T_{max}$ . Another test of the expulsion calculation in PMOD can be done by comparing the calculated amount of bitumen in the rock with measured values. Values of measured bitumen versus measured kerogen atomic H/C ratio were reported by Talukdar *et al.*, (1987, Fig. 7) and versus TTI by Talukdar *et al.* (1986, Fig. 5). Using the results of the PMOD runs for all of the wells

modeled, the bitumen remaining in the rock was calculated by summing the total of the medium oil fraction plus HO3. Calculated bitumen versus both calculated H/C atomic ratio and TTI, calculated from the well thermal histories, are shown in Figures 54 and 55. The calculations match the measurements very well for medium to high maturity, but are somewhat low for low to medium maturity.

**Kerogen and Oil Composition Modeling in the Maracaibo Basin.** The PMOD calculations to determine pore pressure and expulsion characteristics in the Maracaibo Basin also produce predictions of the composition of the organic matter. The comparison of calculated and measured composition of the source rock and reservoir oil is simplified because only data pertaining to oils recovered from Cretaceous reservoirs, either in the La Luna Formation or the underlying fractured Cogollo Limestone, where secondary migration has been minimal, have been used. Thus in most cases the temperature histories of the reservoir oil have closely tracked that of their respective source rocks. In each case discussed below, the thermal history of the La Luna source rock used in each well modeled in the PMOD calculation was for a depth within 100 m of the depth where material was recovered for the oil, extract, or Rock Eval measurements.

A comparison of the calculated and measured API gravity of Cretaceous oil from 11 different wells is shown in Figure 56 for both the leaky system and closed system cases. For the leaky system case, both the differential (value based on the composition of the expelled oil at a particular time step) and cumulative (value integrated over time) gravity are compared. The measured API gravity agrees very well with the calculated differential gravity, indicating that the composition of the oil in the reservoir is quite similar to the composition of the oil currently being expelled from the source rock or that the expelled oil in the reservoir continues to mature along with the source rock. This conclusion is supported by the good agreement between the measured and predicted API gravity in the closed system calculation.

Measured and calculated  $T_{max}$  as a function of maturation (here indicated by the calculated vitrinite reflectance) is shown in Figure 57. The measured and calculated values of  $T_{max}$  show excellent agreement for %Ro less than 1.0, but the measured values are about 20 °C lower than the calculated ones for the two values of %Ro greater than 1.1. The differences for the higher maturity wells may indicate that the thermal history used for the two wells (UD149 and VLB704) may overestimate the maximum temperature (and the calculated %Ro). The  $T_{max}$  calculation is only affected very slightly by whether it is done for the closed or leaky case or by the value of EPSC.

The hydrogen index (HI) of the La Luna source rock was calculated for 22 different wells. Results of these calculations for the leaky system case are compared with data from Talukdar *et al.* (1989) in Figure 58. The calculated values do not decrease as rapidly with  $T_{max}$  as do the measured ones for  $T_{max}$  above about 440 °C, but the agreement is generally quite good, especially considering the fact that the modeled source rock uses an initial HI value of about 600 mg/g TOC while real source rocks can have considerable variation in their primary generation potential.

Calculated and measured values of the H/C ratio of the remaining organic matter in the La Luna shale are compared in Figure 59 for six wells with different values of maturity. The calculated decrease of H/C ratio with maturity closely matches the measured values.

In PMOD oil composition is handled with 12 different species in the chemistry model. The definition of the species is such that the percent of saturates in the oil (expelled or remaining) can be calculated. For expelled oil, the percent saturates is defined by the ratio of the saturate fraction of the light and medium oil normalized to the sum of the light and medium fractions plus HO3. For extract samples, the light oil fractions are probably lost in the extraction process, so the percent saturates is calculated as above, but for the oil remaining in the rock without the light oil fraction. The percent saturates calculated for expelled oils (leaky system case) and remaining oil (closed system case) are compared with the percent saturate fraction in recovered oil for each individual well as a function of maturity in Figure 60. In each well represented in Figure 60, the reservoired oil was recovered within 100 m of the depth of source rock that was used in the thermal history model. The calculation for the closed system closely matches the measured composition while the leaky system calculation does not. The leaky system calculation represents the composition of the expelled oil assuming that no further thermal degradation occurs, but the closed system calculation represents the composition of oil that is generated, stays with the source rock, and continues to change its composition due to cracking and additional generation of different oil components.

A similar comparison of the calculated and measured percent saturates in extracts for a different set of wells is shown in Figure 61. Because the present-day TOC of the remaining organic matter was known for each of these wells, the initial TOC of the source rock was adjusted so that the final calculated TOC would be within a few percent of the measured value in each case for the extracts. In this case there is little difference between the calculated open system and leaky system cases because the leaky system case is calculated for the oil remaining (not expelled) in the source rock. For low maturities ( $\%Ro < 1.0$ ) the calculated and measured values agree quite well, but there is considerable divergence for the two wells with higher maturity. These two wells, UD149 and VLB704 also had a calculated  $T_{max}$  that was higher than the measured value, suggesting that the maximum temperatures in the thermal histories may be too high. The sediments at each of these wells suffered a large amount of Eocene erosion, so there is a lot of uncertainty in the amount of erosion and the maximum amount of pre-Eocene burial. Another possible explanation for the difference between the measured and calculated values is that the composition of the reservoired oil was strongly affected by pre-Eocene expulsion (see the pressure-time plot for well VLE686 [Figure 50] and C151 [Figure 51]).

The pristane/phytane (Pr/Phy) and phytane/C<sub>18</sub> (Phy/C<sub>18</sub>) ratios can also be calculated for expelled and extracted oil in PMOD. Calculated and measured values of Pr/Phy of oils from Cretaceous reservoirs are compared as a function of  $\%Ro$  in the top of Figure 62. Calculated Pr/Phy values of the expelled oil fraction for the leaky system and of oil remaining for the closed system are almost the same and show a gradual increase with increasing maturity, leveling off when  $\%Ro$  becomes about 1.1. The calculated values are nearly the same because phytane is quickly expelled in the leaky system; all of it goes into the expelled oil and it tends to look the same as for the oil in the closed system. Both pristane and phytane have the same cracking rates in the model, so their ratio will remain constant once cracking becomes dominant. The measured values tend to be lower than the calculated ones, except for the highest maturity. This suggests that the chemistry model either tends to underestimate the amount of phytane or overestimate the amount of pristane. Results for the calculations with the lower value of EPSC were essentially the same as those in Figure 62.

A similar plot, but with measured and calculated  $\text{Phy}/\text{C}_{18}$  as a function of maturity is shown in the bottom of Figure 62. In this case the closed system calculations give slightly lower ratios for  $\%R_o < 1.3$ , with the difference being quite large for the highest maturity. The calculated  $\text{Phy}/\text{C}_{18}$  at the highest maturity goes to zero for the closed system case because phytane undergoes cracking in the model while  $\text{C}_{18}$  does not; thus  $\text{C}_{18}$  can remain while phytane disappears. The calculations match the measured values quite well except for the two lowest values of maturity. The difference between calculated and measured  $\text{Phy}/\text{C}_{18}$  ratios at low maturity are probably due to measurement uncertainty, because the trend of the measured data with increasing maturity is somewhat anomalous. Calculations with the lower value of EPSC resulted in slightly higher values of  $\text{Phy}/\text{C}_{18}$  for the leaky system case. The fact that the calculated  $\text{Phy}/\text{C}_{18}$  ratios match the measured values well while the  $\text{Pr}/\text{Phy}$  ratios do not suggests that the model may be overestimating the amount of pristane in the oils.

The  $\text{Pr}/\text{Phy}$  ratios calculated for extracts are compared with measured values in the top of Figure 63. Calculated values for the leaky system case are not shown because they were all extremely high, reflecting the fact that phytane in the model is easily and quickly expelled, so that at the maturity range shown there is essentially no phytane left in the rock to be extracted and  $\text{Pr}/\text{Phy}$  is very large and  $\text{Phy}/\text{C}_{18}$  is almost zero. For the closed system case shown, the calculated values of  $\text{Pr}/\text{Phy}$  tend to be higher than the measured ones, as was seen in Fig 14. In this closed system case, the expulsion parameters such as EPSC make no difference in the results. Calculated and measured  $\text{Phy}/\text{C}_{18}$  ratios for the extracts are compared in the bottom of Figure 63. In this case there is a lot of scatter in the measured values, but they show general agreement with the calculated ones.

A set of Rock Eval data from well Alturitus 19X is also available for comparison of the PMOD calculation with measured values. In this well the La Luna shale was sampled at 1-3 ft (0.3-1 m) intervals throughout its 210 ft (64 m) thickness and Rock Eval analyses were done on each sample. No thermal history for this well had been provided by INTEVEP, so one was estimated based on information from nearby wells and the known present-day depths of the La Luna Formation. A comparison of the calculated Rock Eval parameters for the center of the section with the range of measured values is given in Table 20. For both the leaky and closed system cases, the original TOC for the calculation was 4.0%. Clearly, even though the  $T_{\text{max}}$  is the same for both calculations, the leaky system model matches the range of measured values much better. For the leaky system calculation, the fact that the HI is high and S1 low (making PI low) suggests that the calculated maturity might be a little bit high and that the thermal history needs to be adjusted to slightly lower temperatures.

The trend, with increasing maturity, of the gas wetness index ( $\text{CHX}/(\text{CHX}+\text{CH}_4)$ ) for the closed system case is shown in Figure 64. During the oil generation phase the ratio increases rapidly as the  $\text{C}_2\text{-C}_4$  fraction is generated and then begins to gradually decrease as cracking and other  $\text{CH}_4$  production increases for  $\%R_o > 0.9$ .

## SUMMARY AND CONCLUSIONS

Over the five years of Annex XII work, substantial progress was made in techniques for and understanding of kinetic modeling of petroleum generation and expulsion. These advances have been incorporated into experimental equipment and computer software for future application in other areas.

The programmed micropyrolysis technique for measuring total hydrocarbon generation kinetics was developed in collaboration with two small American businesses, Lab Instruments of Kenwood CA and Humble Instruments and Services of Humble TX, and the KINETICS software for determining activation energy distributions from this data was developed at LLNL and licensed to these companies for commercial distribution. The Humble Instruments system and KINETICS software were installed at the INTEVEP research laboratory in Los Teques. These equipment and software were used to show that the global hydrocarbon generation kinetics for most petroleum source rocks, including those from the La Luna formation, have a modest activation energy distribution with a mean activation energy in the low to mid 50 kcal/mol range. Extrapolation of the kinetic parameters to typical geological heating rates predicts oil formation in the 100-150 °C region. A preliminary comparison of observed and calculated source rock maturity using these parameters was consistent with available geologic evidence.

Separate oil and gas generation kinetics were determined at LLNL under conditions similar to those used in the preceding paragraph. Oil generation kinetics were measured by monitoring the amount of oil evolved from a self-purging reactor as a function of time. It was demonstrated that activation energy distributions are needed for oil alone. The gas generation kinetics were determined using tandem mass spectrometric analysis of the evolved gases. The gas generation characteristics of the La Luna source rock were determined to be similar to those of other marine source rocks. Of the several samples examined, the La Luna kinetics are most similar to those of the Posidonia shale, whose composition is also about carbonate minerals.

Hydrous pyrolysis conducted at INTEVEP are more similar to the natural generation process than atmospheric-pressure pyrolysis experiments performed at LLNL. Initial hydrous pyrolysis experiments measured gas and total bitumen yields as a function of temperature for 72 h pyrolysis. The gas generation in these experiments was similar to that predicted from the atmospheric-pressure pyrolysis experiments, except for CO<sub>2</sub>. Water enhances early CO<sub>2</sub> formation. The relative contributions of organic and inorganic CO<sub>2</sub> were not determined directly, but elemental balance calculations carried out during detailed mechanism development indicate that most of the early CO<sub>2</sub> probably comes from organic matter. Total bitumen formation also occurs with a mean activation energy in the low 50 kcal/mol range, but the larger frequency factor results in earlier generation than predicted by the programmed micropyrolysis experiments. Later experiments where oil expelled from the rock chips was collected separately from the remaining bitumen confirmed prior observations of Lewan (1985) that oil expulsion lags bitumen generation. It was demonstrated in this work that the kinetics for formation of expelled oil are very similar to those measured by the programmed micropyrolysis. Finally, kinetics for cracking of oil to gas were estimated from experiments at the highest temperatures and times.

Mathematical models of source rock compaction and petroleum expulsion were formulated and implemented into two computer programs, PYROL and PMOD. PYROL was

developed prior to the Annex XII work for interpreting oil shale pyrolysis experiments. It was initially used in the Annex XII work to demonstrate that the temperature dependence of oil vaporization may lead to a 1-2 kcal/mol overestimation of the generation activation energy by typical programmed pyrolysis. This resulted in a suggested correction to the programmed micropyrolysis kinetics whereby the activation energies are decreased by 2 kcal/mol and a compensating decrease of 4· is made in the frequency factor. Predicted temperatures for geologic oil formation are about 6 °C lower with this correction, but it is difficult to confirm or deny this correction because of the limitations of paleothermal histories. A modified RKS equation of state was added to PYROL to calculate gas-liquid equilibria for the hydrocarbon phase. A simple model of rock compaction was also added. Simultaneous integration of the relevant equations demonstrated that oil and gas generation contributes substantially to overpressuring and inhibits source rock compaction. These calculations showed that gaseous and liquid hydrocarbons were contained in a single phase under most conditions of interest. Lessons learned with PYROL were incorporated into PMOD. PMOD does not calculate liquid vaporization, so it cannot model some important aspects of laboratory experiments, but it is substantially easier to use and automatically calculates many properties of interest to geochemists and geologists. The rock compaction model in PMOD was also refined. A detailed chemistry mechanism was derived for PMOD using data from the various laboratory experiments.

PMOD model calculations for generic geological conditions found that the combination of an early bitumen product and low porosities can lead to expulsion of a heavy oil, in agreement with general observations in the Maracaibo basin. The most important variables affecting expelled oil quality are the porosity during generation and the initial TOC. In fact, most oil properties correlate well with the ratio of TOC/porosity. This ratio is inversely related to the residence time of the oil and bitumen in the source rock and determines the extent of secondary oil maturation reactions. Higher maturities favor higher API gravity, higher saturate content, and lower sulfur content.

A detailed comparison between PMOD calculations and measured properties was made for specific wells in the Maracaibo Basin. Calculated and measured values of API gravity of reservoir oil, H/C and Tmax of remaining organic matter, and percent saturates, Pr/Phy, and Phy/C18 of oils and extracts show extremely good agreement. With the exception of Pr/Phy and Phy/C18 ratios, the best agreement of the model with the data is for the closed system case. This supports the original intent of the model validation, which was to make a comparison where the expelled oil has not traveled far from the source rock and has continued to mature along with it. Given the uncertainties in the thermal history models that went into the PMOD calculations, the agreement between the model and the "real world" is very good. This comparison validates the chemistry model as a means of characterizing the generation and expulsion characteristics of the hydrocarbons from the La Luna shale. The real power in the application of the model will be when it is used to further refine thermal history models and expulsion characteristics for individual source rock-reservoir systems. It should be noted that PMOD is capable of calculating a whole host of properties that may be of interest to the exploration geologist or reservoir engineer.

## REFERENCES

- Braun, R. L., A. K. Burnham and J. J. Sweeney (1988) Petroleum Geochemistry Project Annual Report, Oct. 1987-Sept. 1988, LLNL Report UCID-21303-88-4.
- Braun, R. L., and A. K. Burnham (1987) Analysis of chemical reaction kinetics using a distribution of activation energies and simpler models, *Energy & Fuels* **1**, 153-161.
- Braun, R. L., and A. K. Burnham (1990a) Mathematical model of oil generation, degradation, and expulsion, *Energy & Fuels* **4**, 132-146.
- Braun, R. L., and A. K. Burnham (1990b) *KINETICS: A Computer Program to Analyze Chemical Reaction Data*, LLNL Report UCID-21588 Rev. 1.
- Braun, R. L., A. K. Burnham, J. G. Reynolds, and J. E. Clarkson (1991) Pyrolysis kinetics for lacustrine and marine source rocks by programmed micropyrolysis, *Energy & Fuels* **5**, 192-204.
- Braun, R. L., and A. K. Burnham (1992) PMOD: A flexible model of oil and gas generation, cracking, and expulsion, LLNL Report UCRL-JC-105371 Rev. 1, submitted to *Advances in Organic Geochemistry 1991*.
- Burnham, A. K., and M. F. Singleton (1983) High-pressure pyrolysis of Green River oil shale, *Geochemistry and Chemistry of Oil Shales, ACS Symp. Ser. 230*, F. P. Miknis and J. F. McKay, eds., American Chemical Society, Washington, pp. 335-351.
- Burnham, A. K. and R. L. Braun (1985) General kinetic model of oil shale pyrolysis, *In Situ* **9**, 1-23.
- Burnham, A. K., R. L. Braun, H. R. Gregg, and A. M. Samoun (1987a) Comparison of methods for measuring kerogen pyrolysis rates and fitting kinetic parameters, *Energy & Fuels* **1**, 452-458.
- Burnham, A. K., R. L. Braun and J. J. Sweeney (1987b) *Annual Report, Petroleum Geochemistry*, LLNL Report UCID-21243.
- Burnham, A. K., R. L. Braun, and A. M. Samoun (1988) Further comparison of methods for measuring kerogen pyrolysis rates and fitting kinetic parameters, *Advances in Organic Geochemistry 1987, Org. Geochem.* **10**, 839-845.
- Burnham, A. K., and J. J. Sweeney (1989) A chemical kinetic model of vitrinite maturation and reflectance, *Geochim. Cosmochim. Acta* **53**, 2649-2657.
- Burnham, A. K., and R. L. Braun (1990) Development of a detailed model of petroleum formation, destruction, and expulsion from lacustrine and marine source rocks, *Advances in Organic Geochemistry 1989, Org. Geochem.* **16**, 27-40.

Burnham, A. K. (1991) Oil evolution from a self-purging reactor: kinetics and composition at 2 °C/min and 2 °C/h, *Energy & Fuels* **5**, 205-214.

Burnham, A. K. (1990) *Pyrolysis Kinetics and Composition for Posidonia Shale*, LLNL Report UCRL-ID-105871.

Hubbert, M.K., and W. W. Rubey (1959) Role of fluid pressure in mechanics of overthrust faulting. I. Mechanics of fluid-filled porous solids and its application to overthrust faulting. *Geol. Soc. America Bull.* **70**, 115-166.

Huizinga, B. J., Z. A. Aizenshtat and K. E. Peters (1988) Programmed pyrolysis-gas chromatography of artificially matured Green River kerogen, *Energy & Fuels* **2**, 74-81.

Lerche, I. (1990) *Basin Analysis, Quantitative Methods, Volume 1*, Academic Press, p. 239.

Lewan, M. D., J. C. Winters and J. H. McDonald (1979) Generation of oil-like pyrolysates from organic-rich shales, *Science* **203**, 897-899.

Lewan, M. D. (1985) Evaluation of petroleum generation by hydrous pyrolysis experimentation. *Phil. Trans. Roy. Soc. Lond.* **A315**, 123-134.

McAulliffe, C. D. (1979) Oil and gas migration-chemical and physical constraints. *AAPG Bulletin* **63**, 761-781.

Palciauskas, V.V. and P.A. Domenico (1980) Microfracture development in compacting sediments: relation to hydrocarbon-maturation kinetics, *AAPG Bulletin* **64**, 927-937.

PennWell (1990) *Oil and Gas Journal Data Book*, Pennwell Publishing Co., Tulsa, OK.

Philippi, G. T. (1965) On the depth, time and mechanism of petroleum generation, *Geochem. Cosmochim. Acta* **29**, 1021-1049.

Reynolds, J. G., R. W. Crawford and A. K. Burnham (1991) Analysis of oil shale and petroleum source rock pyrolysis by triple quadrupole mass spectrometry: Comparisons of gas evolution at the heating rate of 10 °C/min, *Energy & Fuels* **5**, 507-523.

Reynolds, J. G., and A. Murray (1991) *Pyromat II Micropyrolysis of Source Rocks and Oil Shales: Effects of Native Bitumen Content and Sample Size on  $T_{max}$  Values and Kinetic Parameters*, LLNL Report UCRL-ID-106505.

Sweeney, J. J., A. K. Burnham and R. L. Braun (1985) A model of hydrocarbon maturation in the Uinta Basin, Utah, USA, *Modeling the Thermal Evolution of Sedimentary Basins*, Editions Technip, Paris, pp. 547-561.

Sweeney, J. J., A. K. Burnham and R. L. Braun (1987) A model of hydrocarbon generation from Type I kerogen: application to Uinta Basin, Utah, *AAPG Bulletin* **71**, 967-985.

Sweeney, J. J. (1989) *FORTRAN Programs for Basin Analysis and Petroleum Generation Modeling*, LLNL Report UCID-21859.

Sweeney, J. J., and A. K. Burnham (1990) Evaluation of a simple model of vitrinite reflectance based on chemical kinetics, *AAPG Bulletin* **74**, 1559-1570.

Sweeney, J. J. (1990) BASINMAT: FORTRAN program calculates oil and gas generation using a distribution of discrete activation energies, *Geobyte*, April 1990, pp. 37-43.

Sweeney, J., S. Talukdar, A. Burnham, and C. Vallejos (1990) Pyrolysis kinetics applied to prediction of oil generation in the Maracaibo Basin, Venezuela, *Advances in Organic Geochemistry 1989, Org. Geochem.* **16**, 189-196.

Talukdar, S., O. Gallango, and M. Chin-A-Lien (1986) Generation and migration of hydrocarbon migration of oil in the Maracaibo Basin, Venezuela: an integrated basin study. *Advances in Organic Geochemistry 1985, Org. Geochem.* **10**, 261-279.

Talukdar, S., O. Gallango, C. Vallejos, and A. Ruggerio (1987) Observations on the primary migration of oil in the La Luna source rocks of the Maracaibo Basin, Venezuela, *Migration of Hydrocarbons in Sedimentary Basins*, Editions Technip, Paris, pp. 59-78.

Talukdar, S., C. Vallejos, and A. Ruggerio (1989) Primary migration and expulsion efficiency of oil in La Luna source rocks of the Maracaibo Basin, Venezuela (Abstract #85), 14th International Meeting on Organic Geochemistry, Paris, September 18-22.

Ungerer, P., J. Espitalie, F. Behar, and S. Eggen (1988) Mathematical modelling of the interactions between thermal cracking and migration in the formation of oil and gas, *C.R. Acad. Sci. Paris* **307, Series II**, 927-934.

Waples, D. W. (1984) Time and temperature in petroleum formation, *Advances in Petroleum Geochemistry*, v. 1, J. Brooks and D. Welte, eds., Academic Press, London, pp. 7-67.

Table 1. Chemical analysis of La Luna rock samples

Parameter	QL7	26D2	26D2'	QLN
Elemental Analysis (wt%)				
total carbon	17.8		11.7	
mineral carbon	6.7		10.9	
organic carbon	11.2	6.1	0.85	4.6
total hydrogen	1.3		0.2	
total nitrogen	0.4		0.2	
total sulfur	1.4		0.14	
Rock Eval Analysis				
T <sub>max</sub> (°C)	426	437	429	429
S1 (mg/g shale)	0.8		0.9	0.5
S2 (mg/g shale)	73.0		5.0	25.0
TOC (wt%)	7.8		0.9	4.1
HI (from RE TOC)	939		559	595
HI (from EA TOC)	654		586	549

Table 2. Summary of Rock Eval Kinetic Analysis

Analysis Desig.	Samoun 871011	Samoun 880721	Jarvie 880724		
<u>AP22 Standard</u>					
T correction (°C)	26.82 + 0.0325 H <sub>r</sub>	1.91 + 0.0244 H <sub>r</sub>	1.69 + 0.0169 H <sub>r</sub>		
A <sub>approx</sub>	9.3e12	8.2e12	2.1e13		
E <sub>approx</sub>	50.87	50.78	52.09		
A <sub>discrete</sub>	4.4e13	3.9e13	3.4e14		
f <sub>1</sub> , E <sub>1</sub>	6.3, 49	6.4, 49	3.8, 51		
f <sub>2</sub> , E <sub>2</sub>	89.3, 53	89.8, 53	94.4, 56		
<u>La Luna</u>					
	QL7	QL7	26D2'	QL7	26D2'
A <sub>approx</sub>	8.7e12	7.1e11	4.0e12	2.7e12	1.2e12
E <sub>approx</sub>	49.74	46.42	49.11	48.46	47.81
σ <sub>approx</sub>	2.7	2.1	2.6	1.4	2.0
T <sub>max</sub> , 25 °C/min	462	466	469	470	476
A <sub>discrete</sub>	3.7e12	7.2e11	2.2e14	2.7e12	6.1e11
f <sub>1</sub> , E <sub>1</sub>	6.4, 46	8.8, 44	8.8, 53	73.1, 48	40.6, 46
f <sub>2</sub> , E <sub>2</sub>	12.9, 47	49.6, 46	20.3, 54	3.0, 49	32.8, 47
f <sub>3</sub> , E <sub>3</sub>	28.7, 48	22.3, 47	26.7, 55	16.5, 50	10.6, 48
f <sub>4</sub> , E <sub>4</sub>	29.9, 49	7.2, 48	13.3, 56		
T <sub>max</sub> , 25 °C/min	462.5	467	469	470	476.5

Table 3. Approximate analysis of all 1988 Rock-Eval Data for La Luna source rocks

---

**Sample QL7**

*Data Input:*

	Hr (C/min)	T <sub>max</sub> (C)	FWHH (C)
Exp #1	5.06	431.44	59.52
Exp #2	27.84	461.87	75.17
Exp #3	55.44	480.00	80.51
Exp #4	5.41	434.92	60.16
Exp #5	16.27	456.74	65.35
Exp #6	29.79	468.90	70.17
Exp #7	60.11	487.58	70.62
Exp #8	4.94	437.31	56.63
Exp #9	14.94	460.07	58.32
Exp #10	31.80	474.03	56.06
Exp #11	54.20	488.14	57.56

*Data Output:*

	T <sub>max</sub> (C)
Avg E = 46900 cal/mole	433.4
sigma = 3.1 % avg E	469.1
Avg A = 9.2e11 s <sup>-1</sup>	484.6
	434.8
	457.5
	470.6
	486.4
	432.9
	455.7
	472.1
	484.0

**Sample 26D2**

*Data Input:*

	Hr (C/min)	T <sub>max</sub> (C)	FWHH (C)
Exp #1	5.41	438.48	67.68
Exp #2	16.23	460.42	73.90
Exp #3	29.78	473.09	70.54
Exp #4	60.00	488.25	72.27
Exp #5	4.94	442.80	64.18
Exp #6	14.94	465.54	65.72
Exp #7	31.80	480.09	66.04
Exp #8	54.20	495.18	68.18

*Data Output:*

	T <sub>max</sub> (C)
Avg E = 47030 cal/mole	440.6
sigma = 3.2 % avg E	463.6
Avg A = 7.5e11 s <sup>-1</sup>	477.0
	493.0
	438.8
	461.9
	478.5
	490.6

---

Table 4. Summary of Pyromat kinetic parameters for La Luna samples

	QL7	QLN	26D2'
A <sub>approx</sub>	3.0e13	5.5e12	4.6e11
E <sub>approx</sub>	51.4	49.1	45.9
σ <sub>approx</sub>	2.3	1.1	2.8
T <sub>max</sub> , 25°C/min	463	468	470
A <sub>NLR</sub>	5.1e13	1.6e13	1.6e12
E <sub>NLR</sub>	52.1	50.7	47.5
σ <sub>NLR</sub>	2.7	1.9	3.3
T <sub>max</sub> , 25°C/min	462	467	466
A <sub>discrete</sub>	6.0e13	1.6e13	1.2e12
40			5.7
41			
42			4.9
43	0.1		1.5
44	0.2		7.4
45	0.7	0.6	3.1
46	0.1	0.6	17.0
47	1.9	1.8	<b>30.4</b>
48			18.2
49	2.3		8.2
50	7.7	<b>52.7</b>	2.7
51	5.4	23.7	
52	<b>45.9</b>	16.3	
53	17.6	2.1	1.0
54	9.2		
55	5.9		
56	0.4	2.3	
57	1.1		
58	0.9		1.5
59			
60	0.6		

Table 5. Material balance for oil evolution experiments in the LLNL self-purging reactor

	QL7		26D2	
	2°C/min	2°C/h	2°C/min	2°C/h
mass % in:				
residue	90.7	91.9	99.0	99.1
oil	5.9	4.7	0.54	0.47
water	2.0	1.8	0.3	0.3
gas+loss	1.4	1.6	0.7	0.6
oil composition				
wt % C	80.8	80.9		
wt % H	10.7	11.0		
wt % N	0.6	0.9		
wt % S	6.8	6.4		
remainder	1.3	0.8		
mol H/C	1.57	1.61		
oil density	0.933	0.920		
acid CO <sub>2</sub> loss	1.2	0.5		
% TOC in:				
residue	53	43		
oil	43	34		
gas+loss	5	7		

Table 6. Kinetic parameters derived for sample QL7 from oil evolution data.

A <sub>approx</sub>	4.9e14
E <sub>approx</sub>	55.5
σ <sub>approx</sub>	2.9
A <sub>NLR</sub>	6.3e14
E <sub>NLR</sub>	55.7
σ <sub>NLR</sub>	2.7
A <sub>discrete</sub>	8.2e14
46	0.4
52	10.4
55	20.5
56	20.8
57	<b>40.9</b>
58	4.6
62	2.5

Table 7. Composition of evolved oils from sample QL7

	2°C/min	2°C/h
<i>Gas chromatography</i>		
mg/g TOC		
pristane	0.38	0.31
1-pristene	0.24	0.08
n-C <sub>17</sub>	0.94	1.20
1-C <sub>17</sub>	0.55	0.28
phytane	0.37	0.45
n-C <sub>18</sub>	0.81	1.31
1-C <sub>18</sub>	0.49	0.29
ratios		
pr/C <sub>17</sub>	0.42	0.21
ph/C <sub>18</sub>	0.28	0.28
pr/ph	1.7	0.86
% of orig TOC		
n-alkenes	1.86	2.79
1-alkenes	1.46	0.95
tot normal	3.32	3.74
<i>Carbon NMR</i>		
<sup>13</sup> C aromaticity	0.41	0.34
% of orig TOC		
arom	17.4	11.5
br + cycl	12.8	13.4
normal	12.4	8.9
fraction of normal C		
C <sub>1</sub>	0.18	0.185
C <sub>2</sub>	0.18	0.195
C <sub>3</sub>	0.14	0.13
C <sub>n</sub>	0.50	0.49
chain length		
Eq. 1 <sup>a</sup>	12.1	11.8
Eq. 2 <sup>b</sup>	11.1	10.8
<i>Proton NMR</i>		
% of oil H		
arom	7.1	7.2
olefin	1.2	1.0
aliph	91.6	91.7
% of aliph H		
methyl	23	21
methylene	51	49
benzyl	22	26

Table 8. Species from programmed pyrolysis monitored by the triple-quadrupole mass spectrometer (TQMS)

Hydrocarbons		O and N Compounds		S Compounds	
H <sub>2</sub>	2	H <sub>2</sub> O	18	H <sub>2</sub> S	34/32
CH <sub>4</sub>	16, 16/14	CO	28/84	CH <sub>3</sub> SH	48/45
C <sub>2</sub> H <sub>4</sub>	26, 28/26	CH <sub>3</sub> CO	43/16	COS	60/32
C <sub>2</sub> H <sub>6</sub>	30, 30/27	CO <sub>2</sub>	44/16	C <sub>2</sub> H <sub>5</sub> SH	62/29
C <sub>3</sub> H <sub>6</sub>	42, 42/39	CH <sub>3</sub> COOH	60/45	CH <sub>3</sub> SCH <sub>3</sub>	62/47
C <sub>3</sub> H <sub>8</sub>	44/29	C <sub>4</sub> H <sub>5</sub> N	67/40	SO <sub>2</sub>	64/48
C <sub>4</sub> H <sub>8</sub>	56	C <sub>5</sub> H <sub>5</sub> N	79/52	CS <sub>2</sub>	76/32
C <sub>4</sub> H <sub>10</sub>	58	C <sub>6</sub> H <sub>5</sub> OH	94/65	C <sub>3</sub> H <sub>7</sub> SH	76/42
C <sub>5</sub> H <sub>10</sub>	70			C <sub>4</sub> H <sub>4</sub> S	84/45
C <sub>5</sub> H <sub>12</sub>	72			CH <sub>3</sub> C <sub>4</sub> H <sub>4</sub> S	97/53
C <sub>6</sub> H <sub>6</sub>	78/52				
C <sub>6</sub> H <sub>12</sub>	84/56				
C <sub>6</sub> H <sub>14</sub>	86				
CH <sub>3</sub> C <sub>6</sub> H <sub>5</sub>	92/91				
C <sub>7</sub> H <sub>10</sub>	94/79				

Table 9. Activation energy distributions for individual species evolved from sample QL7, derived by constraining A to  $3 \times 13 \text{ s}^{-1}$ . Components with less than 1% of the reaction were combined.

E	CH <sub>4</sub>	CH <sub>x</sub>	H <sub>2</sub>	H <sub>2</sub> S	Methio	m/z=57	CH <sub>3</sub> COOH
36							2.2
37							
38							3.4
39							
40							1.8
41		1.1					1.5
42				1.5			
43							3.2
44		1.1			1.1		4.4
45							
46	1.0	1.8		4.6	2.3	1.5	9.4
47		1.0		1.6	3.7		4.3
48	1.7	3.5		9.4	11.5	4.7	12.5
49		6.8		23.2	3.9	2.0	19.2
50	2.9	3.9		32.6	25.8	12.4	19.5
51	5.4	22.8	11.6	17.1	18.1	24.1	
52	5.6	10.8	24.6	5.4	19.3	14.6	9.2
53	4.6	10.2				30.1	
54	2.1	19.7	9.7	2.7	8.1	2.6	4.6
55	17.0	4.4	11.0		1.8	3.7	
56		6.8	14.2	0.9	1.2	2.0	2.3
57	12.5				1.2		
58	6.3	3.0		1.0			
59	6.1	1.4	28.9		1.8	2.1	
60	8.7						
61	3.1						
62	6.2						
63	6.1						
64		1.7					
65	6.8						
66							
67							
68	3.9						

Table 10. Hydrous pyrolysis of sample JGE28 for 72 h

Exp #	T Extract (°C)	Extract Remaining (ppm)	Remaining TOC (wt%)	H/C	Tmax (°C)	Gas chrom.		Liq. chrom. (%)		Mass spec. (mg/g TOC)							
						pr/17	ph/18	pr/ph	sat	aro	i+a	CH <sub>4</sub>	CH <sub>x</sub>	H <sub>2</sub>	CO <sub>2</sub>	H <sub>2</sub> S	
orig		958	0.85		431	1.01	1.37	0.63	21	22	57						
CV-33	260	912	0.89	1.07	441	0.57	0.68	0.49	22	26	52	0.0	0.0	0.6	96.4	5.1	
CV-34	270	893	0.83	1.03	443	0.87	0.97	0.68	26	28	46	0.6	0.0	0.4	91.0	6.6	
CV-35	280	920	0.83	1.02	443	0.82	0.99	0.67	24	24	52	1.0	0.9	0.6	96.4	5.2	
CV-36	290	960	1.77	0.92	445	0.79	0.93	0.65	23	31	46	1.1	1.3	0.9	78.7	12.5	
CV-37	300	970	1.73	1.00	445	0.73	0.80	0.67	32	31	37	1.3	1.7	1.0	85.6	12.9	
CV-38	310	965	1.66	0.94	449	0.65	0.66	0.88	31	32	37	2.0	4.5	2.2	88.3	16.1	
CV-39	320	1820	1.65	0.90	449	0.63	0.59	0.67	42	30	28	5.0	9.6	4.8	84.2	17.9	
CV-40	330	4600	0.82	0.70	466	0.30	0.31	0.50	34	32	34	4.8	12.6	11.3	100.4	25.8	
CV-41	340	2046	1.18	0.63	441	0.45	0.40	0.92	36	26	38	6.8	13.5	7.9	108.7	79.1	
CV-42	350	1248	1.42	0.54	525	0.32	0.32	1.07	42	25	33						
CV-43	375	1106	1.52	0.51	550	0.48	0.48	0.59	43	30	26						

Table 11. Hydrous pyrolysis of sample QL7 for 72 h

Exp #	T Extract (°C)	Extract (ppm)	Remaining TOC (wt%)	H/C	Tmax (°C)	Gas chrom.		Liq. chrom. (%)		Mass spec. (mg/g TOC)							
						pr/17	ph/18	pr/ph	sat	aro	r+a	CH4	CHx	H2	CO2	H2S	
orig	22200	11.2		1.25	431	2.54	4.97	0.22	5	27	69						
CV-8	200	20300	11.5	1.26	433	2.28	4.81	0.44	7	37	56						
CV-6	250	26800	9.5	1.22	431	1.98	4.27	0.39	6	37	57	1.1	0.4	1.5	22.1	1.0	
CV-23	260	23700	10.2	1.20	433	1.19	2.13	0.59	6	34	60	0.2	0.3	0.2	24.5	2.9	
CV-21	270	29800	10.1	1.23	433	1.20	2.25	0.50	5	32	63	0.4	1.1	0.3	67.2	2.7	
CV-17	280	32400	9.4	1.17	435	1.19	2.21	0.52	5	25	70	0.5	0.9	0.4	81.3	6.0	
CV-19	290	50000	8.8	1.13	433	1.01	1.50	0.76	6	35	59	0.9	2.0	0.9	120.1	9.5	
CV-4	300	73600	5.3	1.01	437	1.39	1.32	0.98	6	25	69	1.5	3.7	1.1	103.3	11.6	
CV-18	310	93100	5.1	0.88	439	0.99	1.06	0.89	13	27	60	2.7	3.3	1.7	113.6	6.8	
CV-16	320	82000	4.7	0.87	437	0.90	1.00	0.81	16	24	60	2.9	12.8	2.0	102.6	19.9	
CV-20	330	64000	6.5	0.79	445	0.68	0.56	1.29	18	33	49	4.8	18.3	3.0	96.0	24.4	
CV-22	340	46800	6.1	0.67	455	0.48	0.52	0.86	27	35	38	6.7	21.1	3.4	143.7	24.3	
CV-5	350	40400	5.8		453	0.44	0.37	1.27	35	40	25	4.0	9.7	2.9	275.1	31.4	
CV-13	375	21000	5.4	0.57	500	0.07	0.06	1.14	20	58	22	26.3	48.8	13.5	580.3	60.5	
CV-9	400	12400	6.7	0.48	550				9	71	20	89.0	248	3.6	652.5	103	

Table 12. Hydrous pyrolysis of sample 26D2 for 72 h

Exp #	T (°C)	Extract (ppm)	Remaining TOC (wt%)	Tmax (°C)	Gas chrom.		Liq. chrom. (%)			
					pr/17	ph/18	sat	aro		
orig		6057	5.5	437	0.34	0.53	0.51	5	15	80
HPA-1	255	6075	4.9	437	0.36	0.56	0.44	4	24	72
HPA-2	260	6094	4.7	437	0.30	0.44	0.44	6	27	67
HPA-3	270	6045	5.1	439	0.28	0.50	0.57	5	28	67
HPA-4	280	6139	5.1	439	0.33	0.45	0.66	8	27	65
HPA-5	290	6076	4.9	435	0.32	0.47	0.59	13	36	51
HPA-6	300	9383	4.4	439	0.33	0.37	0.79	18	35	47
HPA-7	310	10311	4.1	439	0.31	0.33	0.92	21	42	37
HPA-8	320	13709	4.0	441	0.32	0.28	1.13	24	39	37
HPA-9	330	11905	3.6	441	0.23	0.21	1.14	30	37	32
HPA-10	340	9175	3.3	445	0.22	0.25	0.72			
HPA-11	350	8949	3.4	449	0.18	0.16	0.84			
HPA-13	400	2670		550	0.38	0.45	0.61	9	53	38

Table 13. Hydrous pyrolysis of sample 26D2' for various times (GC=gas chrom., LC=liq. chrom.)

Exp #	T (°C)	Time (h)	Bit (ppm)	Oil (ppm)	Tmax (°C)	S1 (mg/g)	S2 (ex sh)	GC of oil			GC of bit			LC of oil			LC of bit		
								pr/17	ph/18	pr/ph									
orig			7472		431	0.17	1.64					0.54	0.84	0.38				22	31
HPC-1	280	72	5693	1478	433	0.01	1.32	0.78	0.85	0.56	0.51	0.77	0.38	39	29			18	32
HPC-10	280	216	4035	2859	435	0.02	1.27	0.52	0.78	0.49	0.56	0.74	0.47	52	28			26	37
HPC-5	320	24	4881	2220	439	0.02	1.21	0.58	0.80	0.54	0.48	0.67	0.46	50	29			18	37
HPC-2	320	72	3730	3210	439	0.03	0.88	0.48	0.60	0.61	0.35	0.46	0.43	40	30			18	39
HPC-6	320	216	1862	4671	439	0.03	0.62	0.43	0.50	0.77	0.63	0.39	1.03	57	38			37	43
HPC-7	340	24	3007	3444	439	0.03	0.95	0.47	0.70	0.57	0.48	0.39	0.59	57	25			16	38
HPC-3	340	72	1423	3820	443	0.03	0.50	0.41	0.58	0.59	0.40	0.48	0.55	62	20			24	45
HPC-8	370	24	633	5017	453	0.04	0.20	0.25	0.28	0.85	0.30	0.36	0.45	37	35			16	29
HPC-4	370	72	420	4838	500	0.07	0.07	0.23	0.39	0.63	0.21	0.27	0.30	48	40			21	29
HPC-9	370	216	346	2256	543	0.07	0.07	0.03	0.06	0.39	0.41	0.29	0.81	7	63			23	61

Table 14. Hydrous pyrolysis of sample QLN for various times

Exp #	T (°C)	Time (h)	Bit (ppm)	Oil (ppm)	TOC* (%)	Tmax (°C)	LC of bitumen (%)			EA of bitumen (%)			EA of heavy oil (%)					
							sat	aro	res	asf	C	H	N	S	C	H	N	S
orig			11910		3.4	429	6	25	25	44								
HPN-5	280	72	11877	1790	3.6	430	6	28	23	43	79.2	8.9	1.5	7.6	74.5	9.1	0.7	
HPN-9	280	216	23651	1880	3.7	433	7	34	23	36	78.8	8.7	1.5	7.3	76.1	8.7	1.1	
HPN-1	310	24	16651	1273	3.2	429	5	24	24	47	79.3	8.8	1.5	7.2				
HPN-I	310	72	25484	4175	2.5	433	15	30	13	42					79.0	9.9	0.7	6.2
HPN-2	310	216	13274	9320	2.2	433	9	33	25	33	80.0	8.5	1.5	6.7	80.2	9.2	1.1	
HPN-4	340	24	10856	18533	1.8	437	6	35	37	22	78.7	8.2	1.5	7.1	81.5	10.2	0.7	6.1
HPN-3	340	72	5534	14970	2.1	442	13	43	30	14	79.0	7.8	1.6		80.7	10.1	0.6	
HPN-6	370	24	4758	16873	2.6	456	13	42	28	17	78.0	7.6	1.5		81.0	9.3	0.7	6.6
HPN-7	370	72	3381	11940	2.5	520	12	41	26	21	76.4	6.9	1.5		80.4	7.8	0.9	7.3
HPN-8	370	216	3018	6800	2.6	539	11	66	20	3								

\*after extraction

Table 15. Gas analysis of HPC and HPN series hydrous pyrolysis experiments. Other data are given in Tables 13 and 14.

Exp #	T (°C)	Time (h)	Mass spec. (mg/g TOC)				
			CH <sub>4</sub>	CH <sub>x</sub>	H <sub>2</sub>	CO <sub>2</sub>	H <sub>2</sub> S
HPC-8	370	24	10.5	39	0.3	238	11
HPC-4	370	72	17.1	54	1.1	283	10
HPC-9	370	216	39.7	144	4.7	1280	42
HPN-5	280	72	0.3	2	0.4	27	1
HPN-2	310	216	4.3	17	2.4	30	6
HPN-4	340	24	4.9	52	1.9	161	18
HPN-3	340	72	8.0	98	2.5	254	25
HPN-6	370	24	14.2	55	3.8	71	24
HPN-7	370	72	26.0	104	4.1	150	28
HPN-8	370	216	40.6	152	2.8	145	33

Table 16. PMOD is written in a modular form to provide flexibility.

---

PMOD.BAT	Calls a series of programs that set up and solve the problem
CONMOD.EXE <sup>a</sup>	Writes a control file (*.con) that gives the file names of all input
KEMMOD.EXE	Derives and writes a file (*.kem) defining the chemical kinetic mechanism
FIZMOD.EXE <sup>a</sup>	Writes a file (*.fiz) giving physical properties (TOC, porosity, equation-of-state parameters, etc.) and expulsion criteria
HISMOD.EXE <sup>a</sup>	Writes a file (*.his) giving t, T, and P or depth history
MISMOD.EXE <sup>a</sup>	Writes a file (*.mis) giving numerical integration tolerances, output specs, etc. <sup>a</sup> previous files could be easily modified with a text editor instead
SOLMOD.EXE	Solves ODE system and calculates maturation parameters of interest
PLOTPMOD.BAT	Calls appropriate programs and subroutines to create plots

---

Table 17. Chemical species allowed in PMOD

---

Fluid Species

HO1	Heavy oil 1	CHX	C <sub>2</sub> -C <sub>4</sub> gas
HO2	Heavy oil 2	CH4	methane
HO3	Heavy oil 3	H2	molecular hydrogen
MO1	Medium oil 1	N2	molecular nitrogen
MO2	Medium oil 2	CO2	carbon dioxide
MO3	Medium oil 3	CO	carbon monoxide
LO1	Light oil 1	H2S	hydrogen sulfide
LO2	Light oil 2	NH3	ammonia
LO3	Light oil 3	H2O	water
NA1	Naphtha 1		
NA2	Naphtha 2		
NA3	Naphtha 3		

Solid Organic Species

KER1	organic solid 1	RESC	Residual organic carbon
KER2	organic solid 2	RESH	Residual organic hydrogen
KER3	organic solid 3	RESO	Residual organic oxygen
KER4	organic solid 4	RESN	Residual organic nitrogen
KER5	organic solid 5	RESS	Residual organic sulfur
KER6	organic solid 6		
KER7	organic solid 7		
KER8	organic solid 8		
KER9	organic solid 9		

Solid Inorganic Species

INRT	inert mineral matrix
MIN1	*volatilizable mineral component 1
MIN2	*volatilizable mineral component 2
MIN3	*volatilizable mineral component 3
MIN4	*volatilizable mineral component 4
MIN5	*volatilizable mineral component 5

---

\*For example, CO<sub>2</sub> from carbonates or H<sub>2</sub>O from clays

Table 18. Simplified representation of the La Luna chemical reaction network. The overall initial kerogen empirical formula is  $\text{CH}_{1.26}\text{O}_{0.104}\text{S}_{0.0305}$ . Oil fraction names include an indication of boiling point range (H=heavy, M=medium, L=light, N=naphtha) and chemical type (3=alkylated aromatics and polars, 2=dealkylated aromatics and polars, 1=saturates).

1. KER1  $\rightarrow$  CHX + CH<sub>4</sub> + H<sub>2</sub>O + CO<sub>2</sub> + H<sub>2</sub>S
2. KER2  $\rightarrow$  KER4 + HO3 + MO1 + MO3 + LO1 + LO3 + CHX + CH<sub>4</sub> + CO<sub>2</sub> + H<sub>2</sub>S
3. KER4  $\rightarrow$  MO1 + MO2 + MO3 + LO1 + LO2 + LO3 + NA1 + NA2 + CHX + CH<sub>4</sub> + H<sub>2</sub> + CO<sub>2</sub> + H<sub>2</sub>S + RESC + RESH + RESO + RESS
4. HO3  $\rightarrow$  MO1 + MO2 + MO3 + LO1 + LO2 + LO3 + NA1 + NA2 + CHX + CH<sub>4</sub> + H<sub>2</sub> + CO<sub>2</sub> + H<sub>2</sub>S + RESC + RESH + RESO + RESS
5. MO3  $\rightarrow$  MO2 + LO1 + LO2 + LO3 + NA1 + NA2 + CHX + CH<sub>4</sub> + CO<sub>2</sub> + H<sub>2</sub>S + RESC + RESH + RESO + RESS
6. LO3  $\rightarrow$  LO2 + NA1 + NA2 + CHX + CH<sub>4</sub> + CO<sub>2</sub> + H<sub>2</sub>S + RESC + RESH + RESO + RESS
7. MO2  $\rightarrow$  CH<sub>4</sub> + CO<sub>2</sub> + H<sub>2</sub>S + RESC + RESH + RESO + RESS
8. LO2  $\rightarrow$  MO2 + CH<sub>4</sub> + CO<sub>2</sub> + H<sub>2</sub>S + RESC + RESH + RESO + RESS
9. NA2  $\rightarrow$  LO2 + CH<sub>4</sub> + CO<sub>2</sub> + H<sub>2</sub>S + RESC + RESH + RESO + RESS
10. MO1  $\rightarrow$  LO1 + NA1 + CHX + CH<sub>4</sub> + RESC + RESH
11. LO1  $\rightarrow$  NA1 + CHX + CH<sub>4</sub> + RESC + RESH
12. NA1  $\rightarrow$  CHX + CH<sub>4</sub> + RESC + RESH
13. CHX  $\rightarrow$  CH<sub>4</sub> + RESC + RESH
14. H<sub>2</sub>  $\rightarrow$  RESH
15. RESC + RESH  $\rightarrow$  H<sub>2</sub> + CH<sub>4</sub>
16. KER8  $\rightarrow$  HO1
17. KER9  $\rightarrow$  NA3
18. HO1  $\rightarrow$  CHX + RESC + RESH
19. HO2  $\rightarrow$  CHX + RESC + RESH

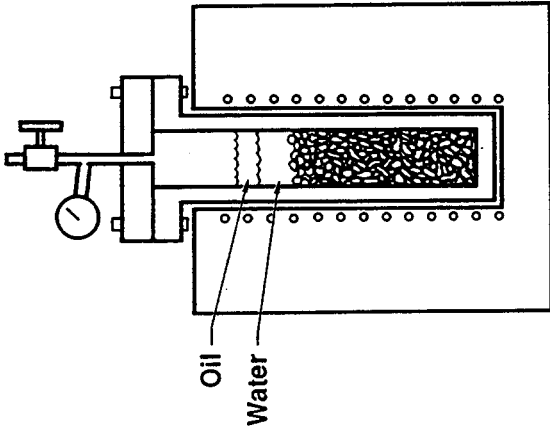
Table 19. Variations for parameter sensitivity study

Name	Description	Lower value	Base value	Upper value
TOC	Organic carbon, wt%	1.5	3.8	9.6
HR	Heating rate, °C/m.y.	2.0	4.0	8.0
EPSC	Compaction coefficient, Pa <sup>-1</sup>	3.43·10 <sup>-8</sup>	6.86·10 <sup>-8</sup>	1.03·10 <sup>-7</sup>
KPRES	Hydraulic conductivity coefficient	1.0·10 <sup>-22</sup>	1.0·10 <sup>-20</sup>	1.0·10 <sup>-18</sup>
FLITH	Pore/lithostatic pressure for fracturing	0.8	0.9	1.0
PER2	Water saturation above which relative permeability of organic fluid is zero	0.6	0.8	1.0
	Water saturation below which relative permeability of organic fluid is one	0.2	0.4	0.6

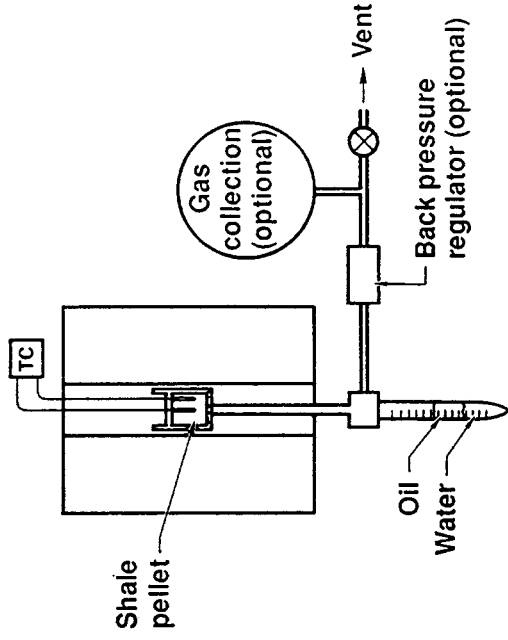
Table 20. Comparison of calculated and measured Rock Eval parameters for well Alturitas 19X.

	<u>Measured</u>	<u>Leaky system</u>	<u>Closed system</u>
TOC:	1.5%-1.9%	2.2%	3.73%
HI:	156-220 mg/g TOC	307	259
T <sub>max</sub> :	437-447°C	443°C	443°C
S1:	1.46-2.91 mg/g	2.5	12.5
S2:	2.65-6.95 mg/g	6.75	9.69
PI:	0.2 - 0.49	0.27	0.56

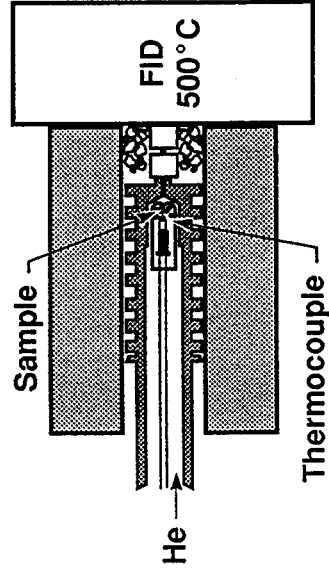
## 1. Hydrous pyrolysis



## 2. Autogenous, self-purging



## 3. Programmed micropyrolysis at multiple heating rates



## 4. Pyrolysis-TQMS

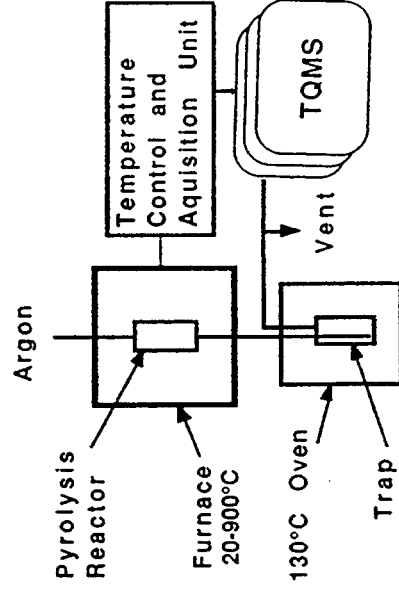


Figure 1. Schematic diagram of the four pyrolysis systems used for oil and gas generation kinetics. Hydrous pyrolysis was done at INTEVEP and the other three at LLNL.

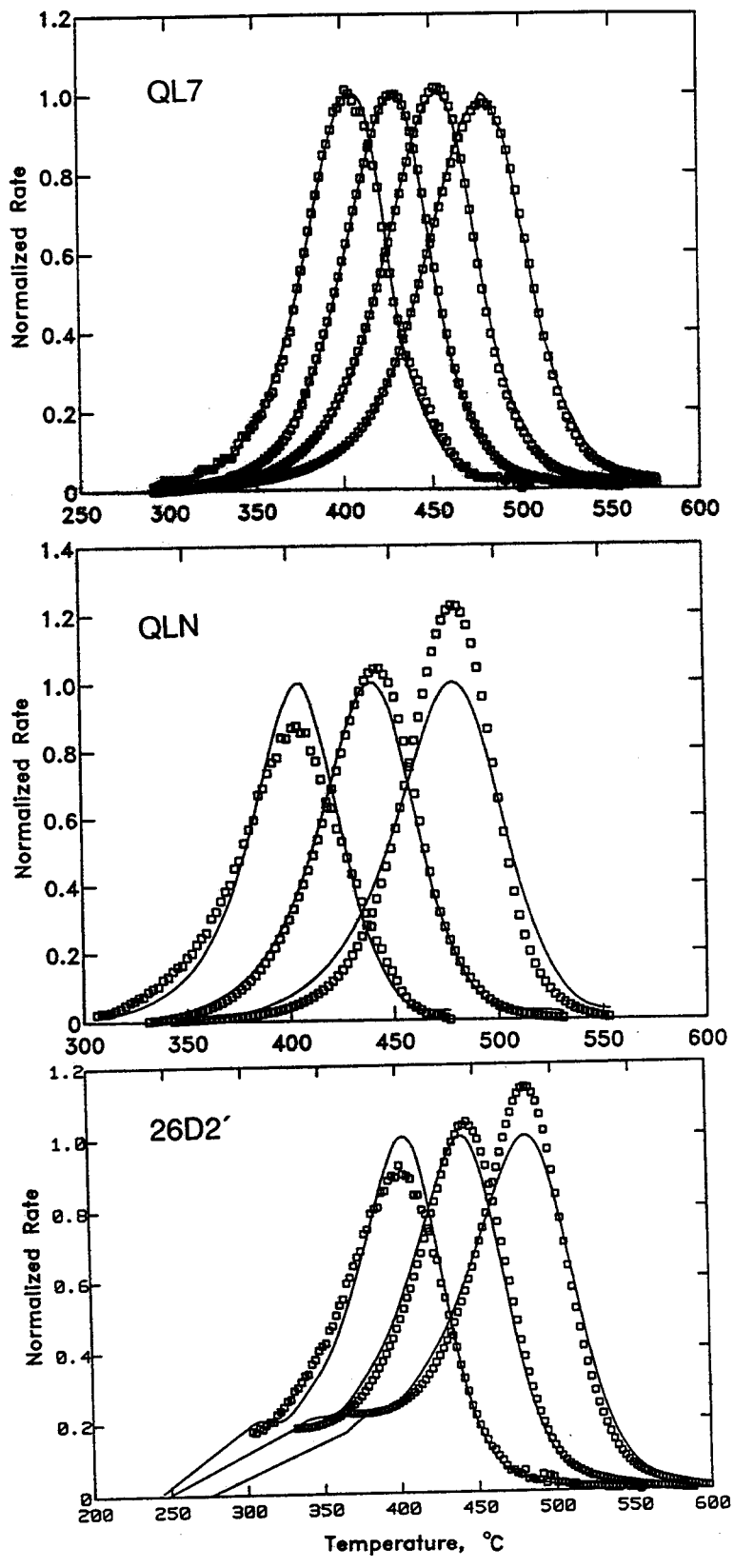


Figure 2. Comparison of measured and calculated Pyromat reaction rates for samples QL7, QLN, and 26D2'. The heating rates were 1, 4, 15, and 50 °C/min for sample QL7 and 1, 7, and 50 °C/min for the other two samples.

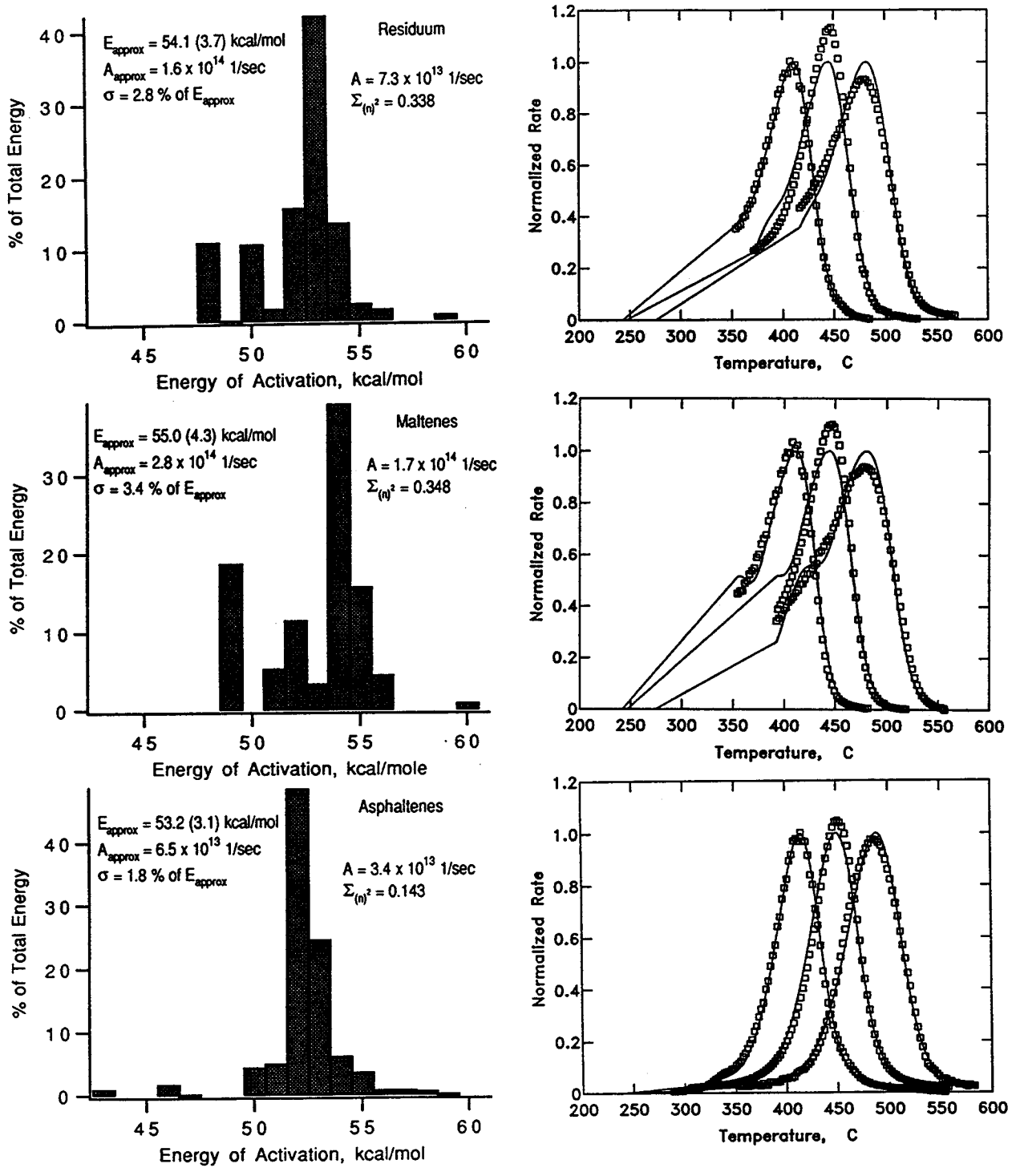


Figure 3. Kinetic measurements and parameters for Boscan 1000°F residuum (top), maltenes (middle) and asphaltenes (bottom). The low temperature contributions from the whole residuum and maltenes have been cut out for the kinetic analysis.

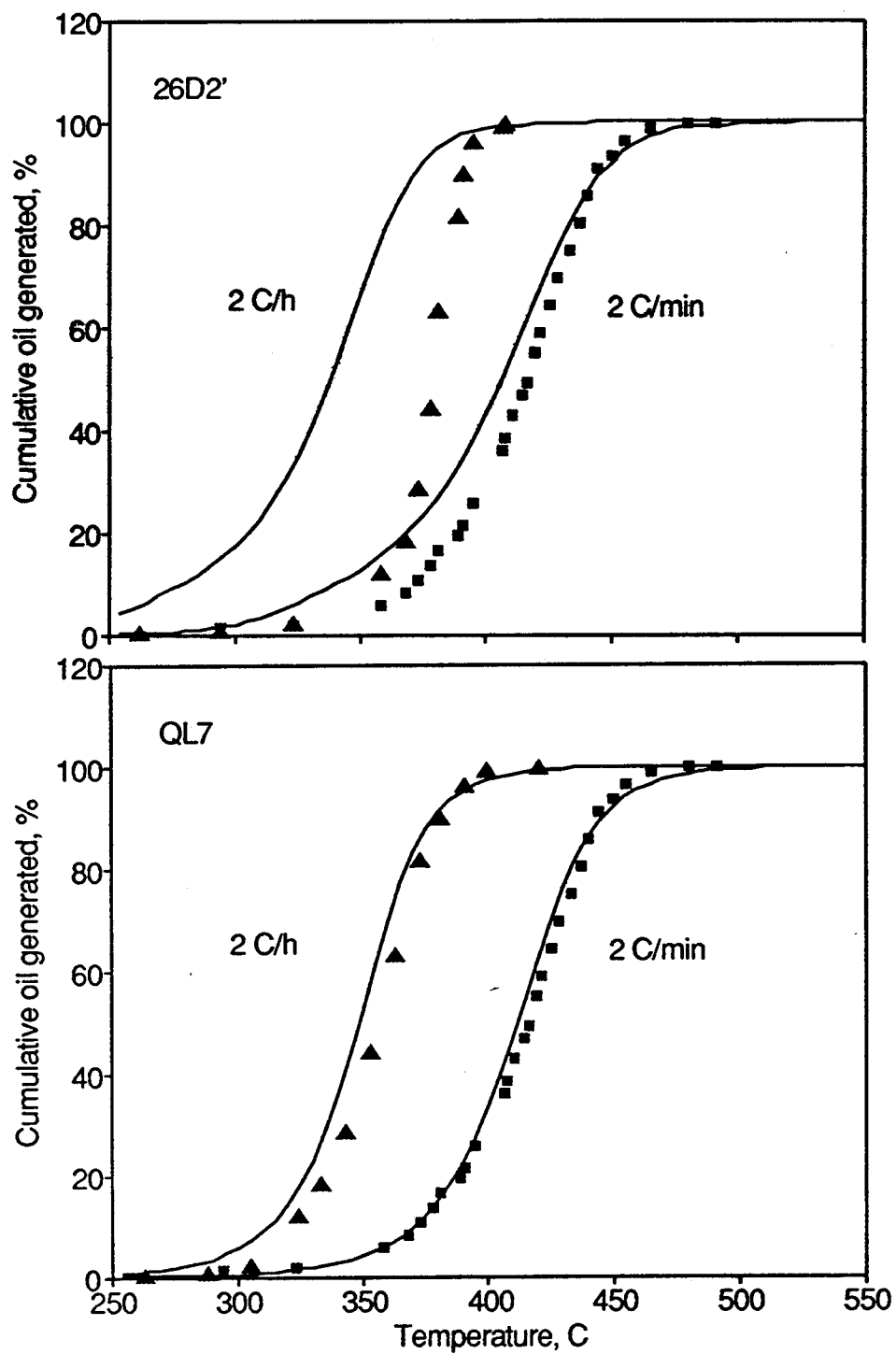


Figure 4. Measured and calculated conversion versus temperature for oil evolution from samples QL7 and 26D2' heated in a self-purging reactor.

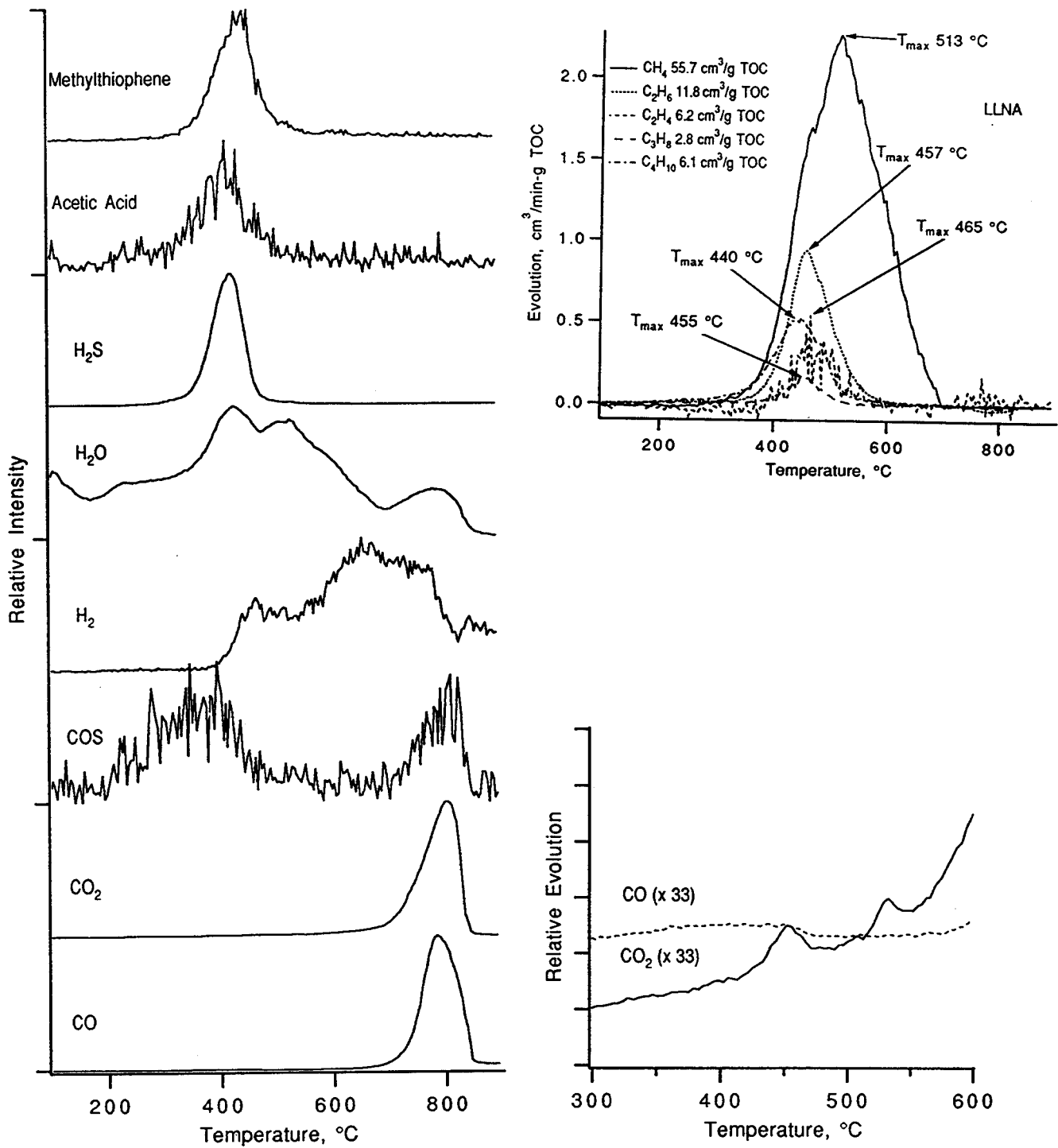


Figure 5. Evolution profiles for 13 gaseous species generated from sample QL7 at 10 °C/min.

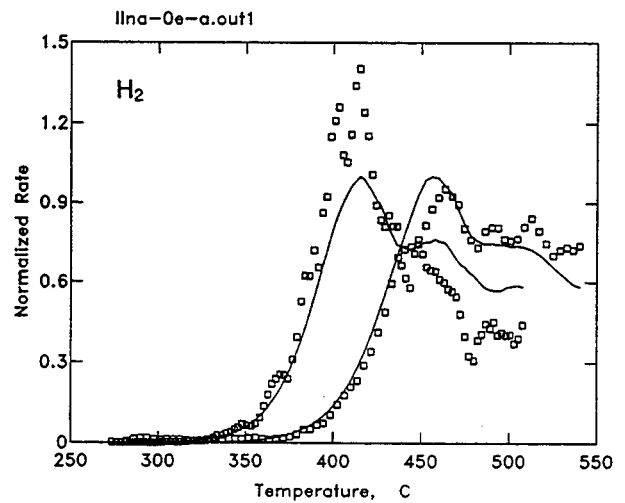
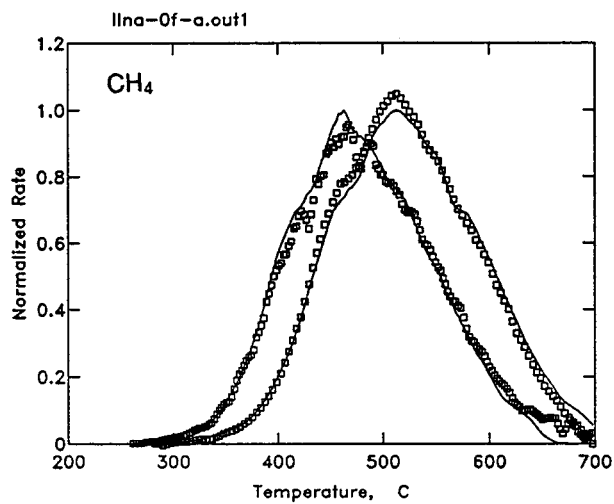
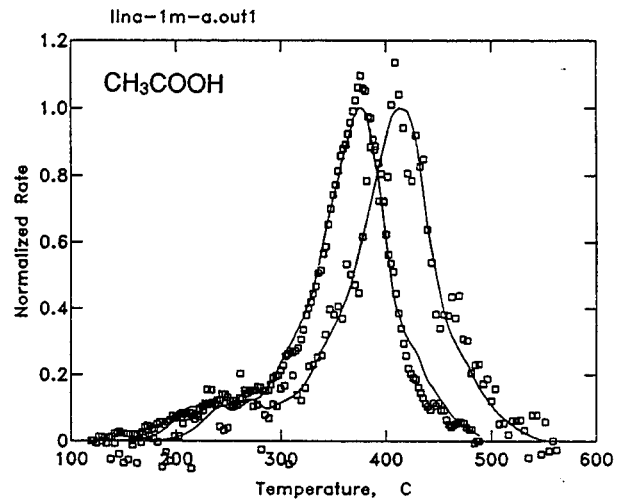
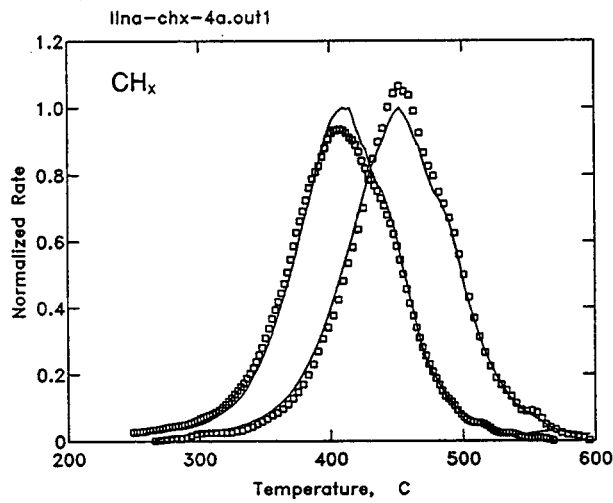
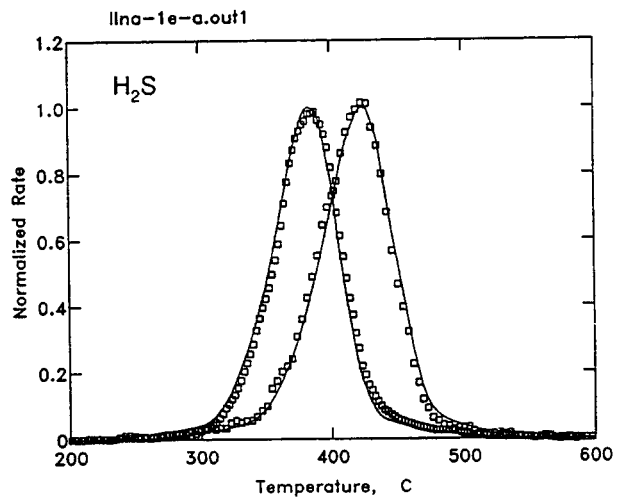
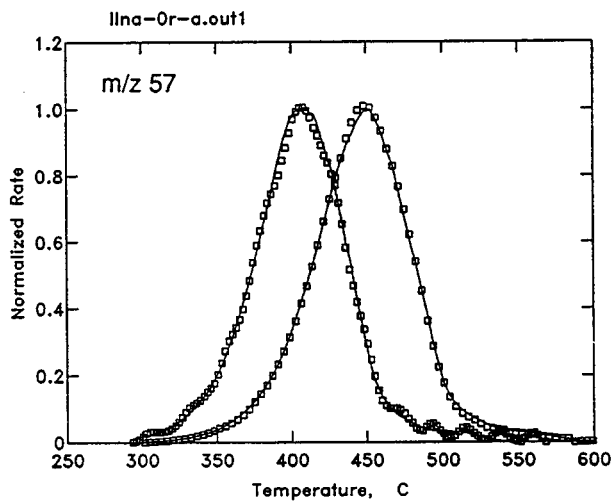


Figure 6. Measured and calculated evolution profiles from sample QL7 heated at 1 and 10 °C/min: CH<sub>4</sub>, C<sub>2</sub>-C<sub>4</sub> (CH<sub>x</sub>), H<sub>2</sub>S, H<sub>2</sub>, acetic acid, and m/z = 57 amu.

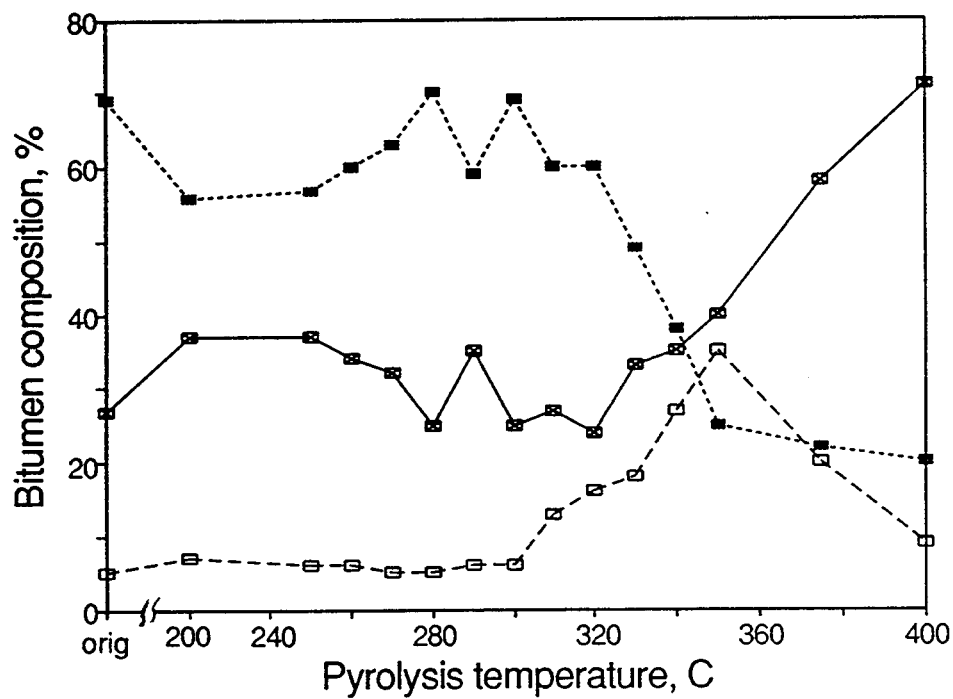
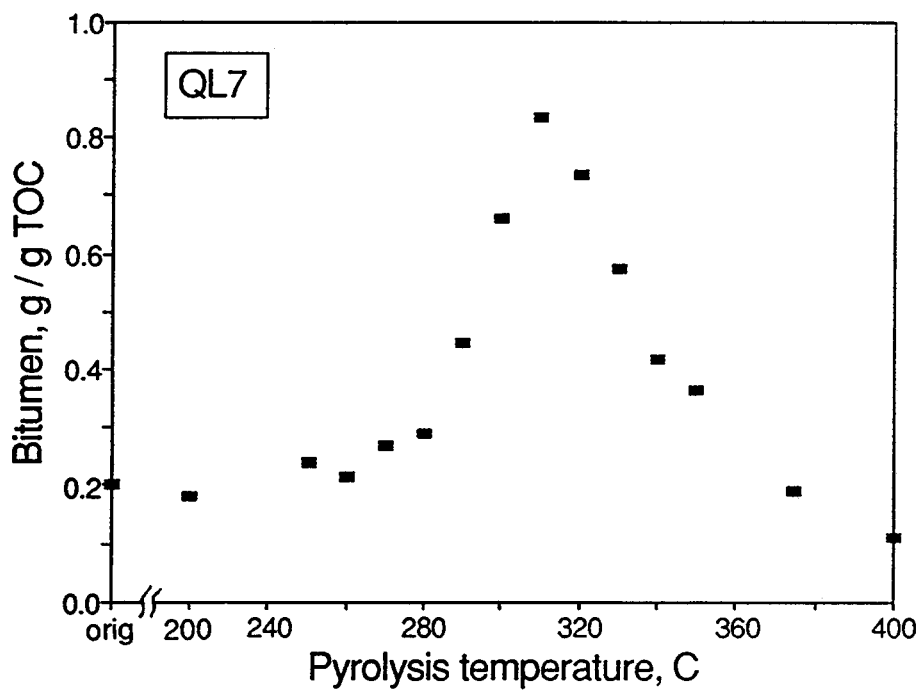


Figure 7. Total bitumen yields (top) and compositions (bottom) from sample QL7 heated for 72 h at the indicated temperature. Polars—solid rectangles; aromatics—rectangles with x; saturates—open rectangles.

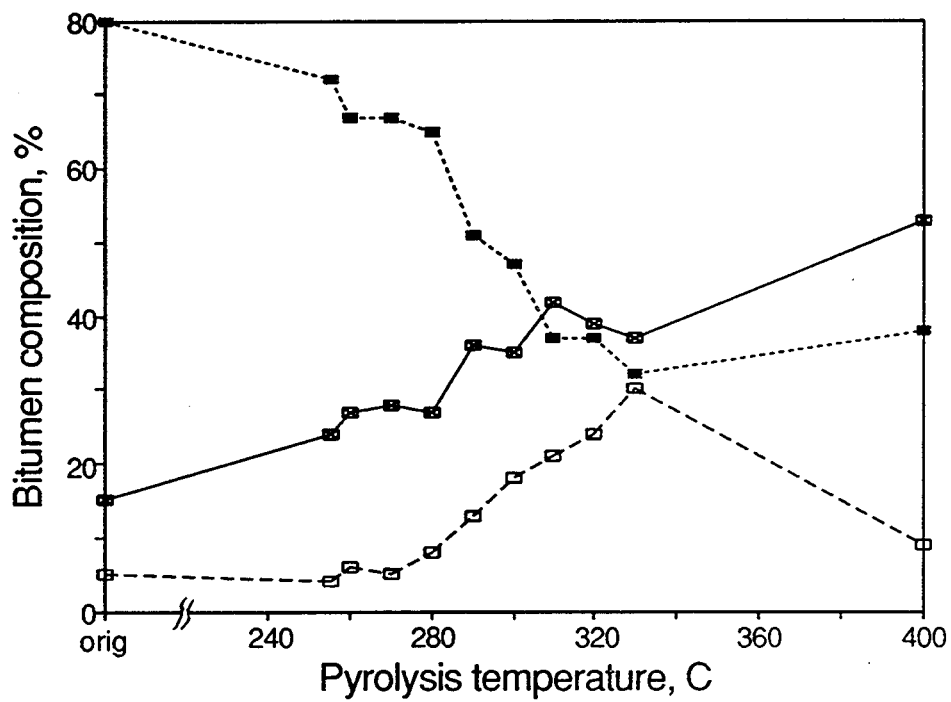
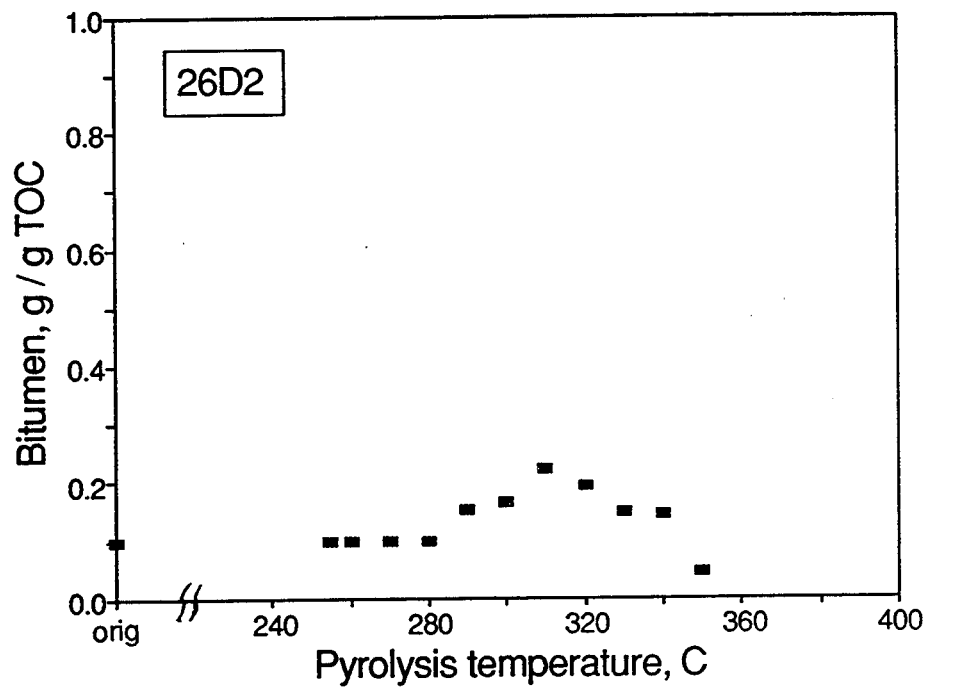


Figure 8. Total bitumen yields (top) and compositions (bottom) from sample 26D2 heated for 72 h at the indicated temperature. Same symbol code as in Figure 7.

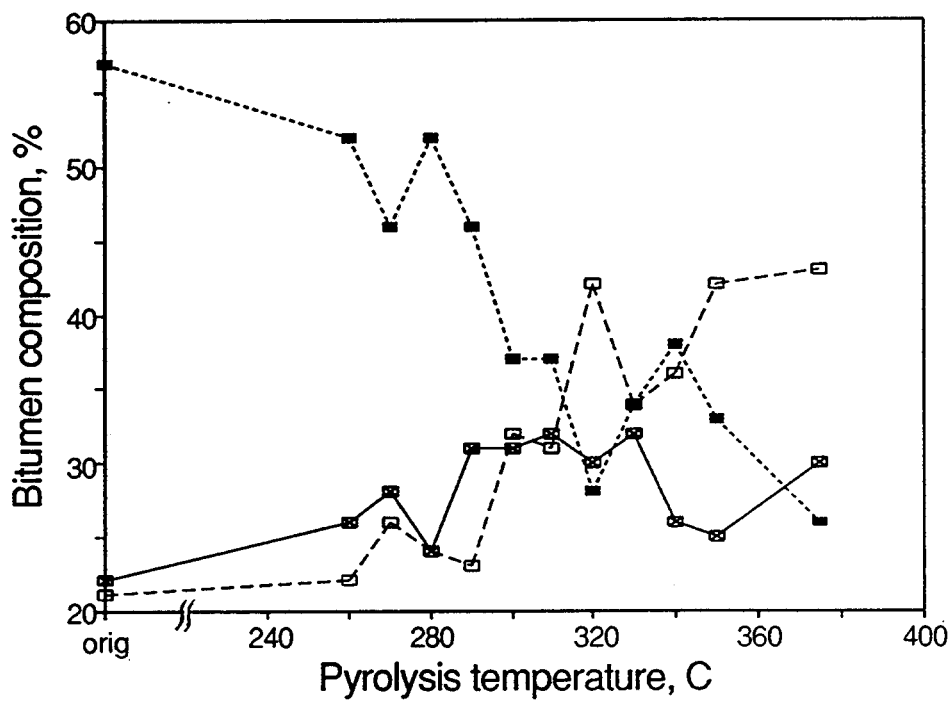
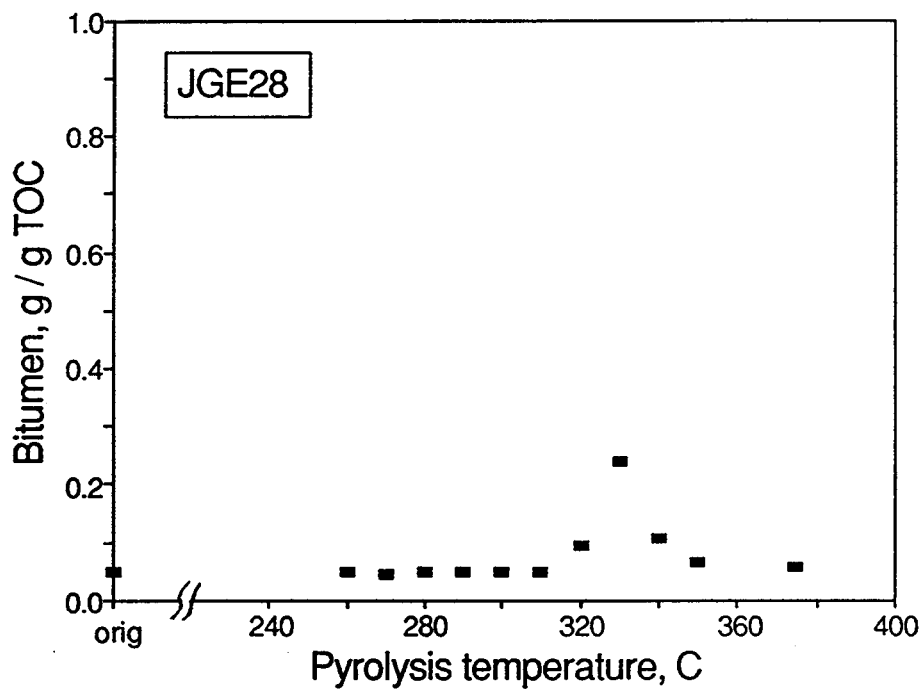


Figure 9. Total bitumen yields (top) and compositions (bottom) from sample JGE28 heated for 72 h at the indicated temperature. Same symbol code as in Figure 7.

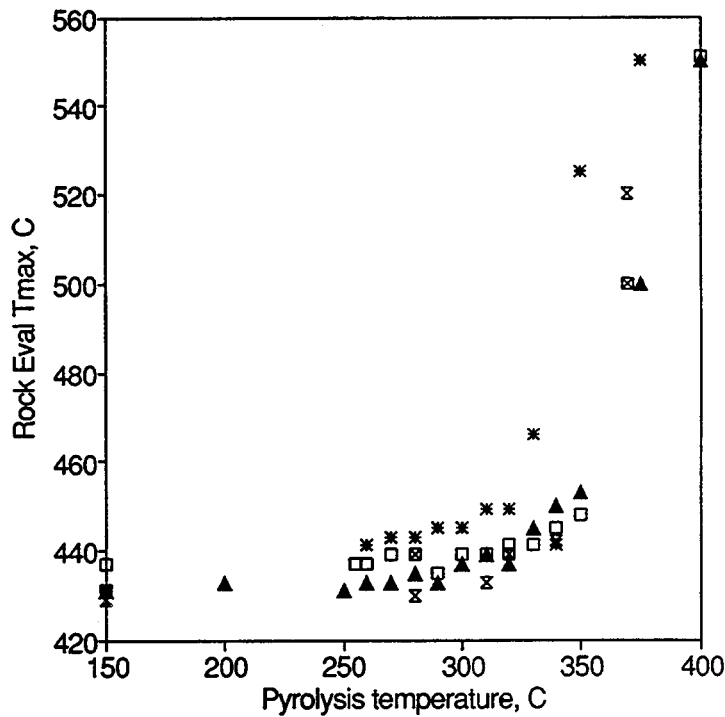


Figure 10. Dependence of Rock-Eval  $T_{max}$  on pyrolysis temperature for 72-h heating for all 5 samples investigated. QL7–filled triangles; 26D2–open squares; 26D2'–squares with x; QLN–hourglass ; JGE28–asterisks.

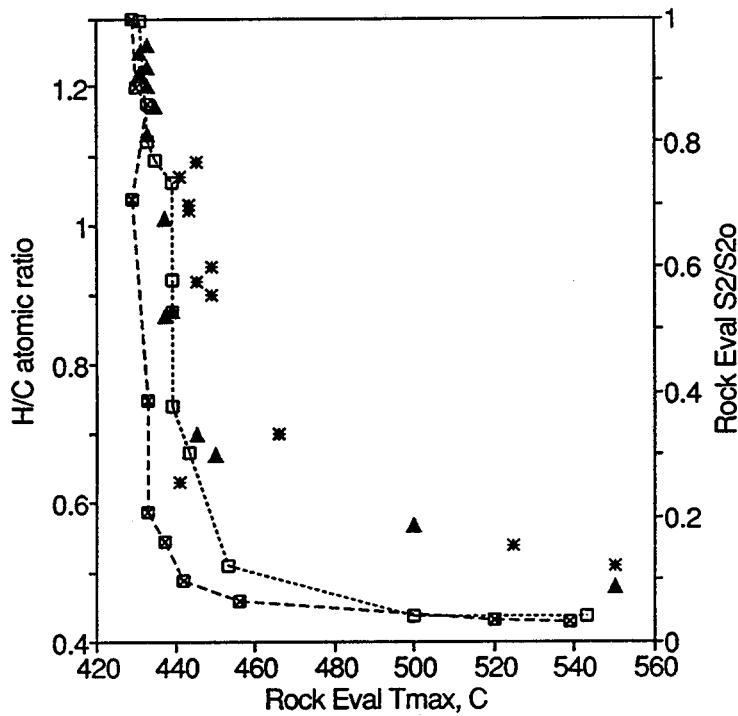


Figure 11. Dependence of residual kerogen H/C ratio and remaining Rock Eval pyrolysis potential on  $T_{max}$ . QL7 H/C–filled triangles; JGE28 H/C–asterisks; 26D2' S2–open squares; QLN S2–squares with x

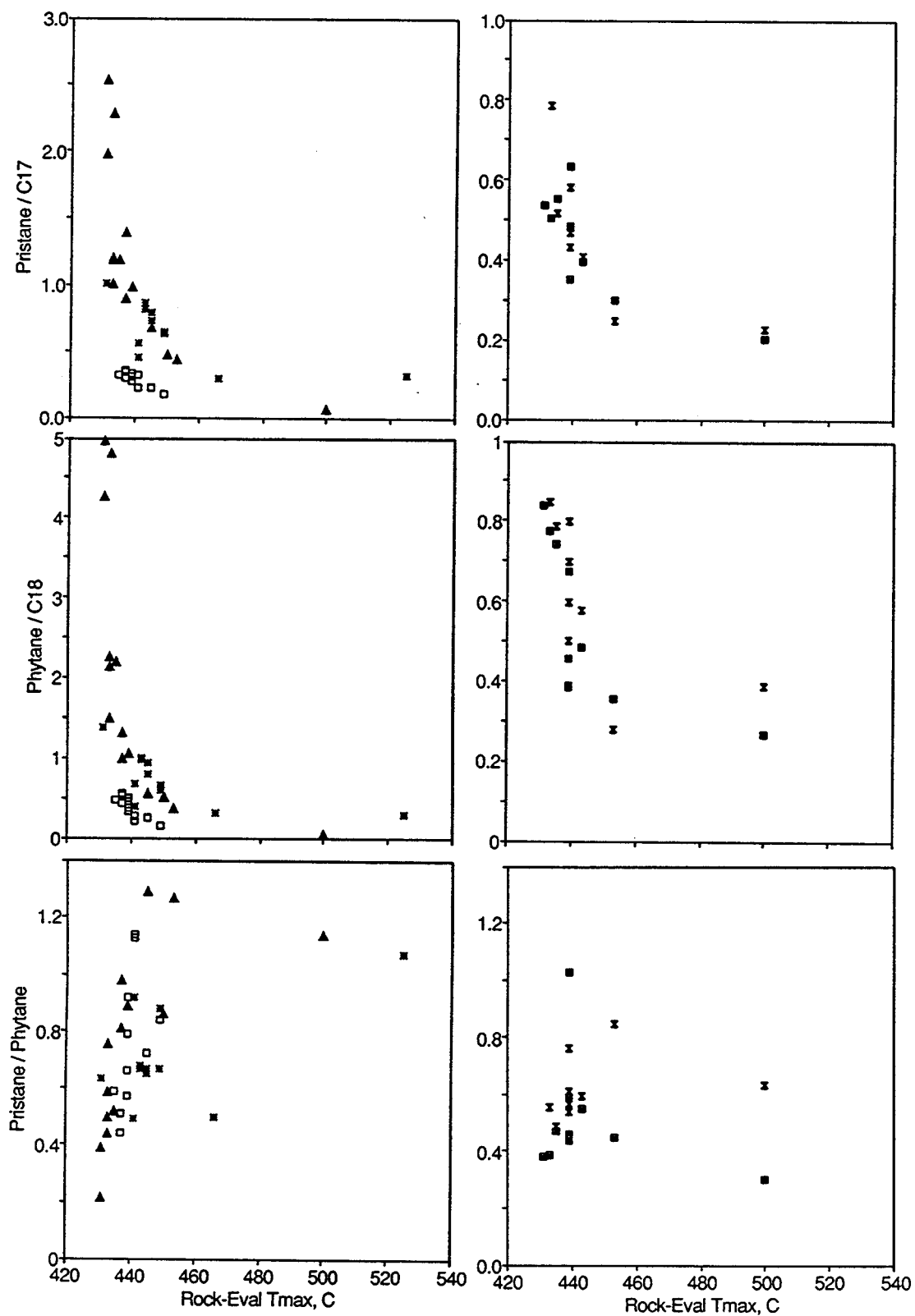


Figure 12. Relationship between three biomarker ratios and  $T_{max}$ . The left-hand figures show the data for total bitumen: QL7–filled triangles; 26D2–open squares; JGE28–asterisks. The right-hand figures show data for the HPC-series expulsion experiments on sample 26D2': expelled oil–hourglasses; extracted bitumen–squares with x.

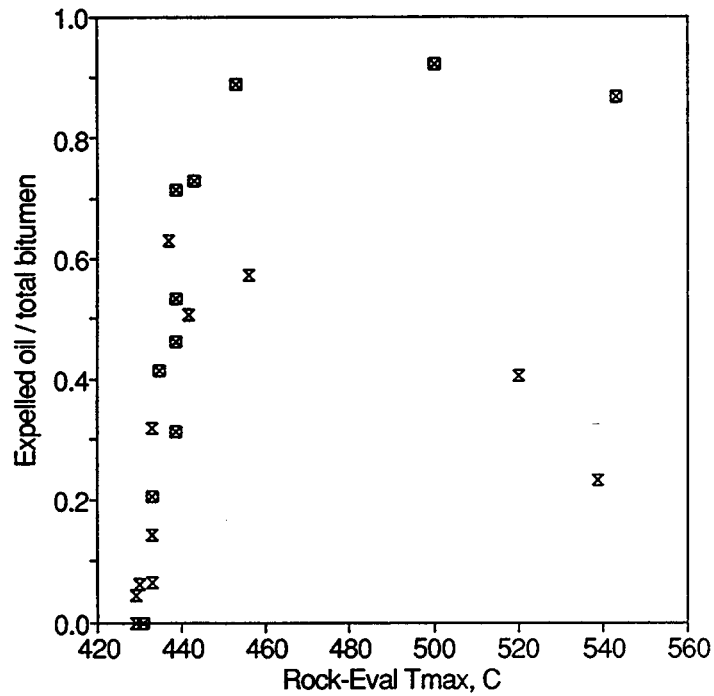


Figure 13. Relationship between  $T_{max}$  and the ratio of expelled oil to total bitumen (expelled oil plus extracted bitumen) for samples QLN (square with x) and 26D2' (hourglass).

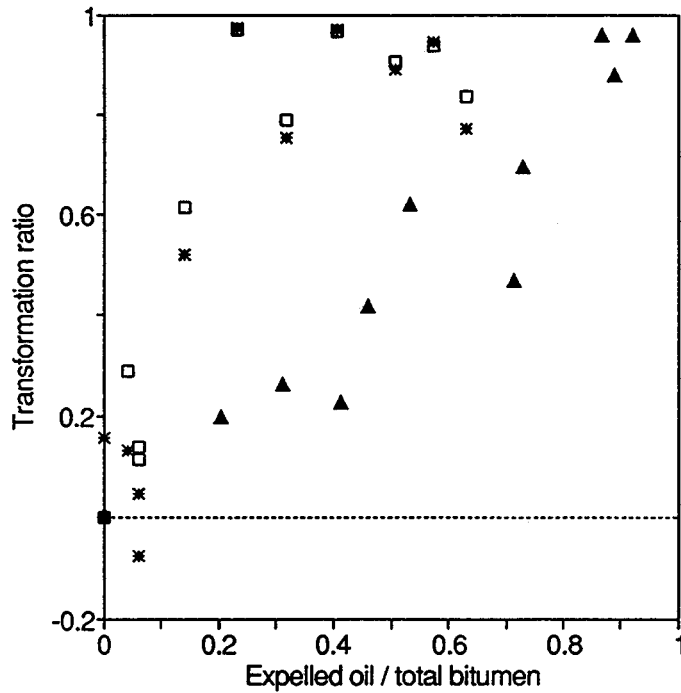


Figure 14. Relationship between the ratio of expelled oil to total bitumen and the transformation ratio calculated from Rock-Eval pyrolysis yield. QLN—squares and asterisks; 26D2'—triangles.

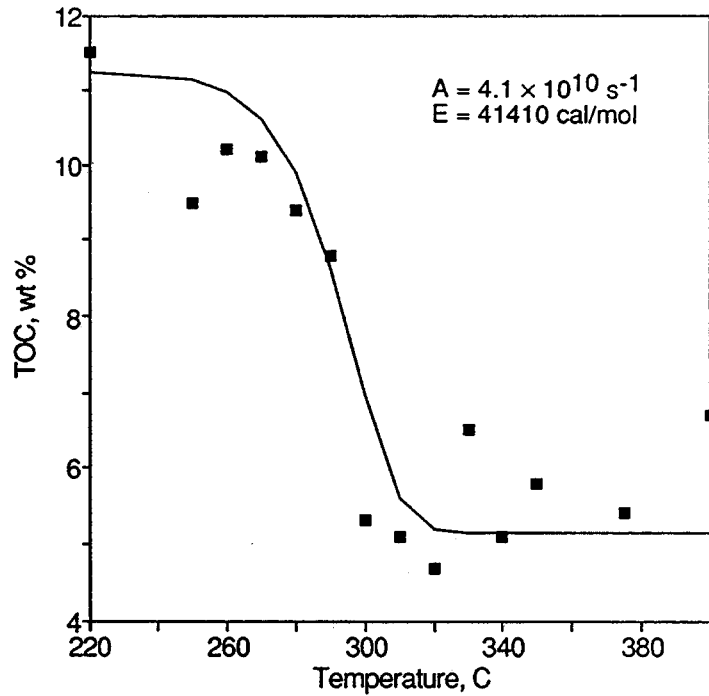


Figure 15. Measured and calculated residual TOC content for sample QL7 heated for 72 h at various temperatures. The calculated values represent a non-linear regression fit to the data using Eq. (4).

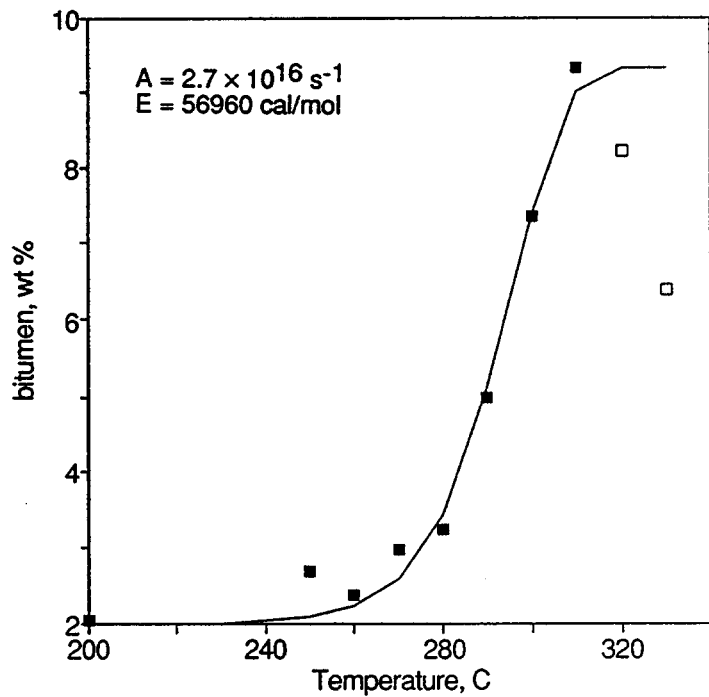


Figure 16. Measured and calculated bitumen content for sample QL7 heated for 72 h at various temperatures. The calculated values represent a nonlinear regression analysis assuming an initial bitumen content of 2 wt%. The open squares represent data not included in the fit where secondary cracking reactions have become important.

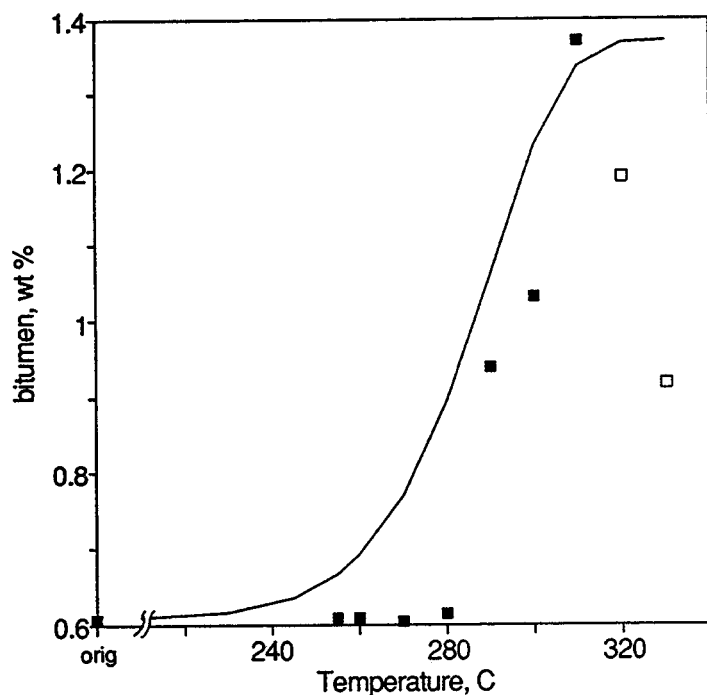


Figure 17. Bitumen yields from sample 26D2' compared to values calculated from QL7 kinetics from Figure 16, assuming a higher native bitumen content.

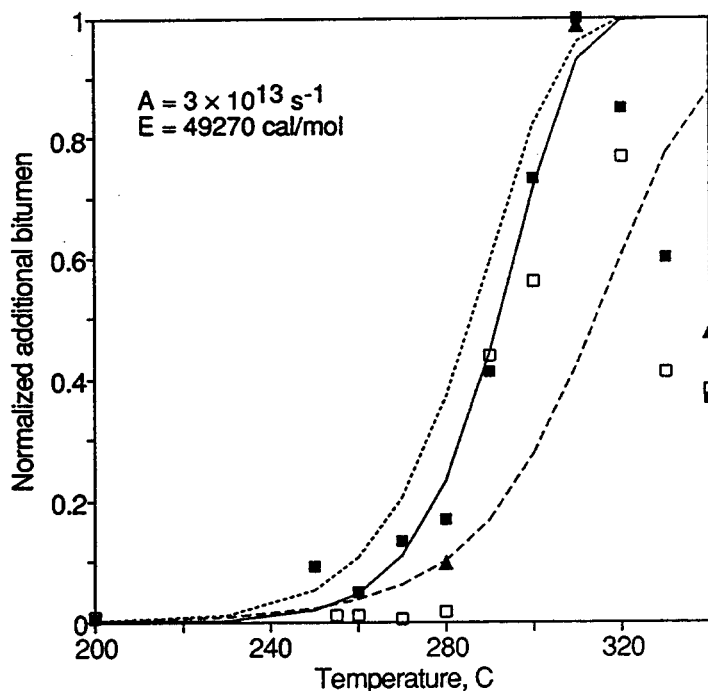


Figure 18. Comparison of measured additional bitumen yields from samples QL7, 26D2', and QLN with three kinetic expressions. The kinetics derived from disappearance of TOC (short dash) lead the appearance of bitumen slightly, and the oil evolution kinetics derived from the self-purging reactor (long dash) lag the bitumen generation considerably. The adjusted bitumen generation kinetics (solid line, assuming  $A = 3 \times 10^{13} \text{ s}^{-1}$ , giving  $E = 49.3 \text{ kcal/mol}$ ) agree well with all three samples. QL7—filled squares; 26D2—open squares; QLN—triangles. The 26D2 point at 310°C and 1.0 is not visible.

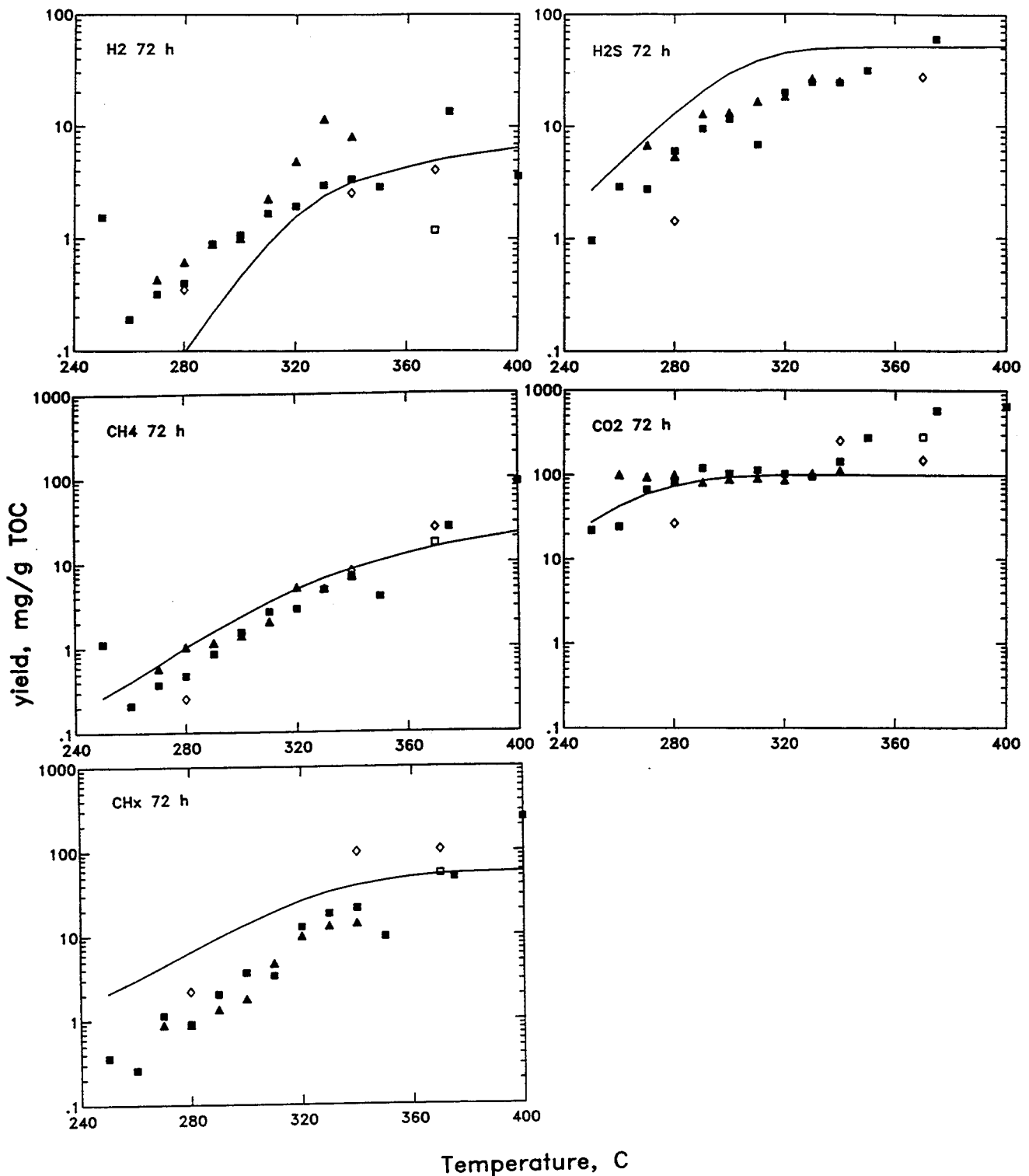


Figure 19. Comparison of measured (points) and calculated (curves) gas generation for hydrous pyrolysis for 72 h at the indicated temperature. For CH<sub>4</sub>, C<sub>2</sub>-C<sub>4</sub> (CH<sub>x</sub>), H<sub>2</sub>S, H<sub>2</sub>, both the yields and rate constants are derived from the pyrolysis-TQMS experiments. The curve for CO<sub>2</sub> is calculated from a simple kinetic model designed to fit the hydrous pyrolysis data. QL7-solid squares; JGE28-solid triangles; 26D2'-open squares; QLN-diamonds.

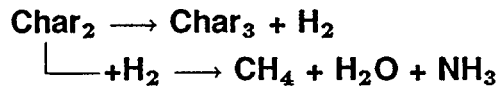
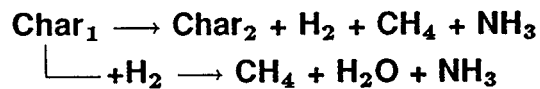
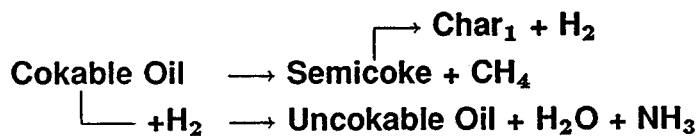
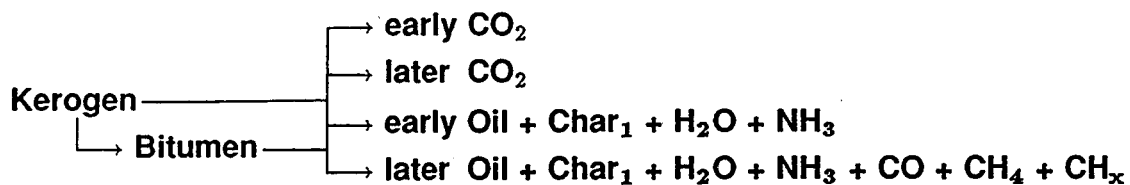


Figure 20. Chemical reactions in PYROL.

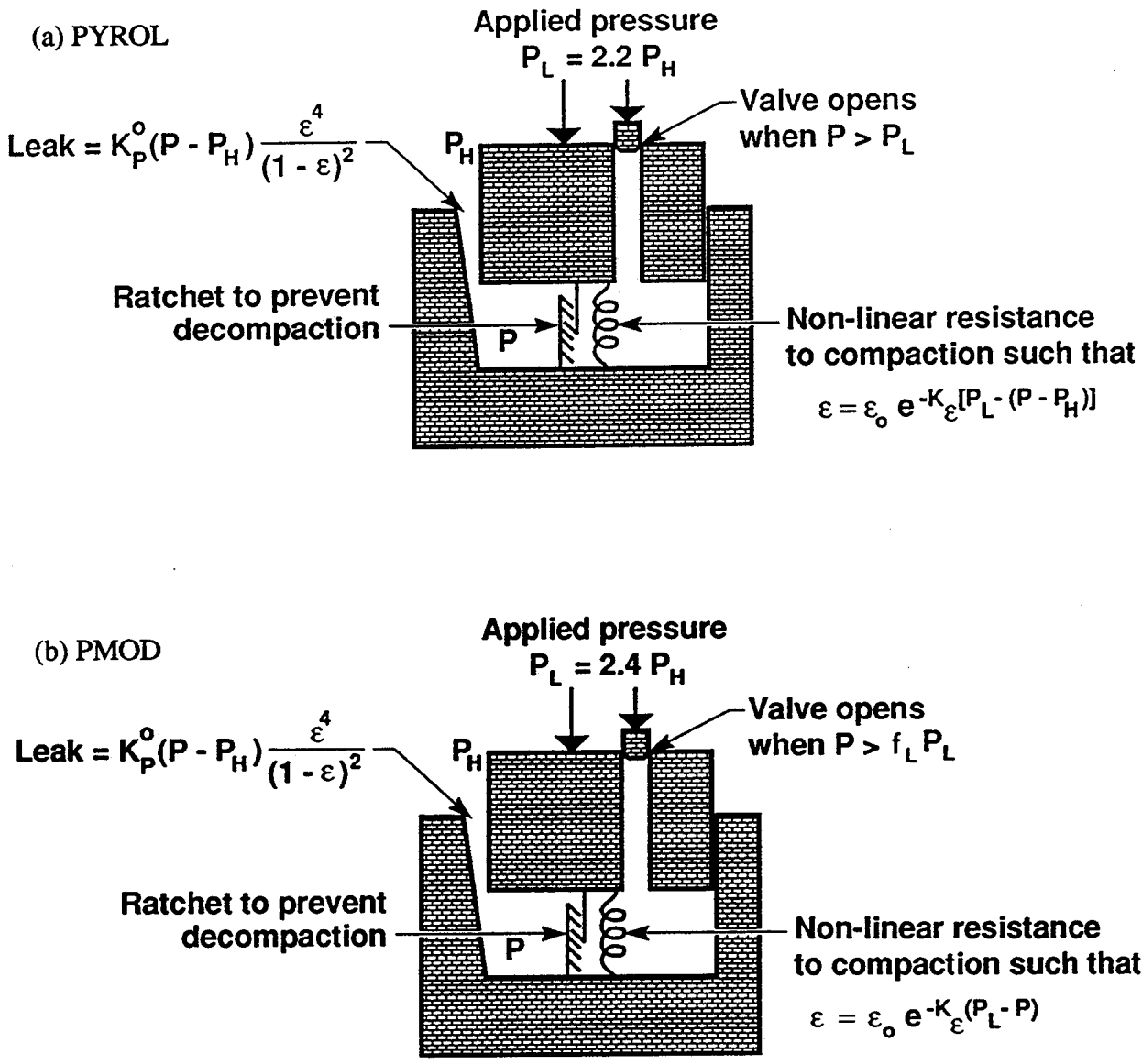


Figure 21. Schematic representation of the compacting leaky reactor models for petroleum expulsion in PYROL and PMOD. Both assume that pore fluid escape is driven by excess pore pressure and governed by a global conductivity that depends on porosity. One difference is that effective stress is related to overburden pressure minus excess pore pressure in PYROL and the overburden minus the total pore pressure in PMOD. This difference disappears if  $P_L$  in the PYROL model is assumed to be a buoyantly corrected overburden pressure ( $\approx 1.4 P_H$ ). Details of the ratchet implementation make the models different in other respects. PYROL allows no porosity increase while PMOD allows porosity increase due to solid disappearance as long as the pore pressure is large enough to support the additional porosity. PMOD also includes an adjustable fracture parameter for the valve opening, typically 0.85.

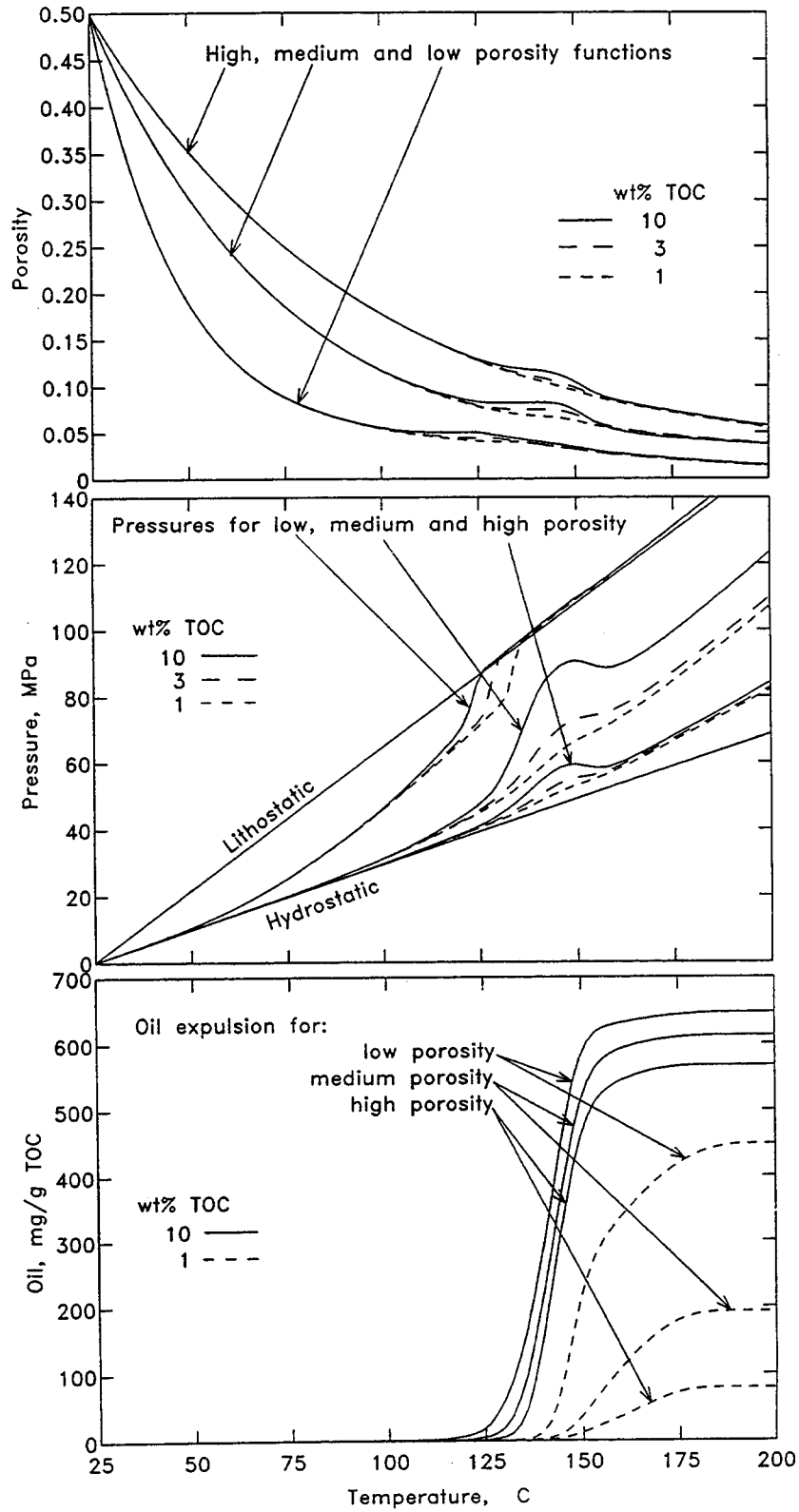


Figure 22. Dependence of overpressure generation and oil expulsion efficiency on the equilibrium porosity function as calculated by PYROL for a geological heating rate of 3 °C/m.y. (Type I kerogen).

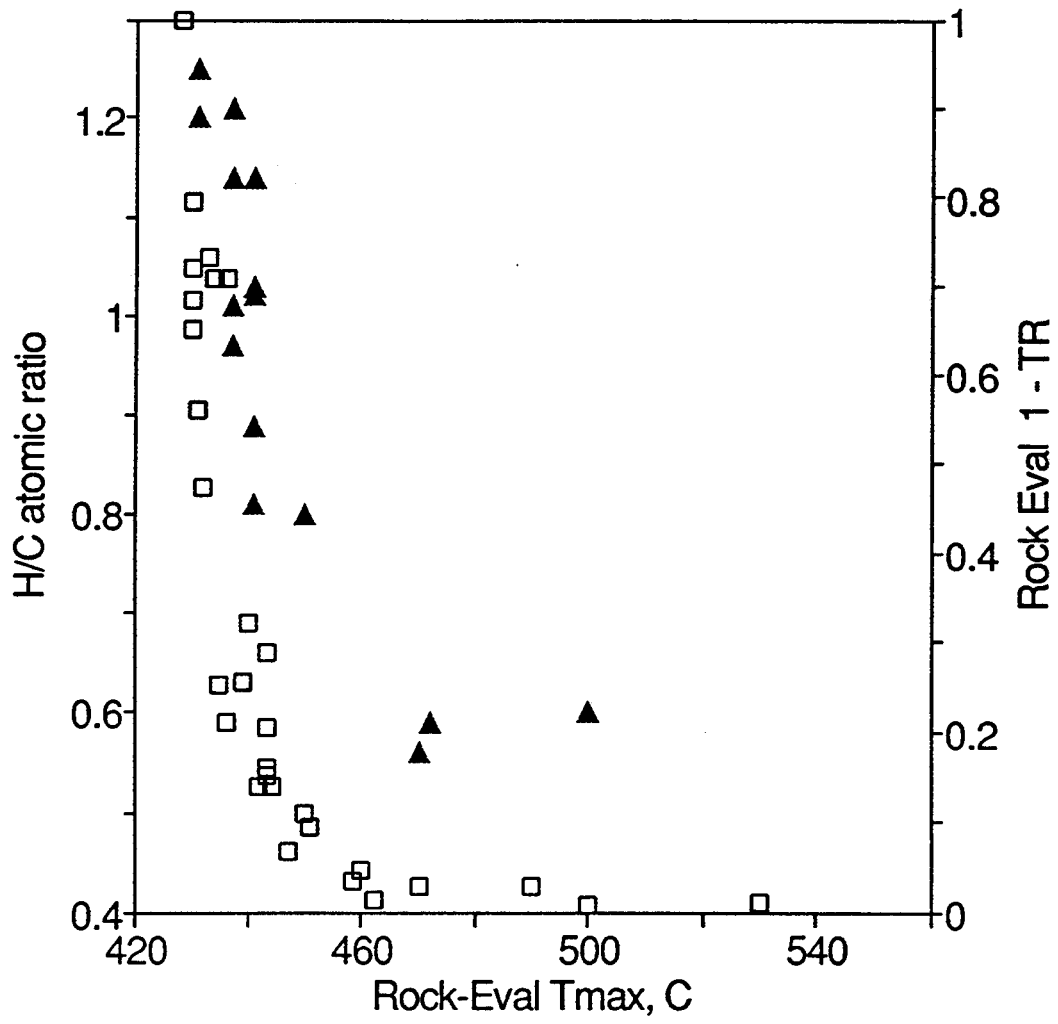


Figure 23. Dependence of kerogen residual H/C ratio (triangles) and Rock-Eval transformation ratio (squares) on Rock-Eval  $T_{max}$  for geological samples from the Maracaibo Basin.

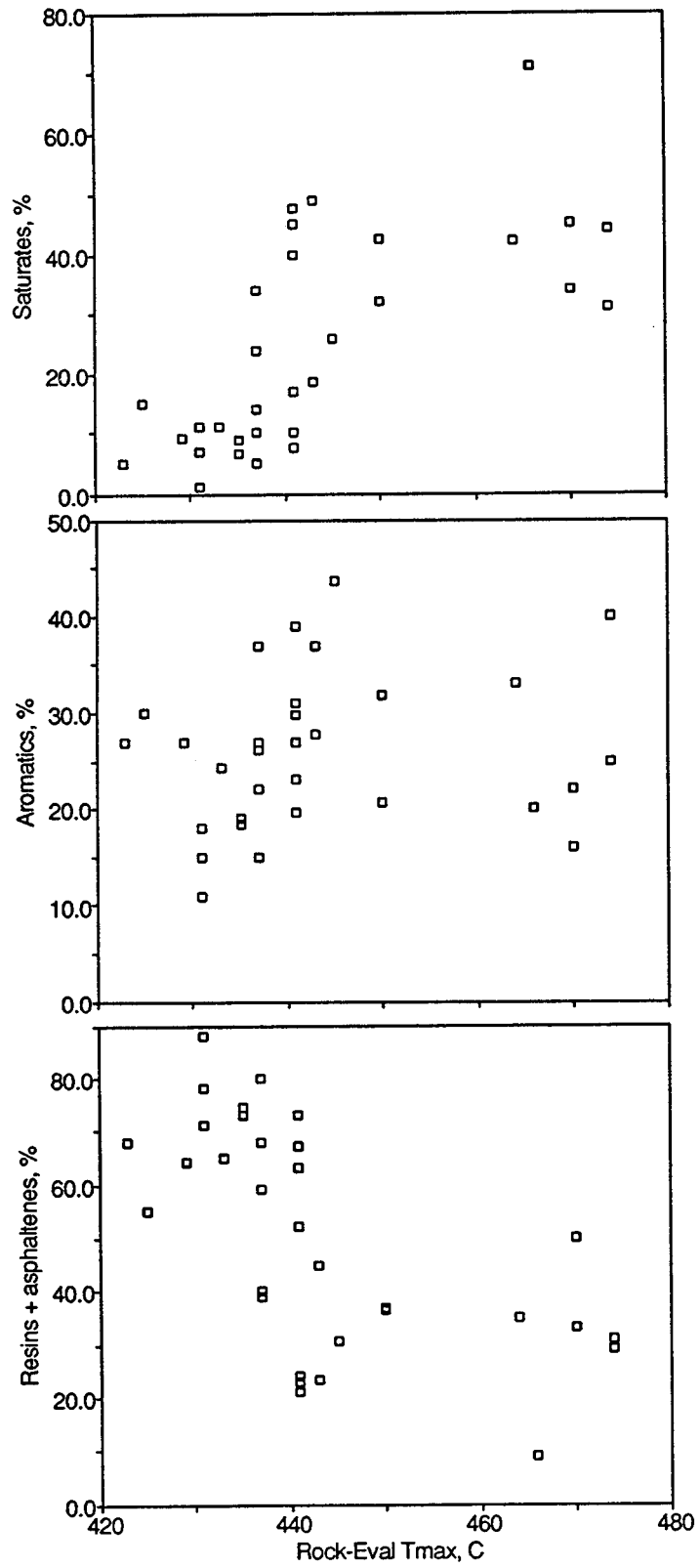


Figure 24. Dependence of extract composition on Rock-Eval  $T_{max}$  for geological samples from the Maracaibo Basin.

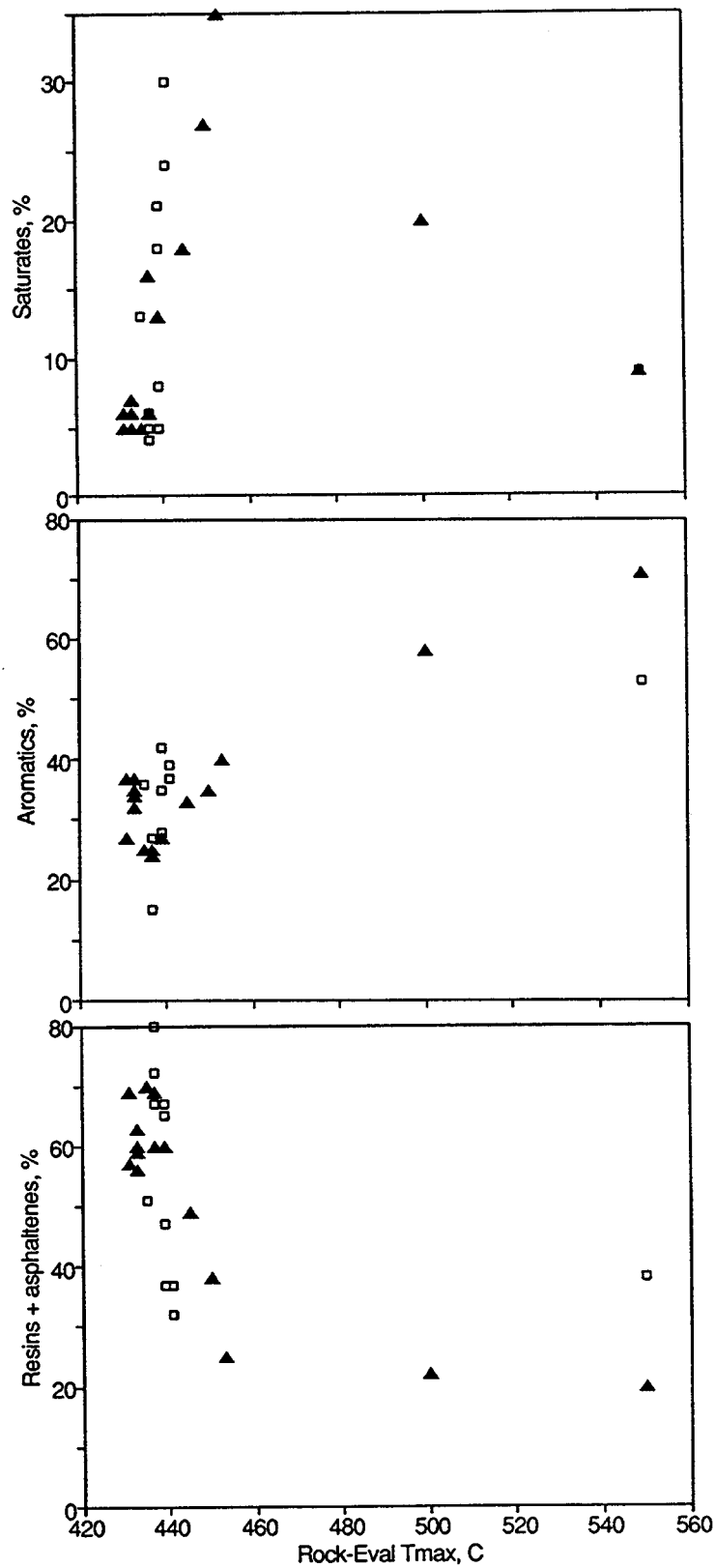


Figure 25. Dependence of total bitumen composition on Rock-Eval  $T_{max}$  for hydrous pyrolysis experiments on samples QL7 (triangles) and 26D2 (squares).

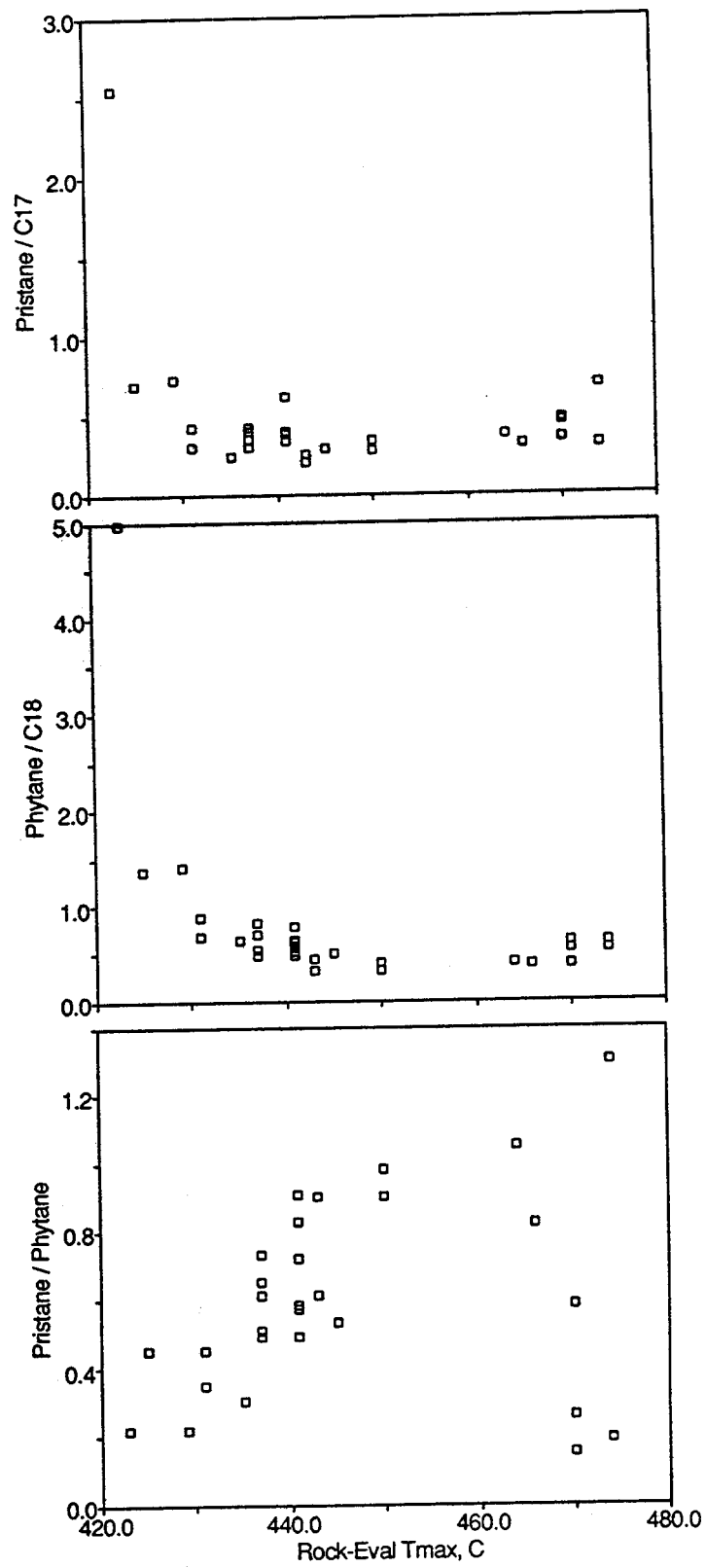


Figure 26. Dependence of three biomarker ratios on Rock-Eval  $T_{max}$  for source rock extracts from the Maracaibo Basin.

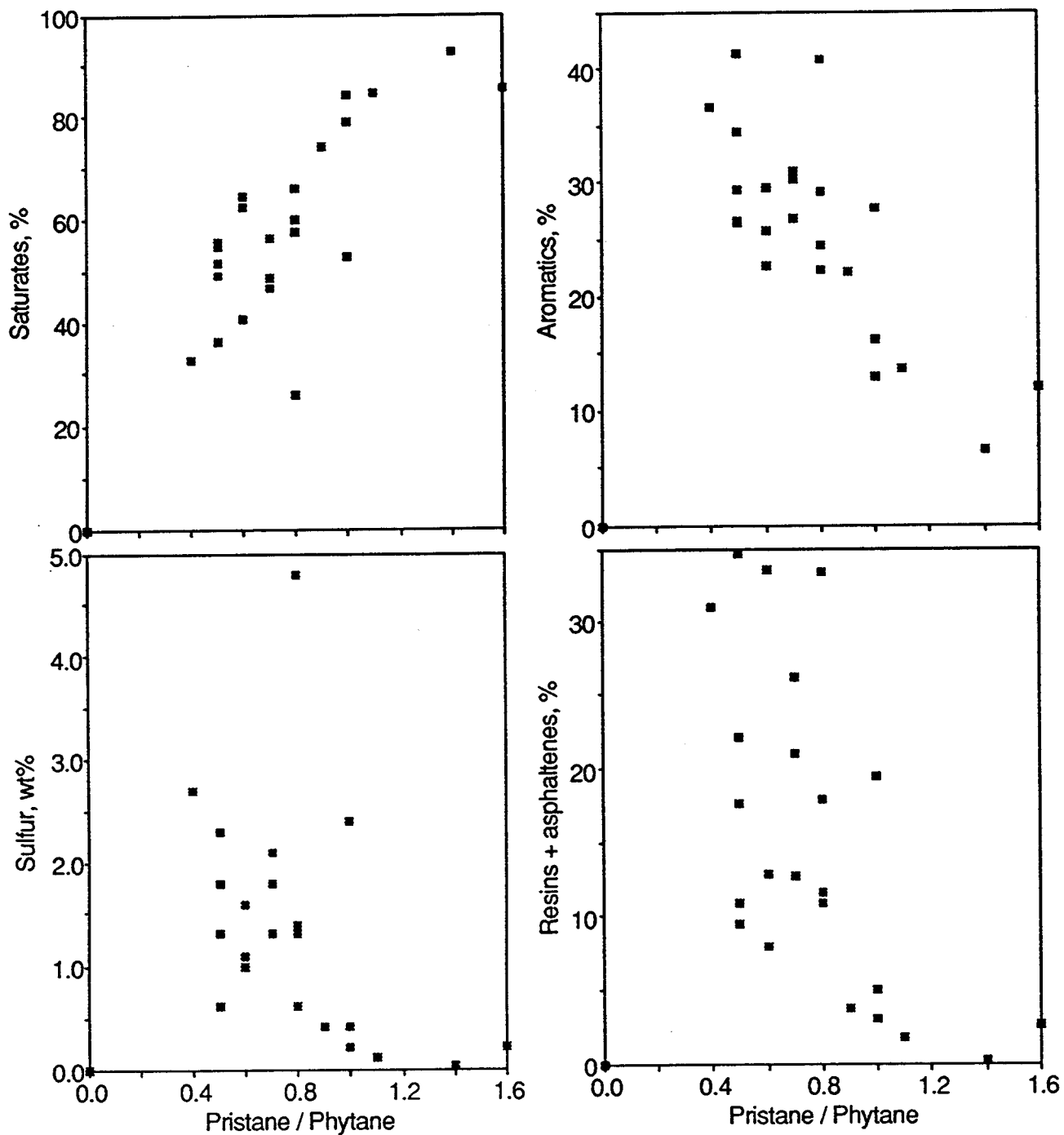


Figure 27. Relationship between the pristane/phytane ratio Maracaibo oils found in cretaceous reservoirs and global oil composition parameters.

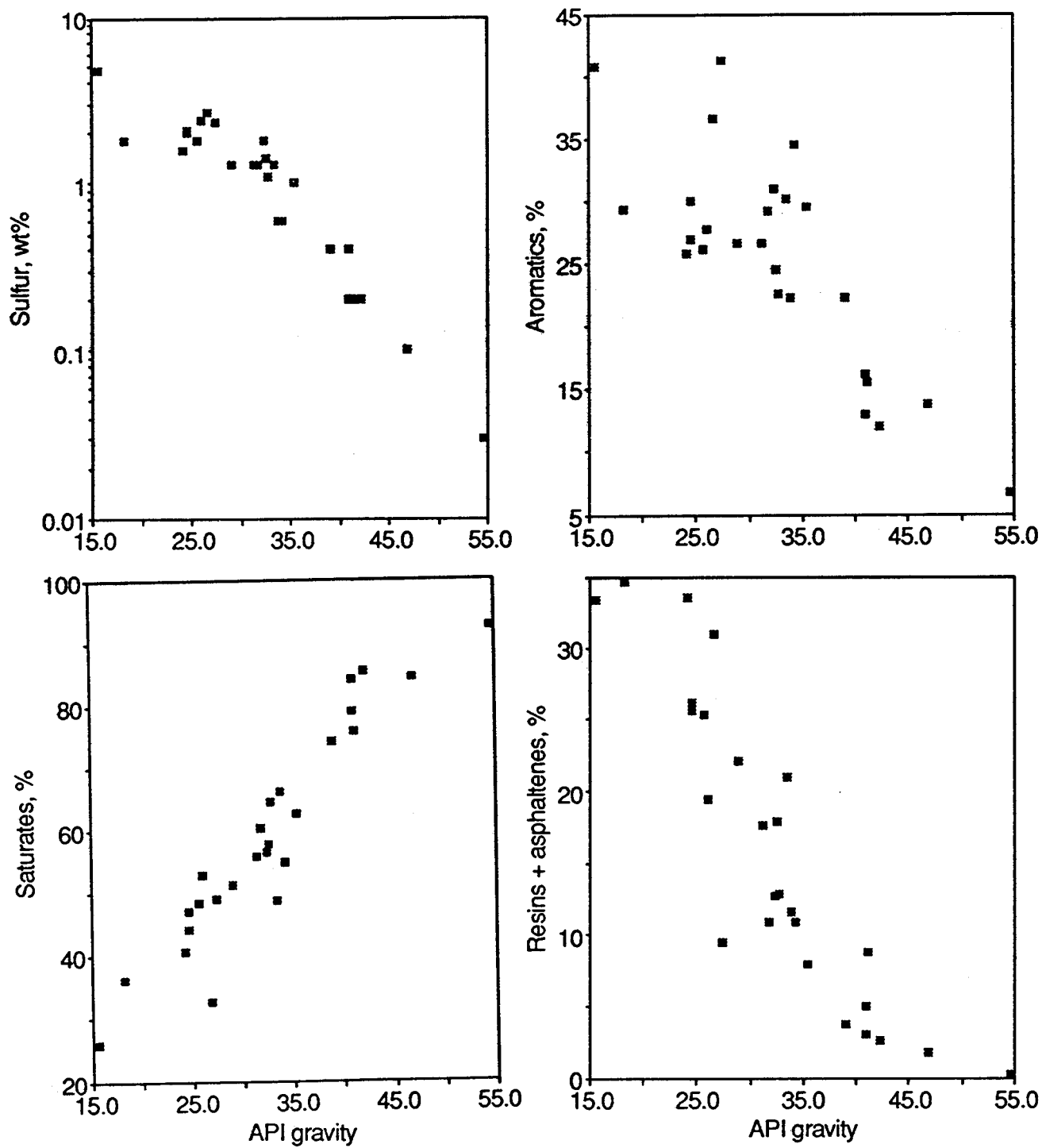


Figure 28. Relationship between API gravity and other composition indicators for the same oils shown in Figure 27.

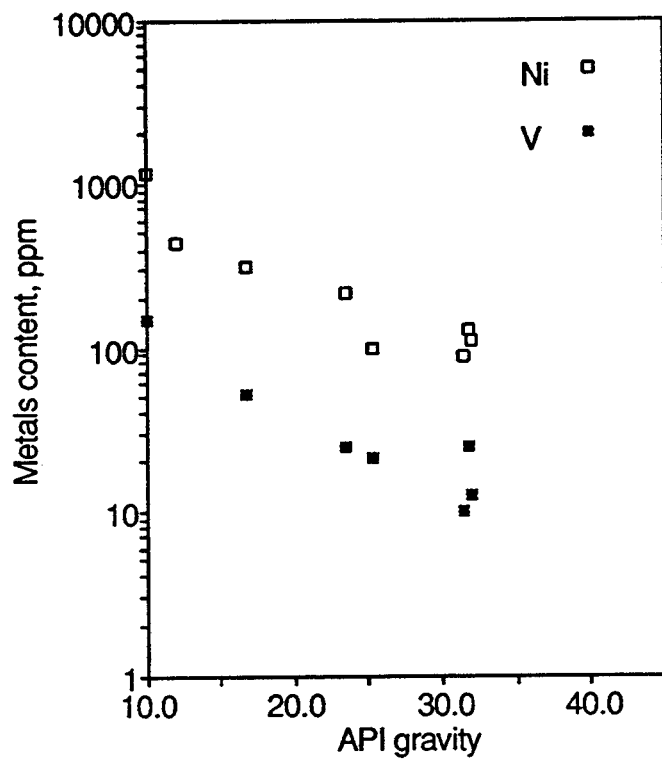


Figure 29. Nickel and vanadium content of whole Maracaibo Basin oils versus API gravity. The metal concentrations were calculated by multiplying the metal content of the atmospheric residuum times the residuum fraction of the whole oil.

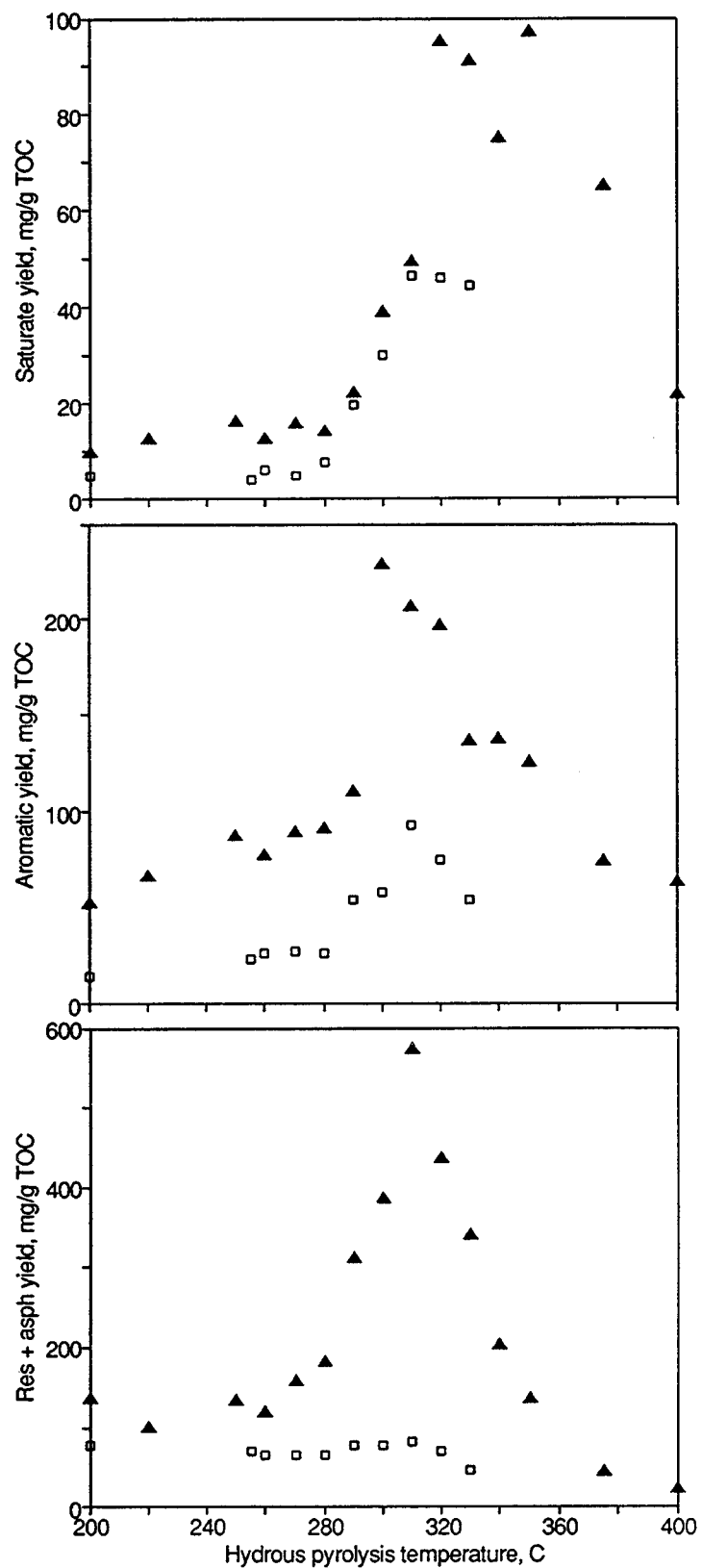


Figure 30. Absolute yields of chemical types for hydrous pyrolysis for 72 h at the indicated temperature: QL7-triangles; 26D2-squares.

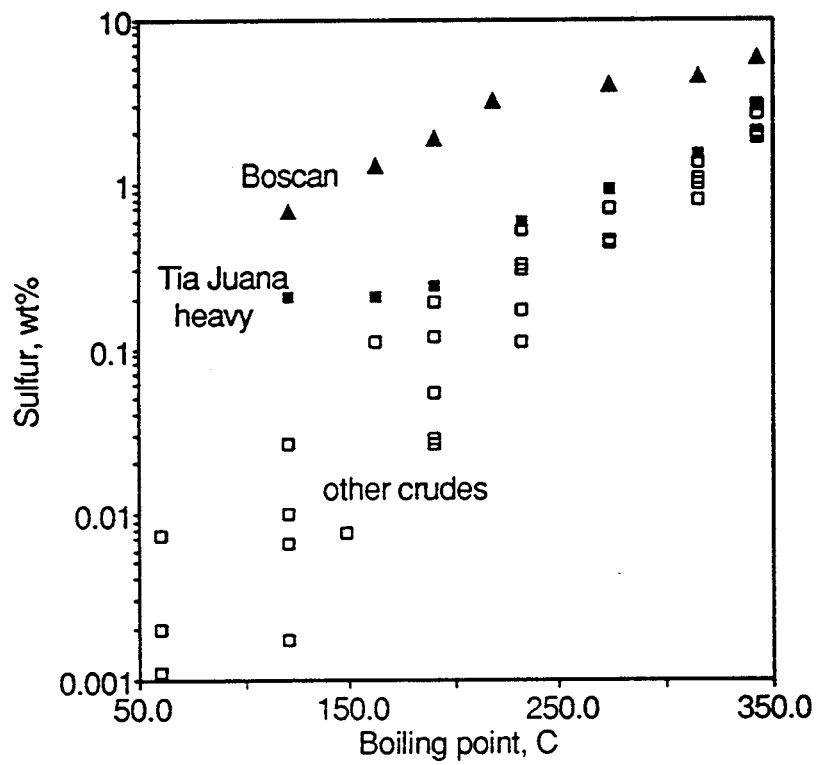


Figure 31. Sulfur content of various boiling-point fractions of 6 Maracaibo Basin oils.

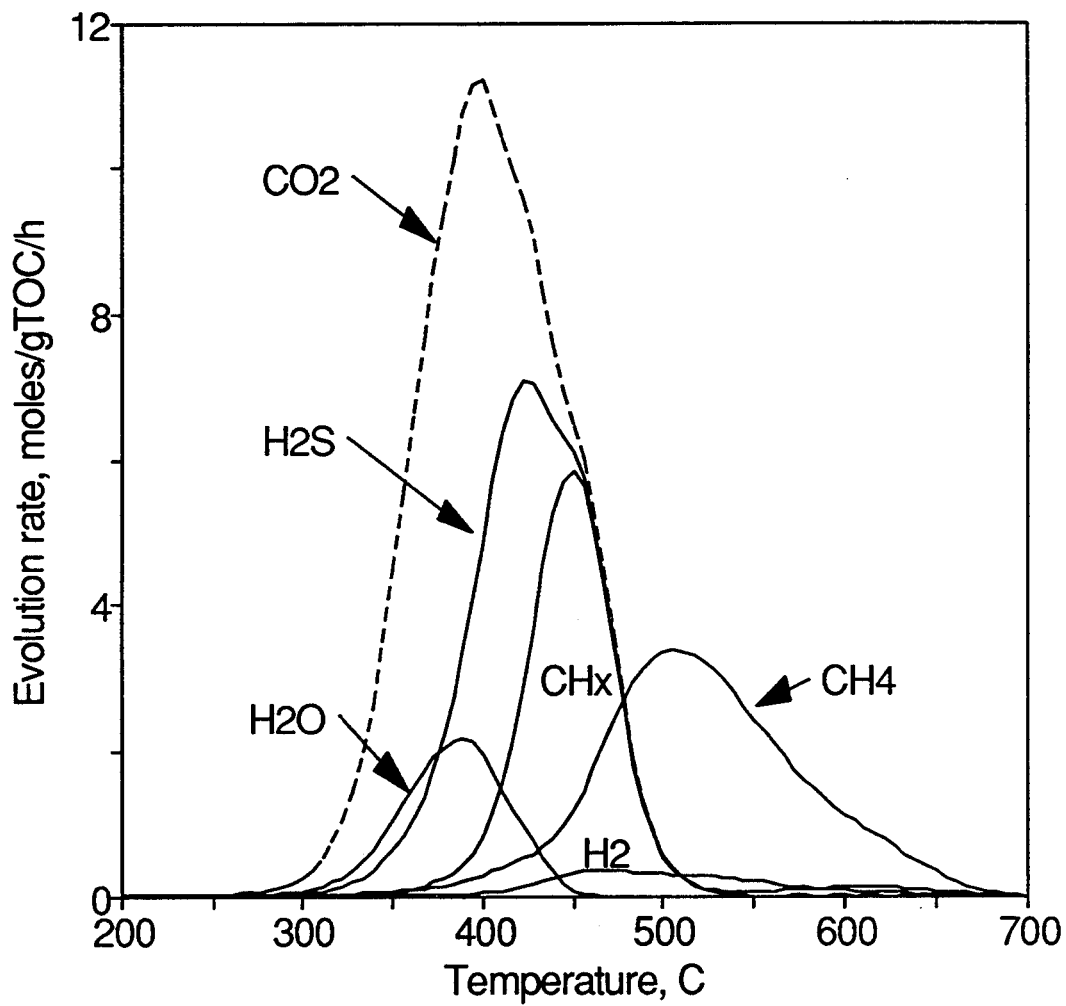


Figure 32. Calculated gas evolution profiles for a heating rate of 10 °C/min, using the PMOD mechanism in Table 18.

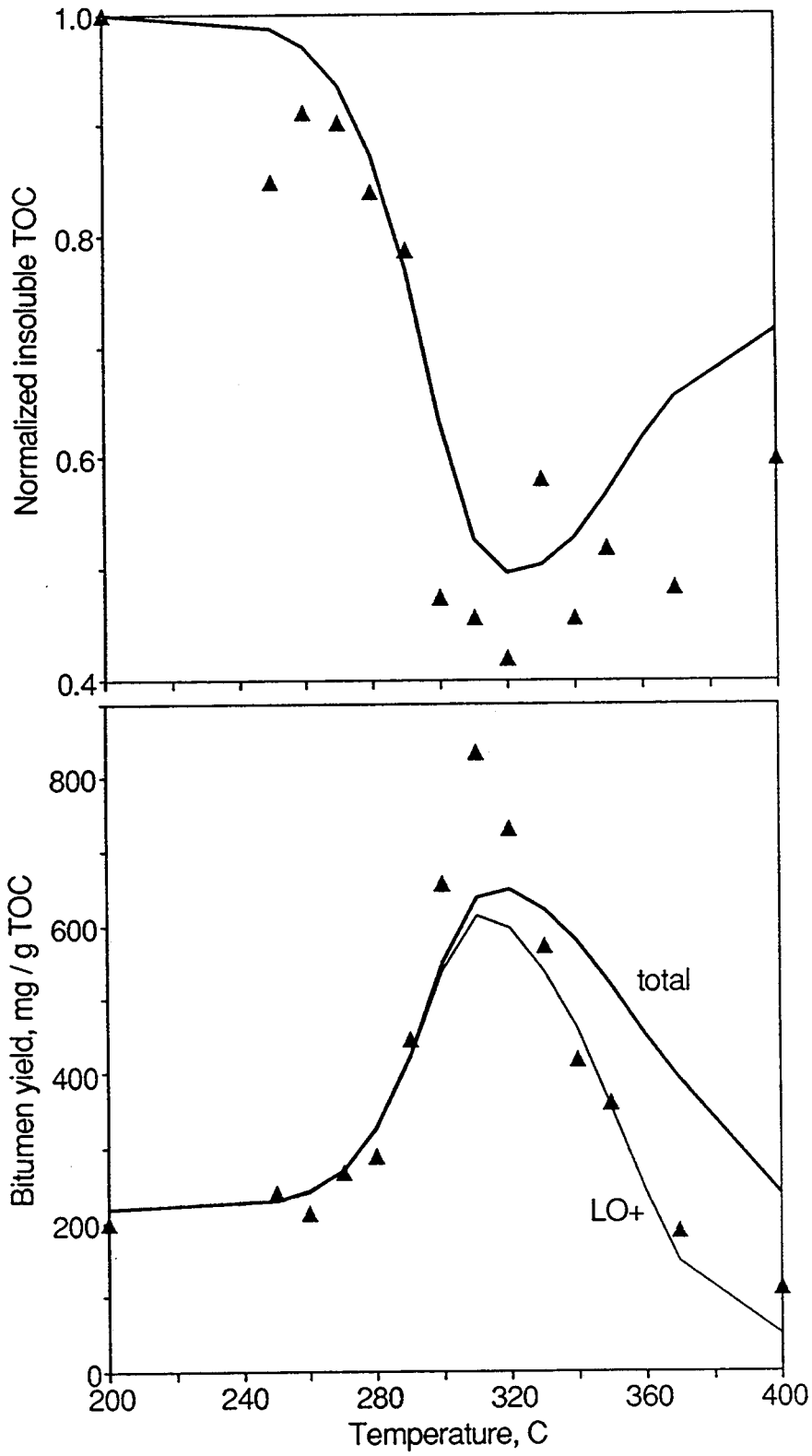


Figure 33. Bitumen and insoluble organic matter yields for hydrous pyrolysis for 72 h at the indicated temperature. The data points are for sample QL7 and the lines are calculated using the PMOD mechanism given in Table 18.

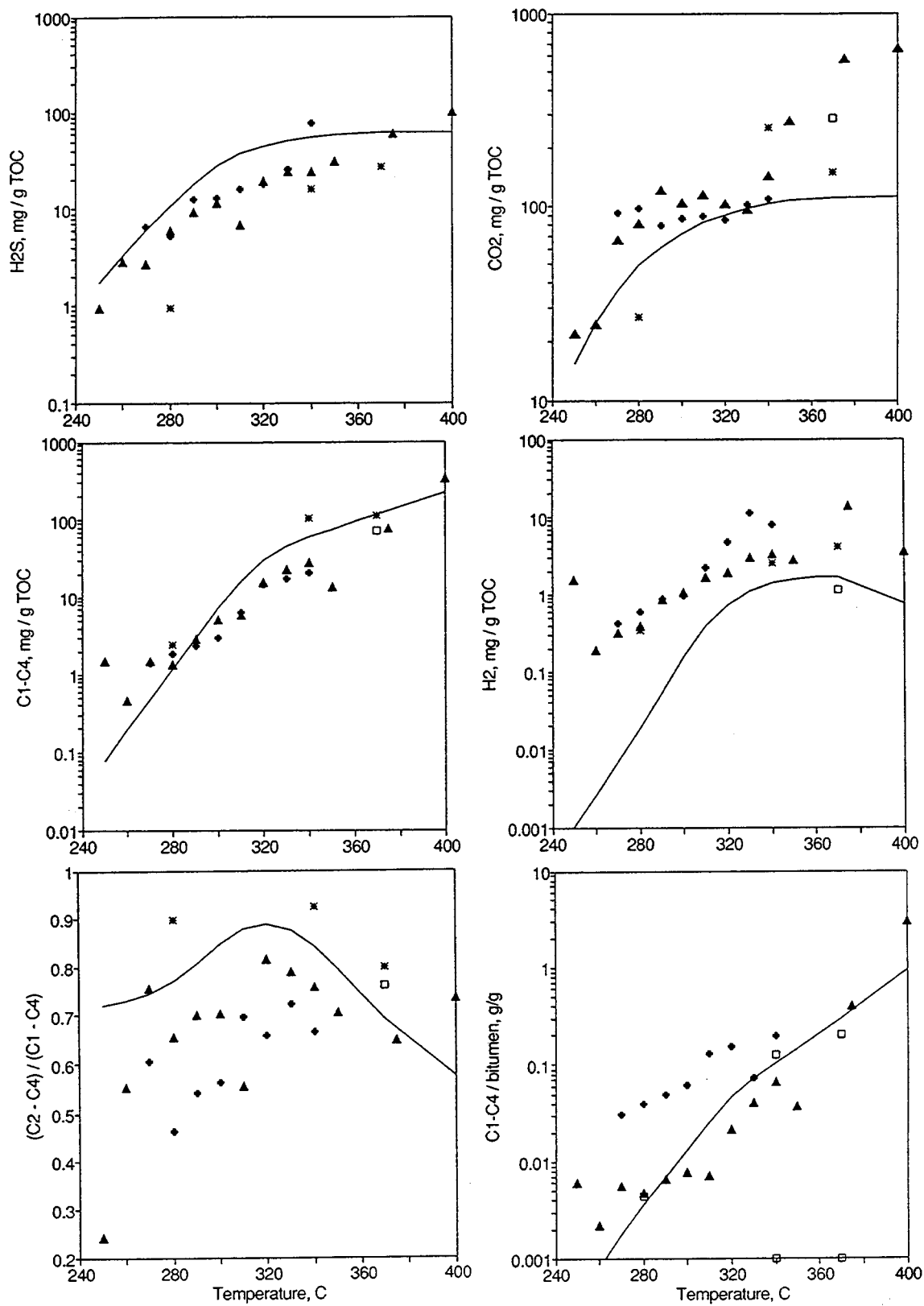


Figure 34. Comparison of measured and calculated gas yields and composition for hydrous pyrolysis at 72 h. Symbol code: QL7—filled triangles; 26D2—open squares; JGE28—asterisks, QLN—pluses.

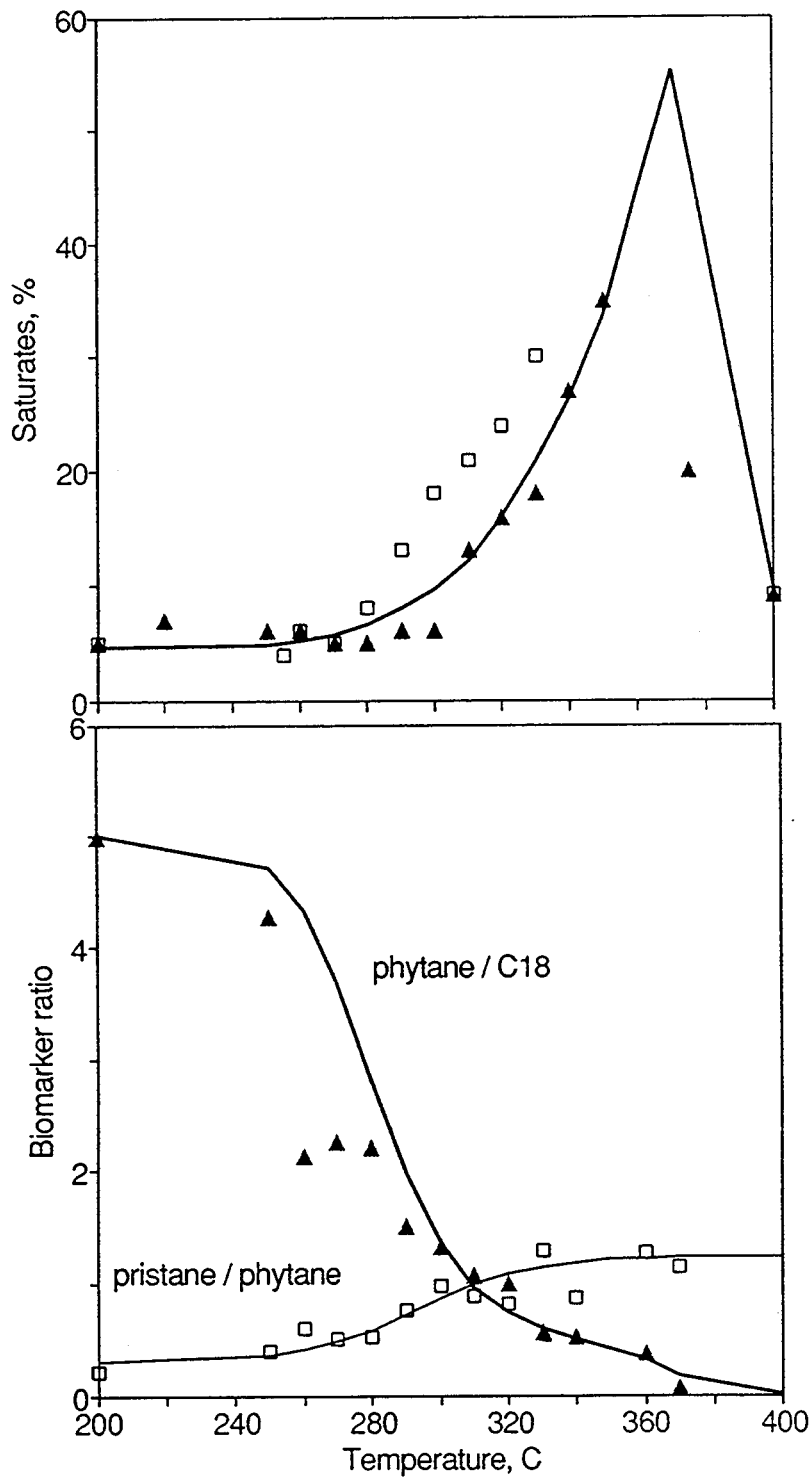


Figure 35. Oil composition as a function of hydrous pyrolysis temperature. In the upper figure, the triangles are for sample QL7 and the squares are for sample 26D2. In the lower figure, the symbols are both for sample QL7. The solid line represents a PMOD calculation.

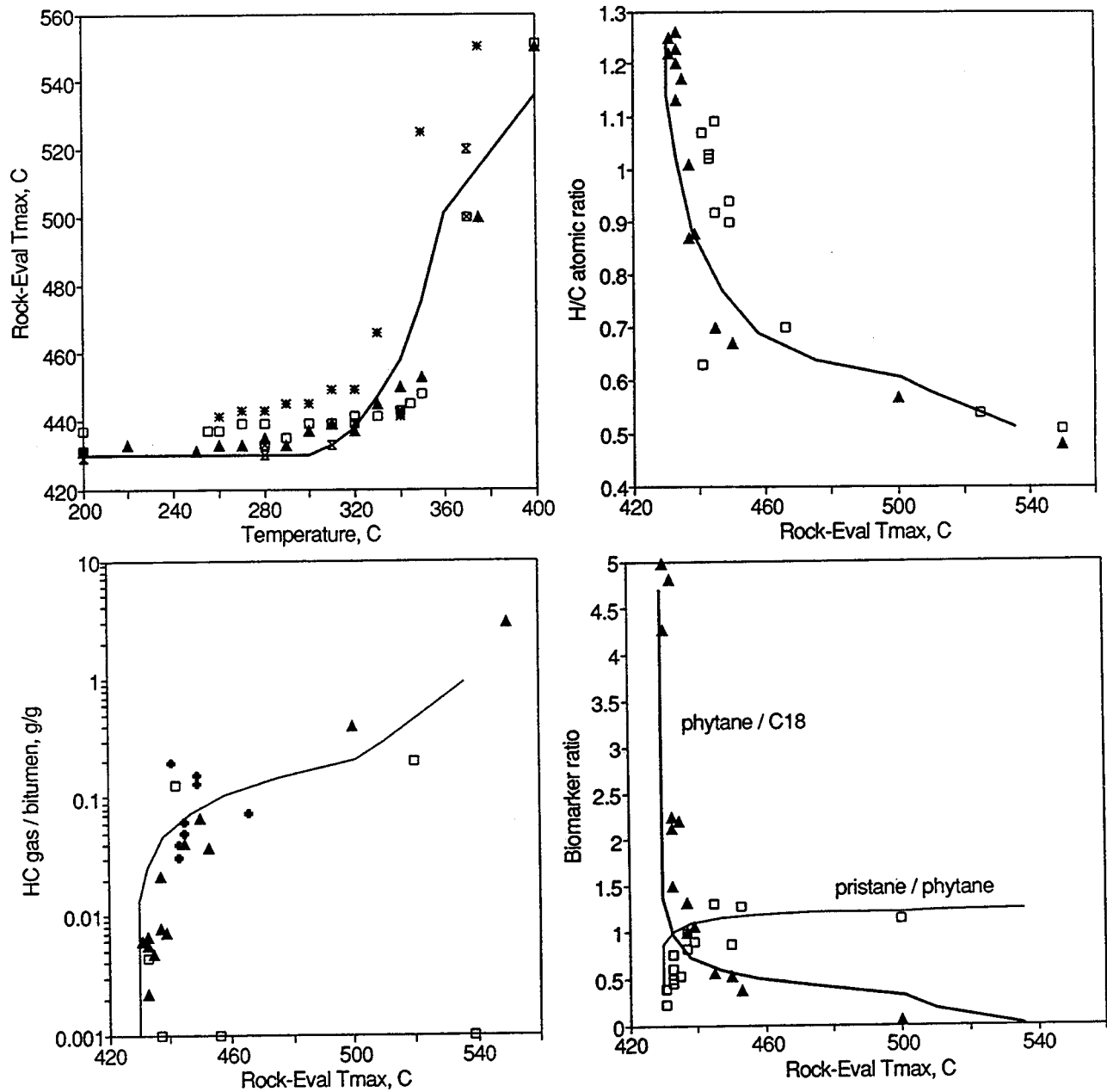


Figure 36. Relationship between Rock-Eval T<sub>max</sub> of the extracted residue and other variables. The solid lines represent PMOD calculations and the points represent hydrous pyrolysis data from Tables 10-14. Symbol code: QL7–filled triangles; 26D2–open squares; 26D2′–squares with x; JGE28–asterisks, QLN–pluses.

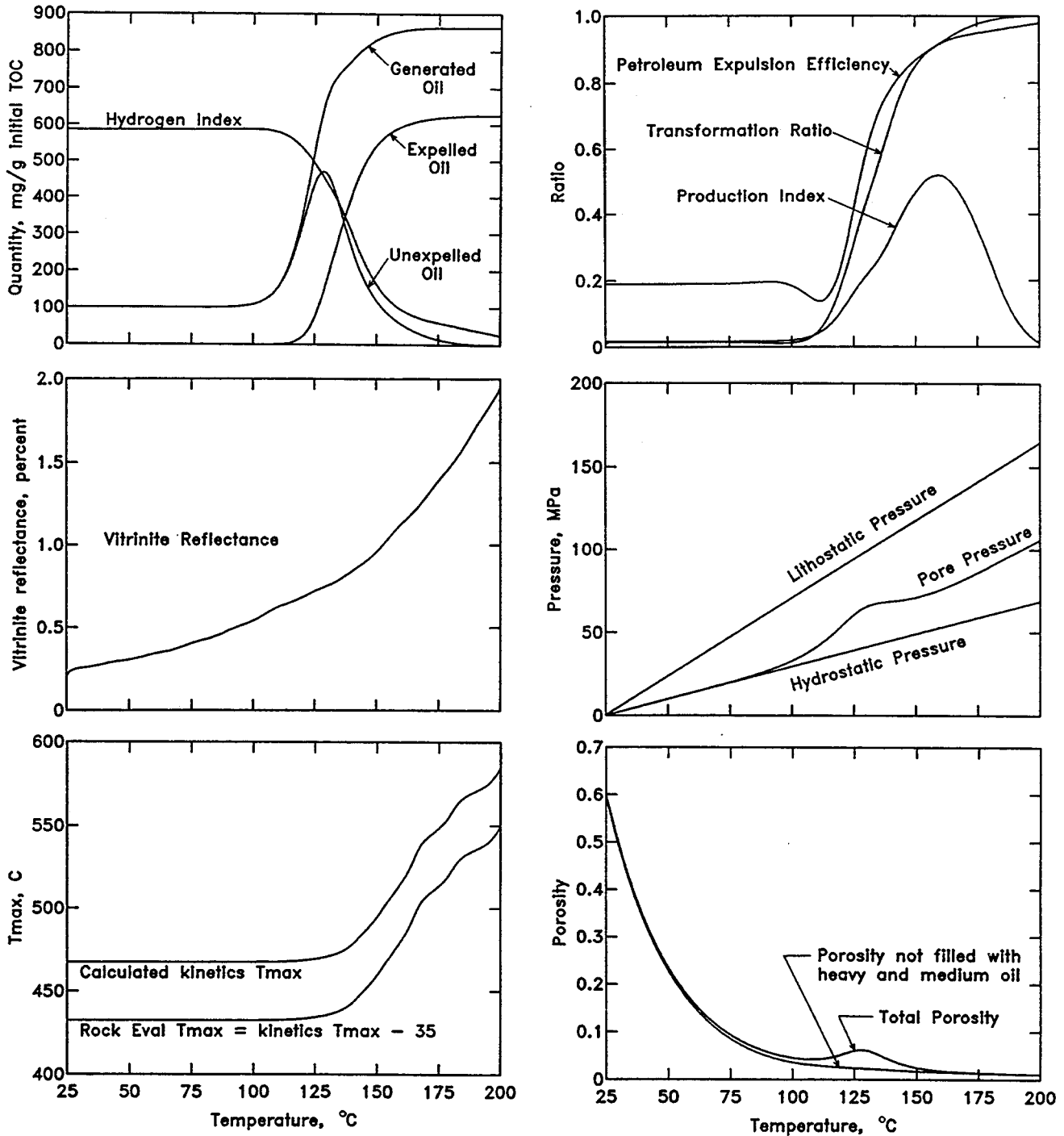


Figure 37. Selected results for the base case of the generic parameter study, using 3.8 wt% TOC, 4 °C/My heating rate, and 25 °C/km geothermal gradient.

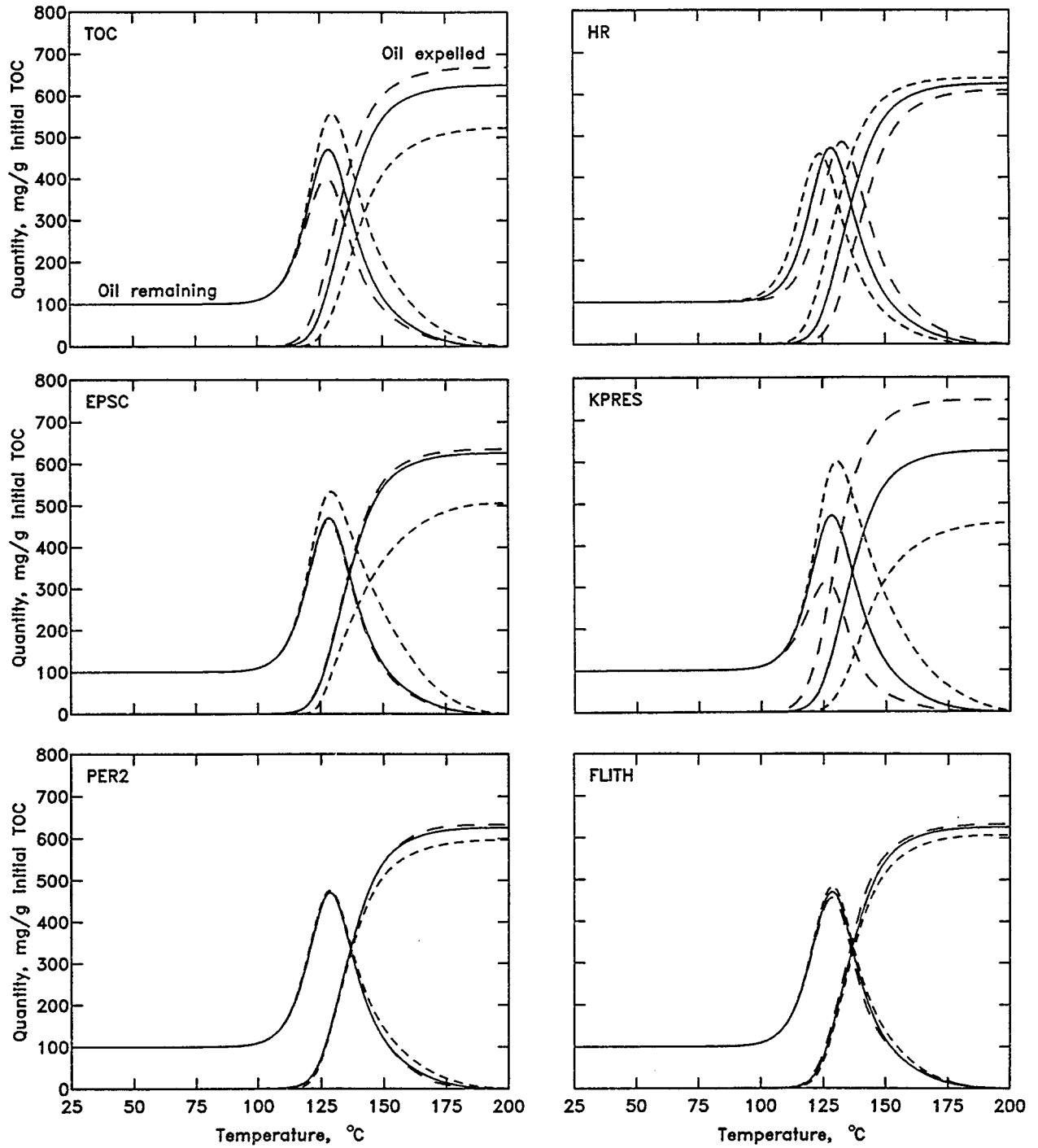


Figure 38. Oil remaining in and expelled from the source rock for variations in the parameter indicated in the upper left corner of each graph. In this figure and the subsequent 6 figures, the solid line is for the base value of the parameter, the small-dashed line is for the lower value of the parameter, and the large-dashed line is for the higher value of the parameter.

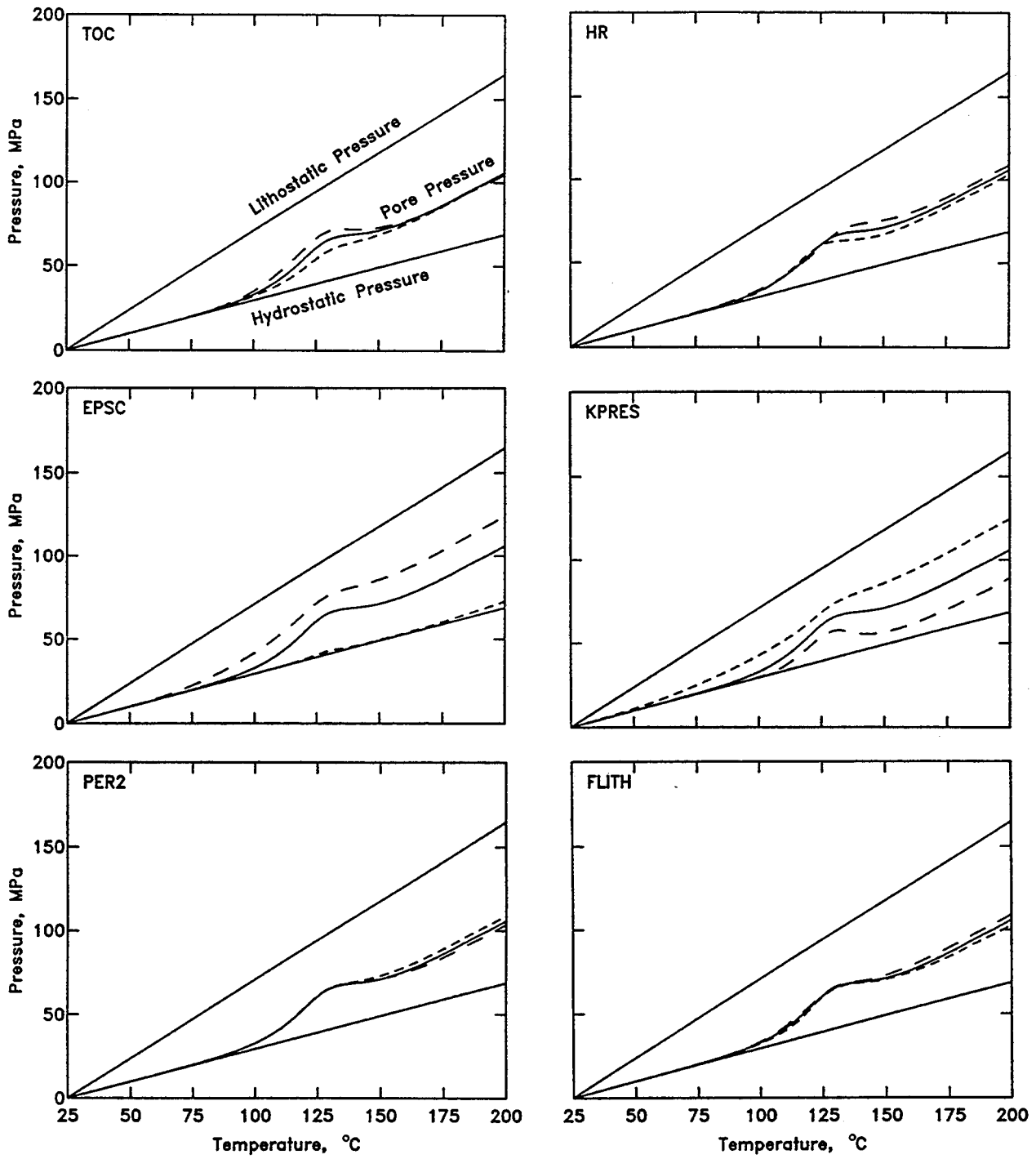


Figure 39. Pore pressure for the indicated parameter variations (see Table 19).

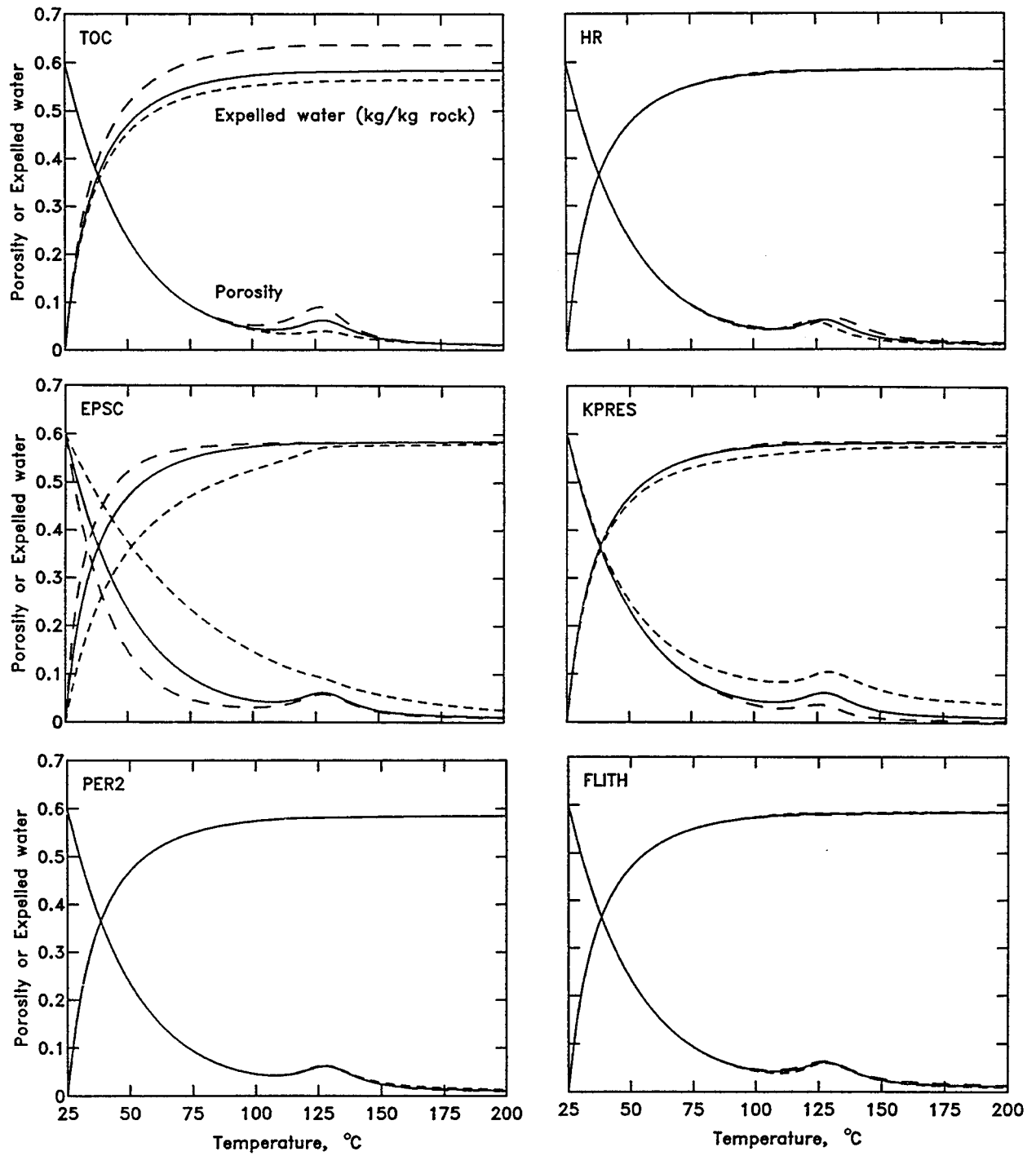


Figure 40. Rock porosity and cumulative expelled water for the indicated parameter variations (Table 19).

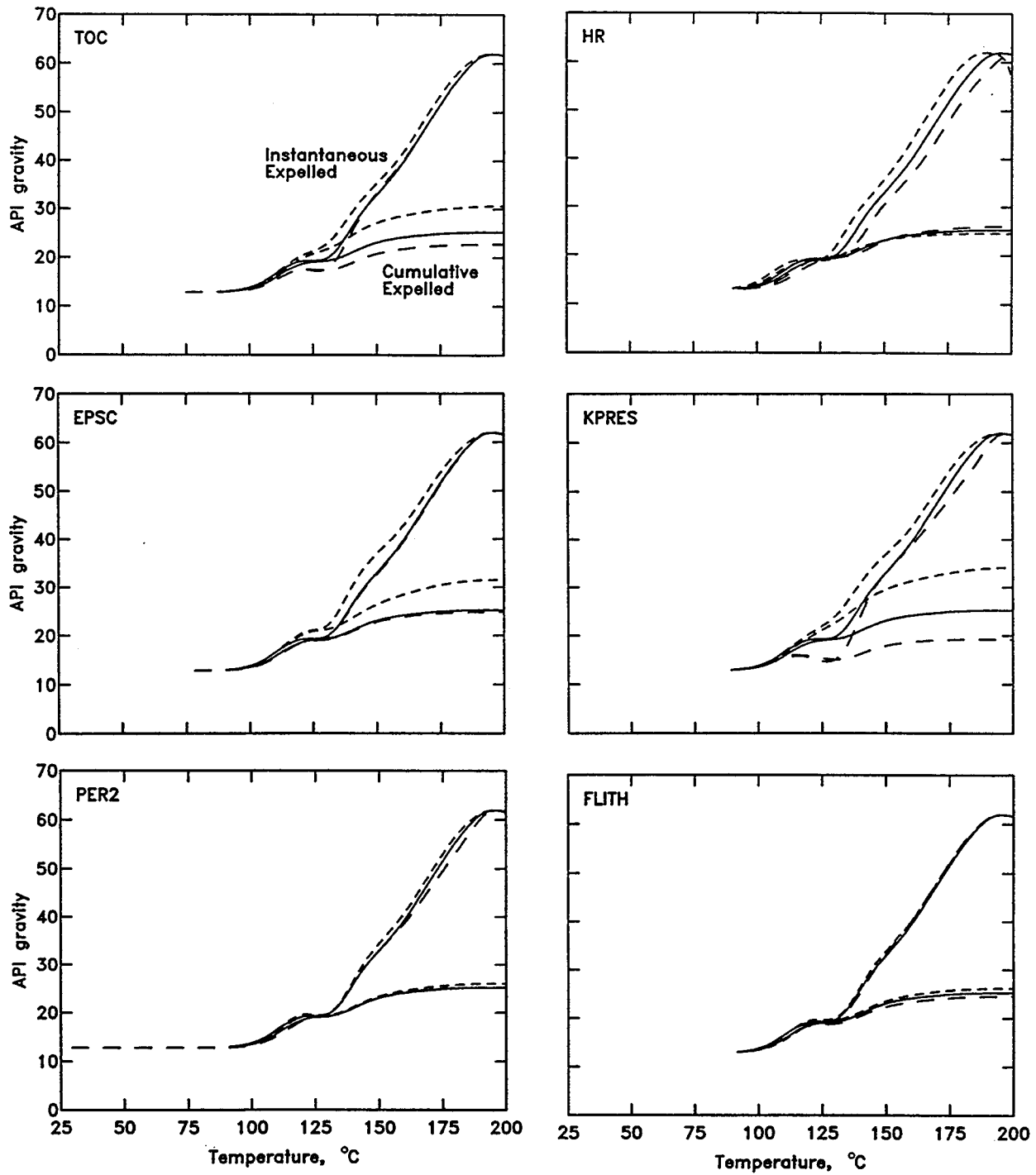


Figure 41. API gravity of the expelled oil for the indicated parameter variations (Table 19).

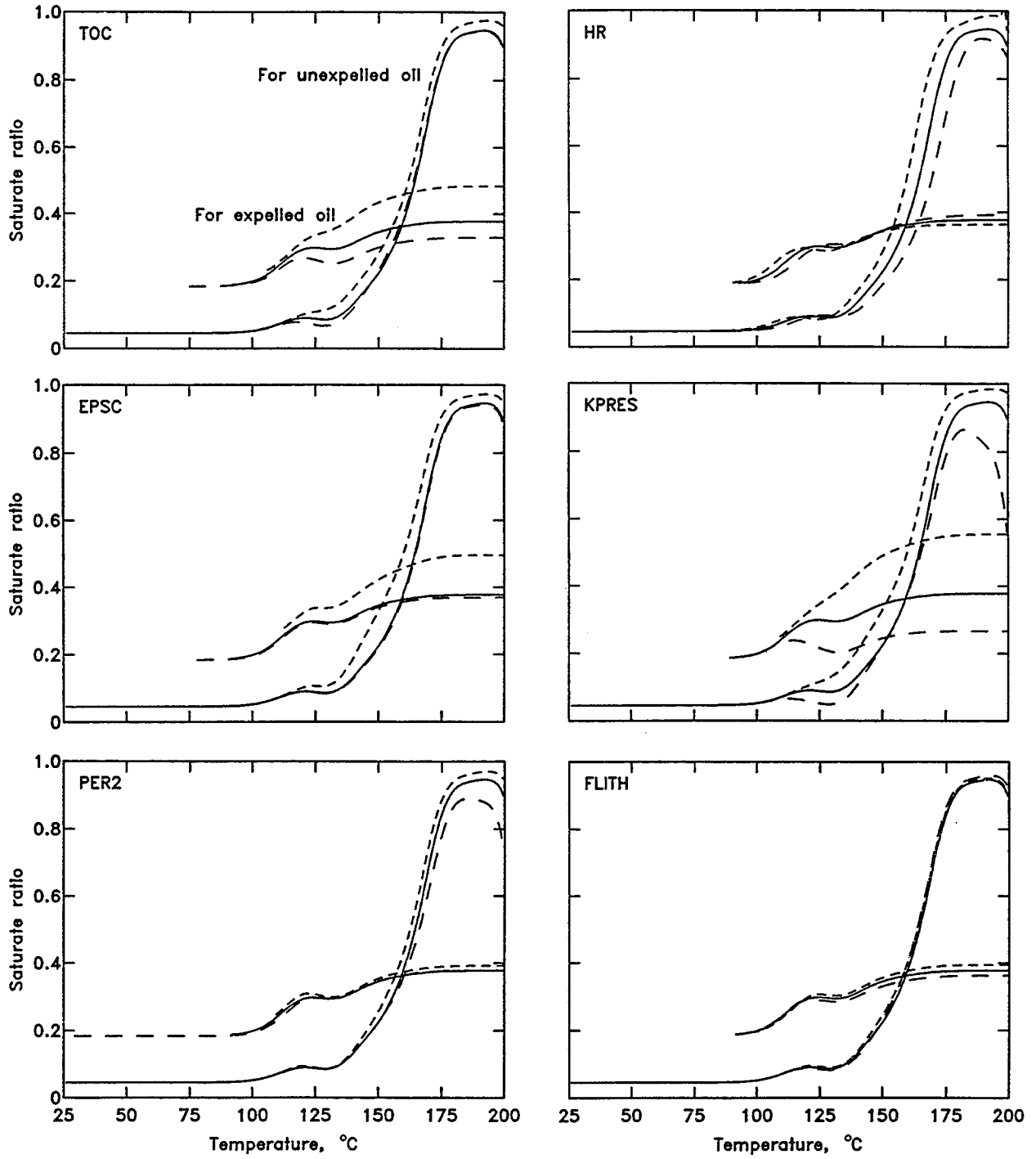


Figure 42. Saturated oil fraction of the expelled and unexpelled oil for the indicated parameter variations (Table 19).

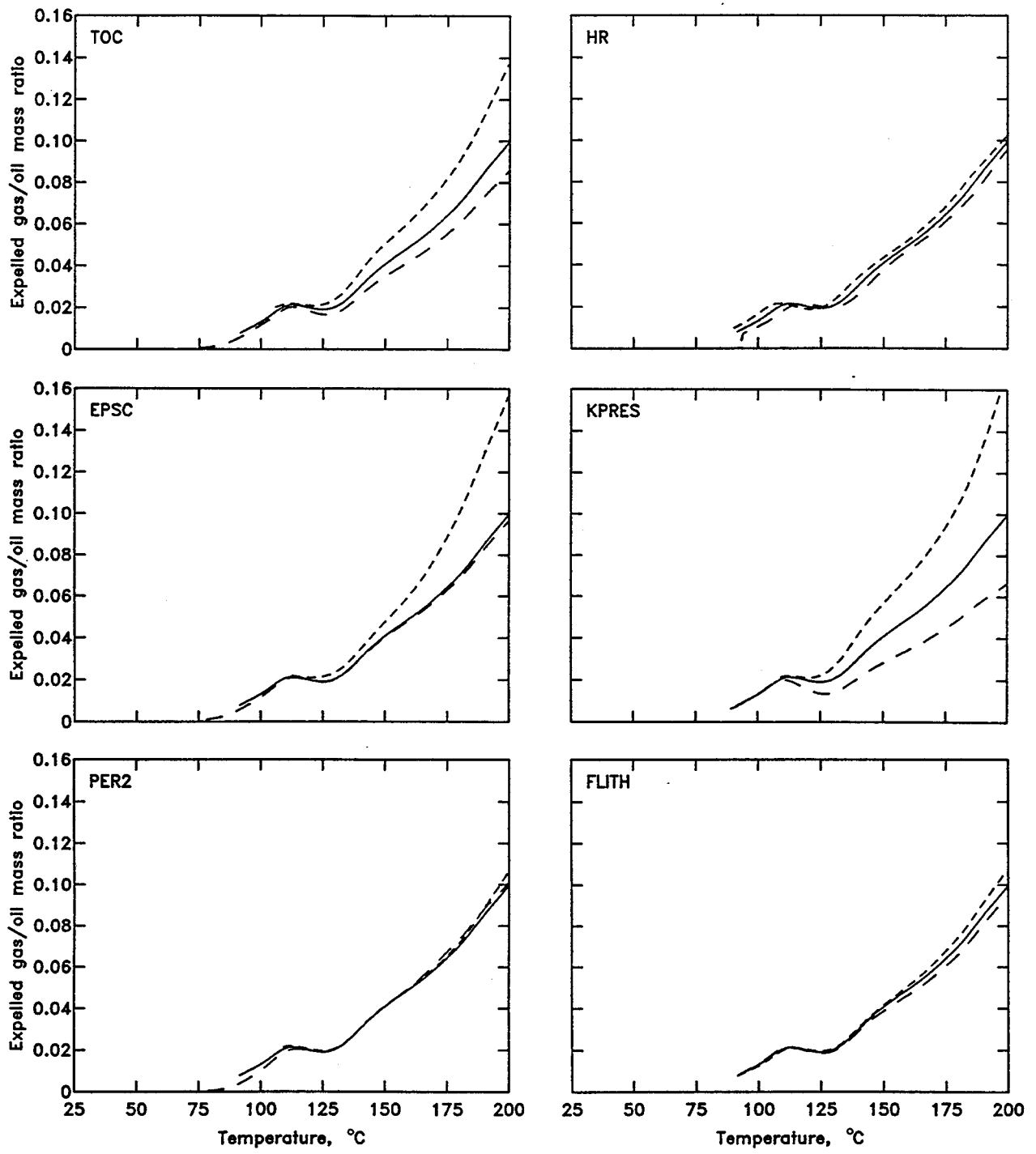


Figure 43. Gas/oil mass ratio of the expelled fluid for the indicated parameter variations (Table 19).

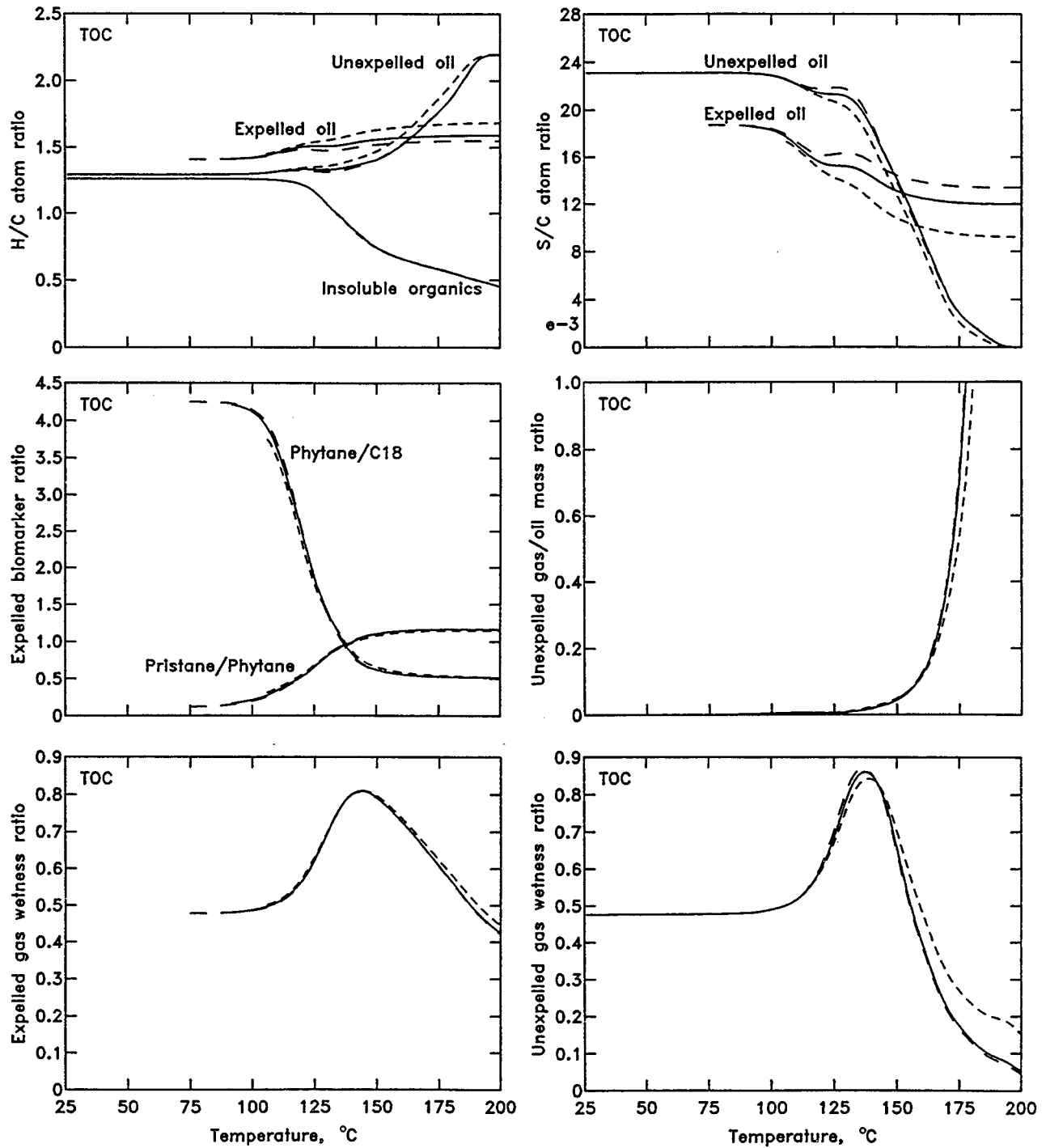


Figure 44. Effect of variations in TOC on biomarker ratios of the expelled oil, gas/oil mass ratio of the unexpelled fluid, expelled wetness index, unexpelled wetness index, H/C atom ratios, and S/C atom ratios.

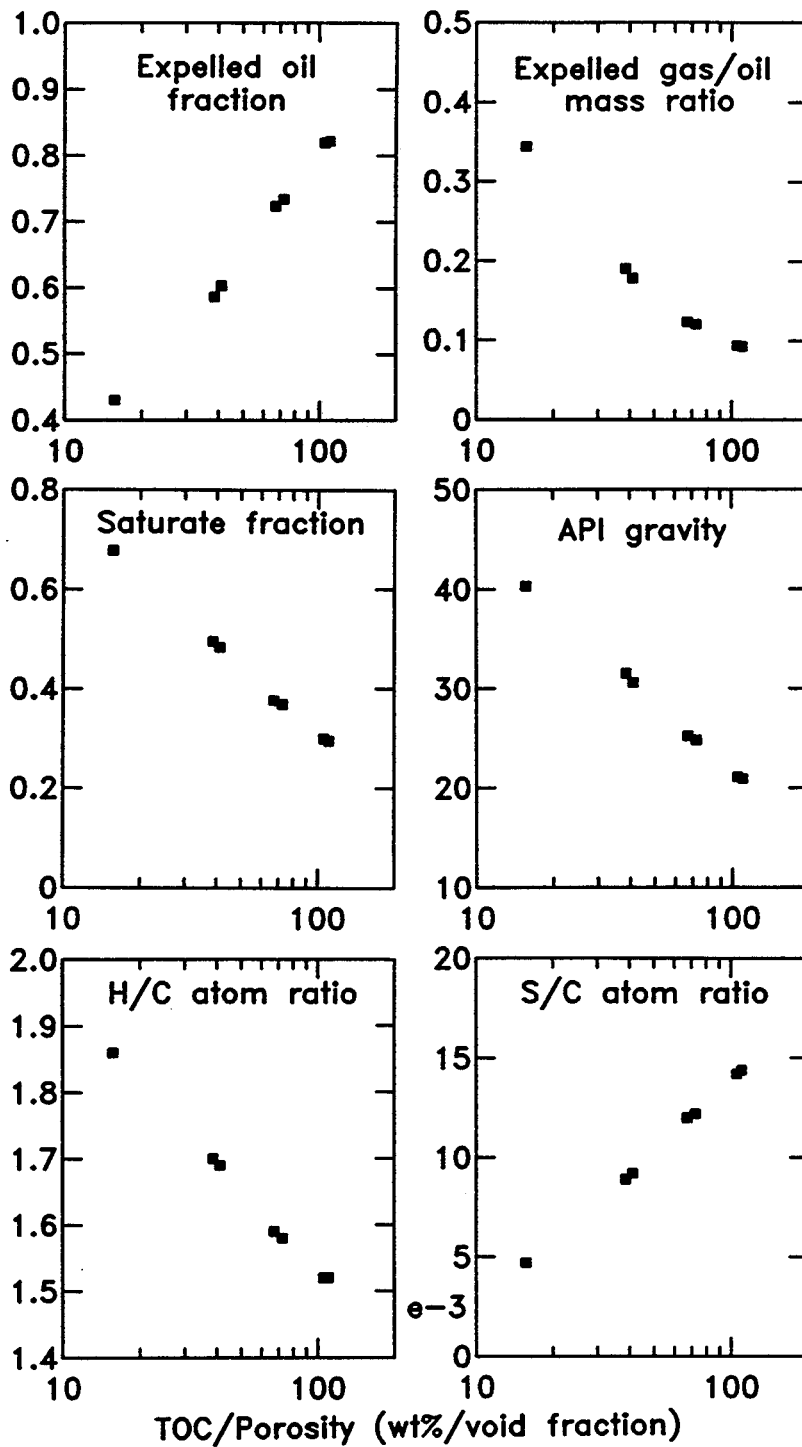


Figure 45. Correlation of important base case results with the ratio of initial TOC to the rock porosity at the midpoint of oil generation. The residence time of the fluid in the rock is approximately proportional to this ratio.

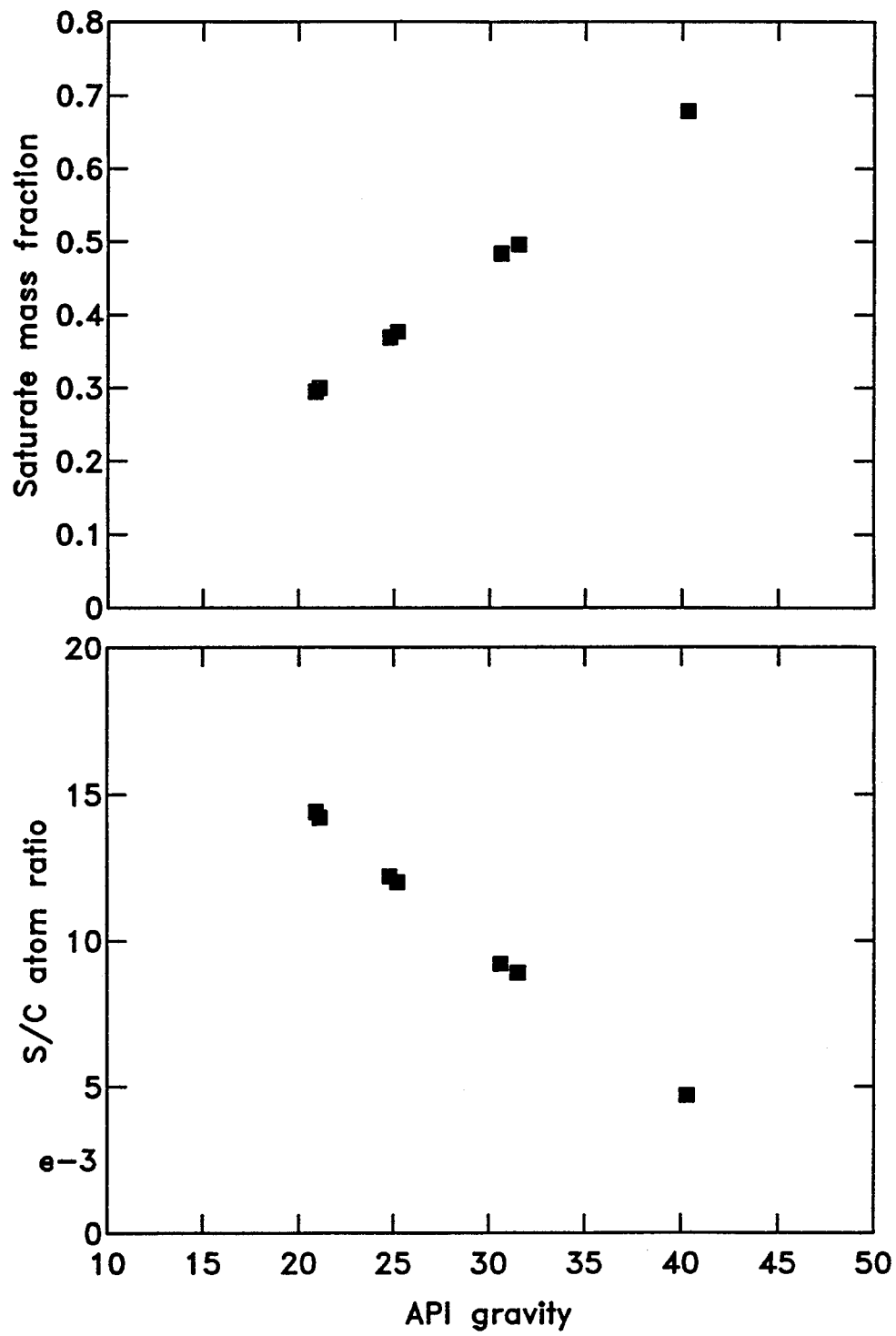


Figure 46. The results which correlated well with the approximate measure of fluid residence time correlate very well with each other.

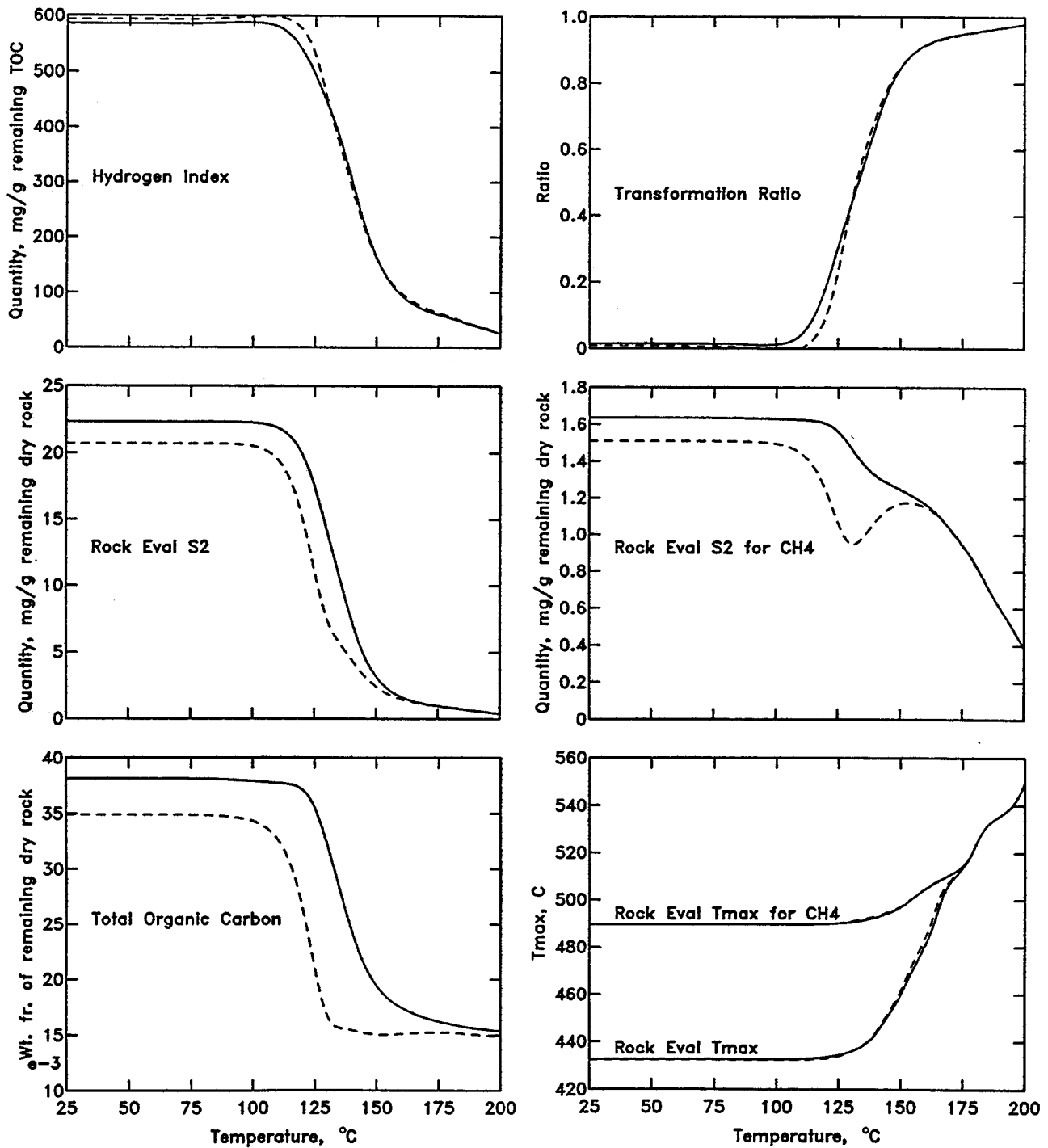


Figure 47. Effect of solvent extraction on various properties calculated from the Rock Eval simulation during the base case run. The solid line is without extraction and the dashed line is with extraction.

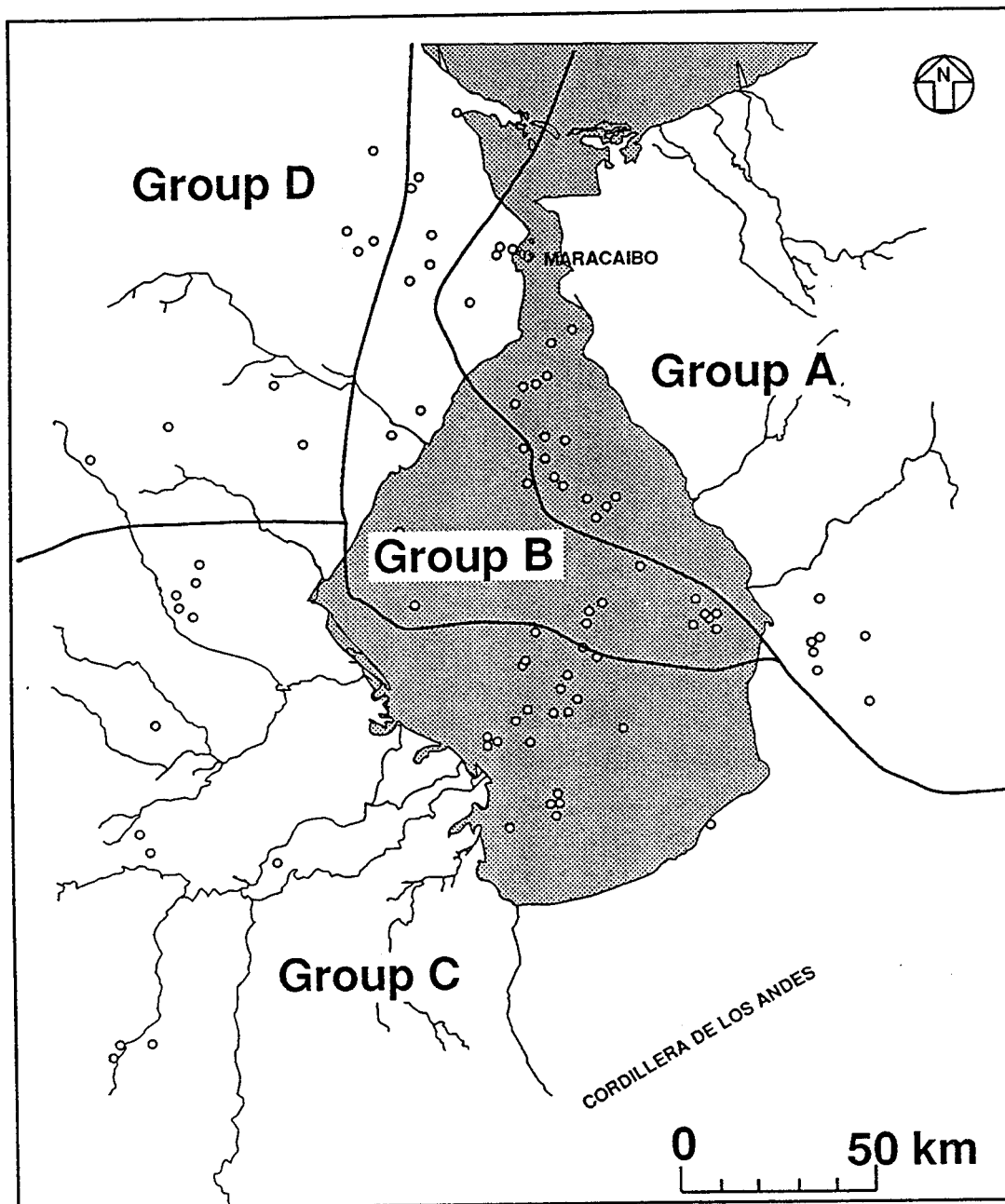


Figure 48. Map showing the location of the four different groups of oil generation characteristics based on kinetic modeling. Group A—generation begins and goes to completion during the late Eocene (48-40 Ma); Group B—generation begins in the late Eocene, is shut off early and resumes during the late Miocene (about 8 Ma) but does not go to completion—actively generating today; Group C—generation begins and goes to completion during the late Miocene to early Pliocene (8-2 Ma); Group D—generation begins during the late Miocene (12 Ma) and continues to the present—actively generating today.

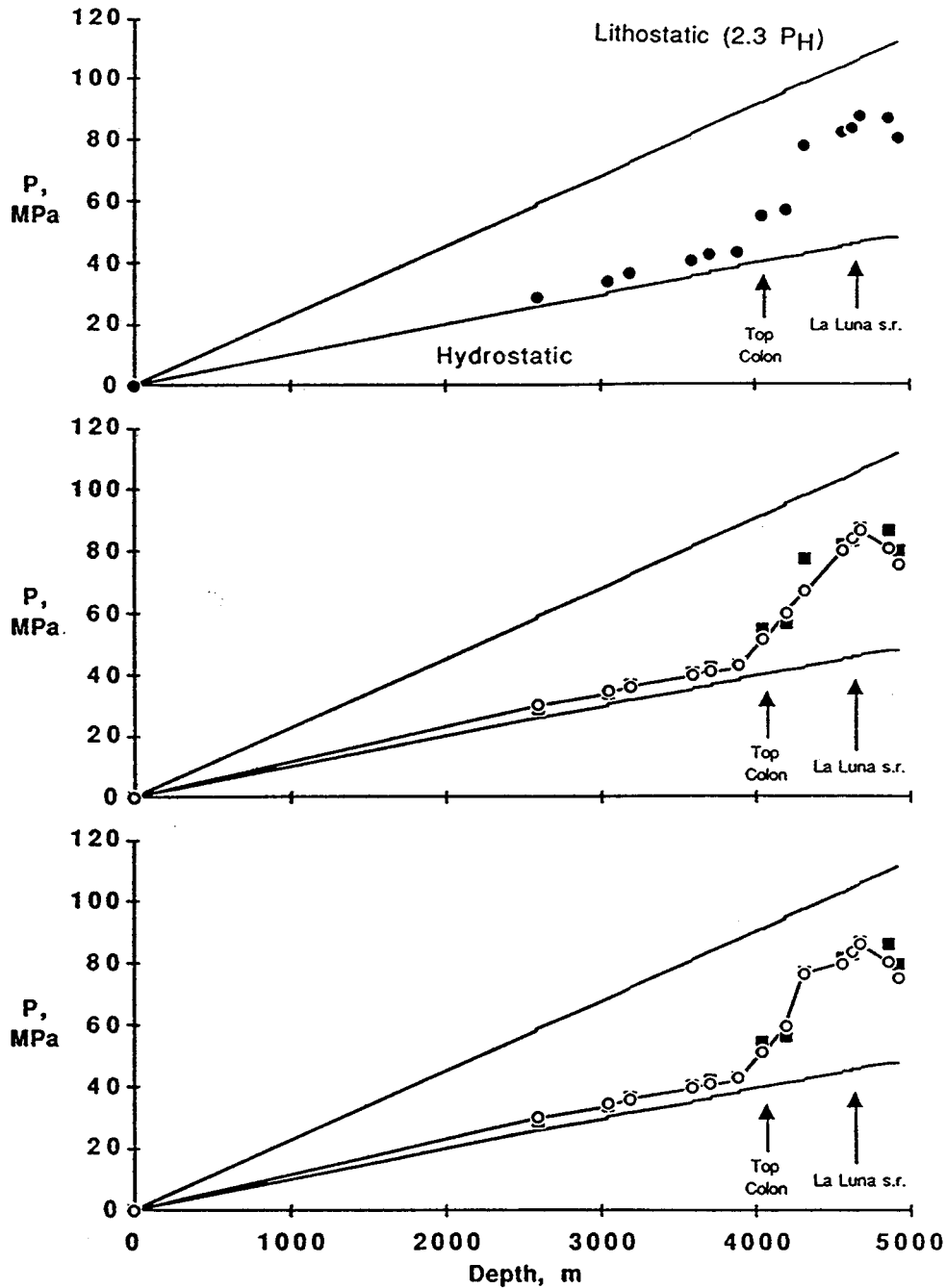


Figure 49. (a) Measured pore pressure (from mud weights) versus depth for well VLE686 in the Maracaibo Basin. Upper and lower solid lines are for lithostatic and hydrostatic pressure, respectively. (b) Calculated (open circles) and measured (solid squares) values of pore pressure in well VLE686. Calculated pore pressure at 4700 m depth in the La Luna shale is from the PMOD calculation and it is assumed that a steady state condition exists and that pressure drops off linearly above and below that depth. (c) Plot similar to (b) except that a contribution (10.2 MPa) of pore pressure caused by compaction disequilibrium at 4328 m depth is included.

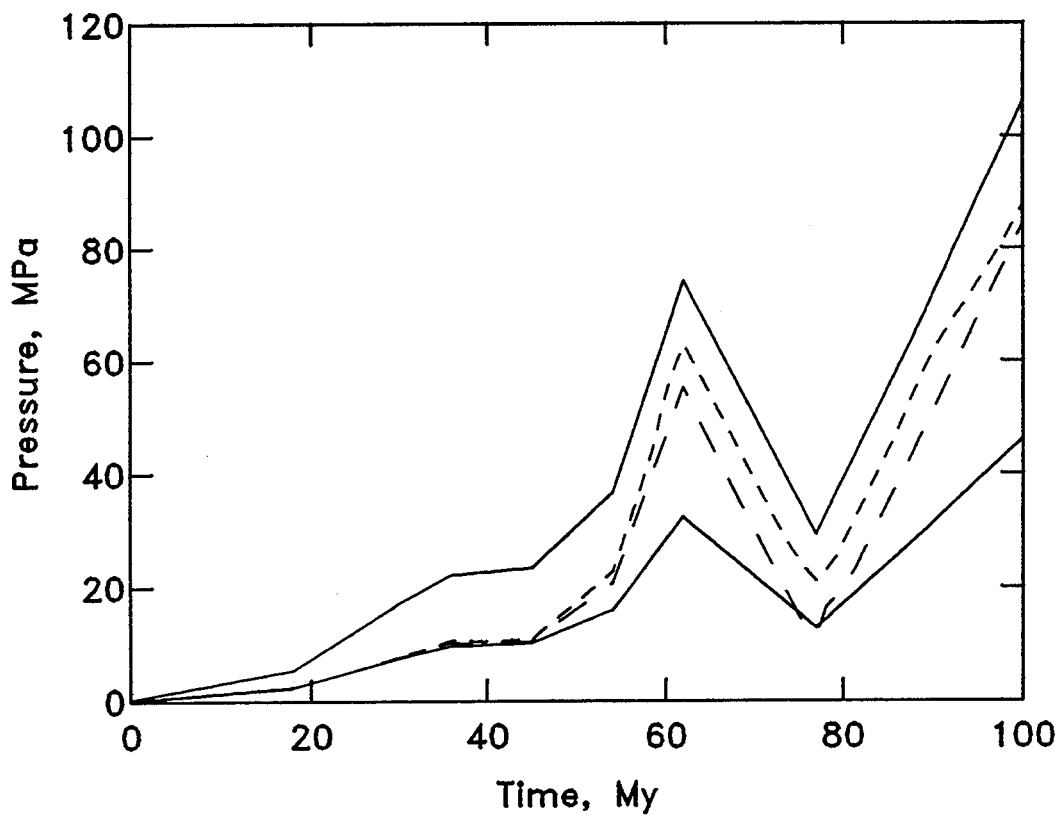


Figure 50. Calculated pore pressure versus time in the La Luna shale (4700 m present day depth), well VLE686. Upper solid curve—lithostatic pressure; lower solid curve—hydrostatic pressure; short dash line—6.0% TOC calculation; long dash line—0 % TOC calculation.

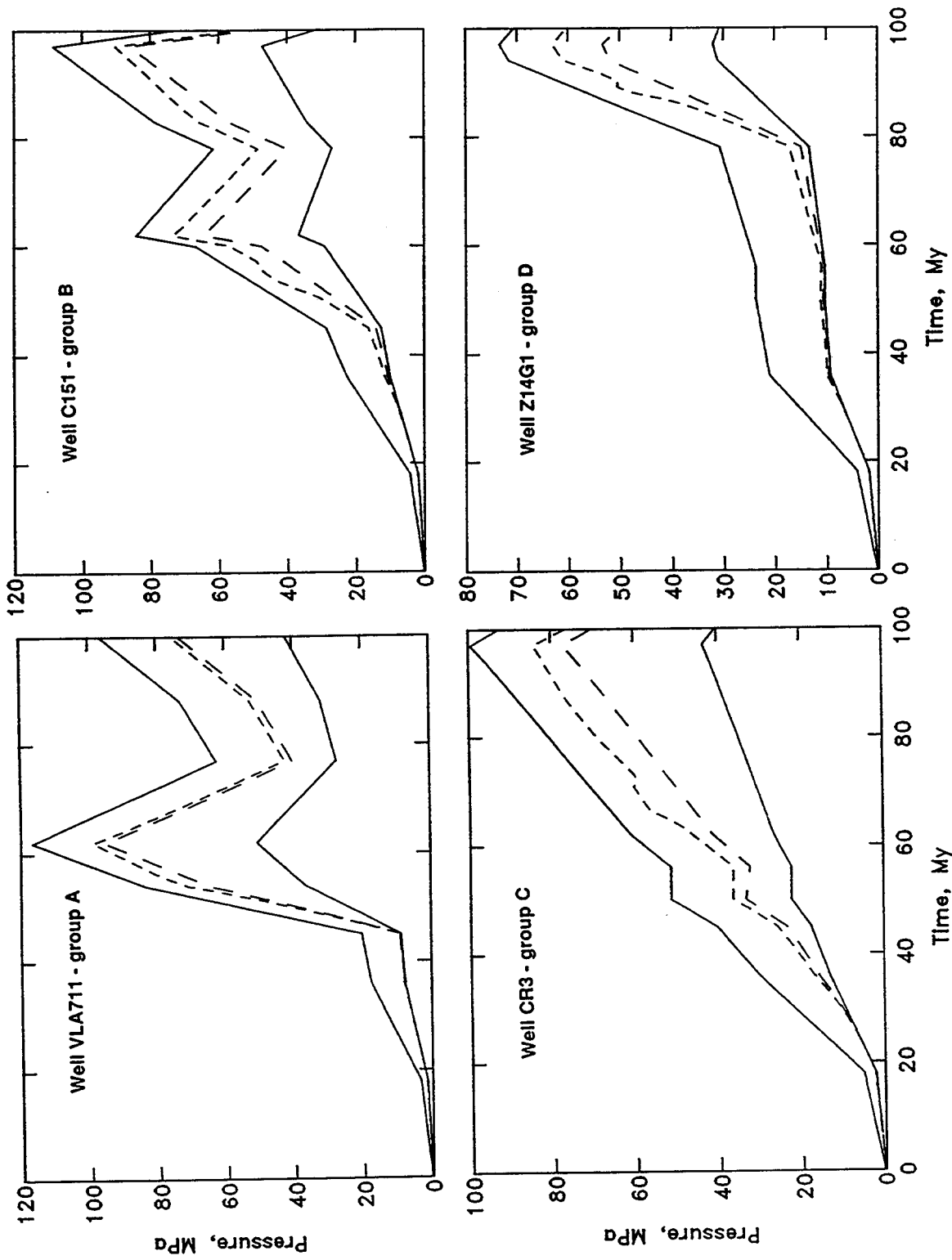


Figure 51. Calculated pore pressure curves for the La Luna shale in representative wells for each of the groups shown in Figure 48. Upper solid curve—lithostatic pressure; lower solid curve—hydrostatic pressure; long dash line—calculation with organic matter; short dash line—calculation with zero TOC.

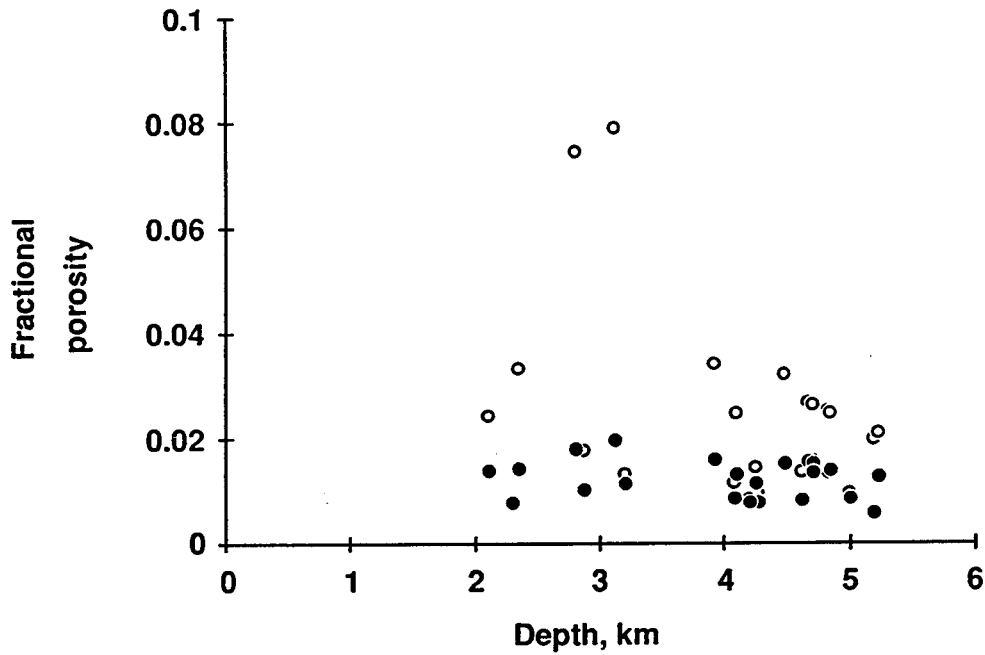


Figure 52. Present day porosity at the depth of the La Luna Formation calculated with PMOD for the leaky system case with  $EPSC = 2 \times 10^{-7} \text{ Pa}^{-1}$  and  $KPRES = 1 \times 10^{-20}$ . Total porosity is represented by open circles; partial porosity (the total porosity less the portion filled with bitumen) is represented by solid circles.

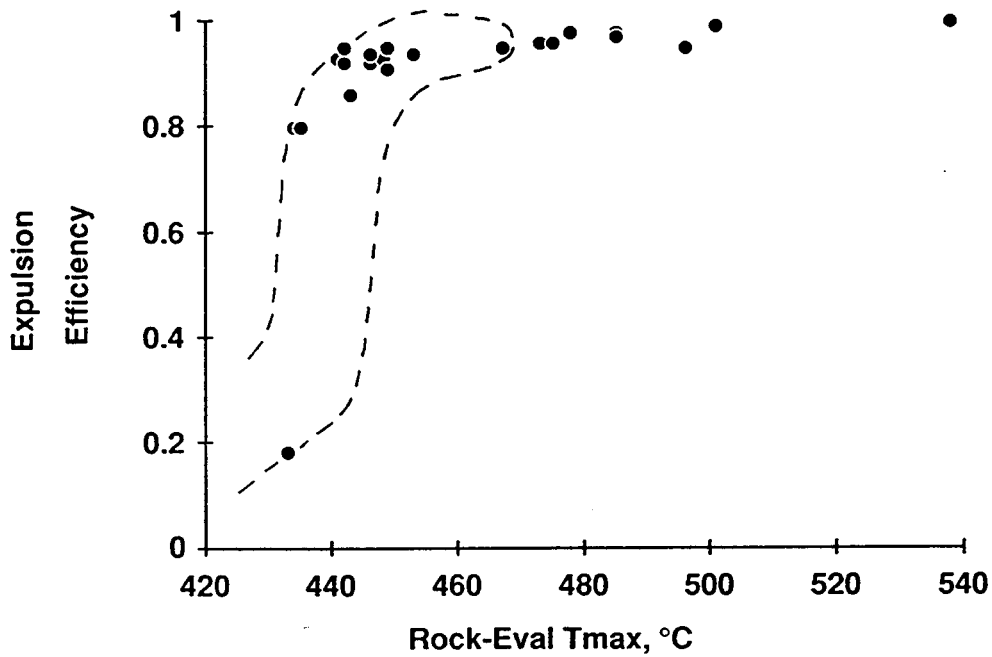


Figure 53. Calculated expulsion efficiency versus calculated  $T_{max}$  for the leaky system case (same parameters as Fig. 52). The outline of the range of measured values (from Talukdar *et al.*, 1989) is shown by the dashed line.

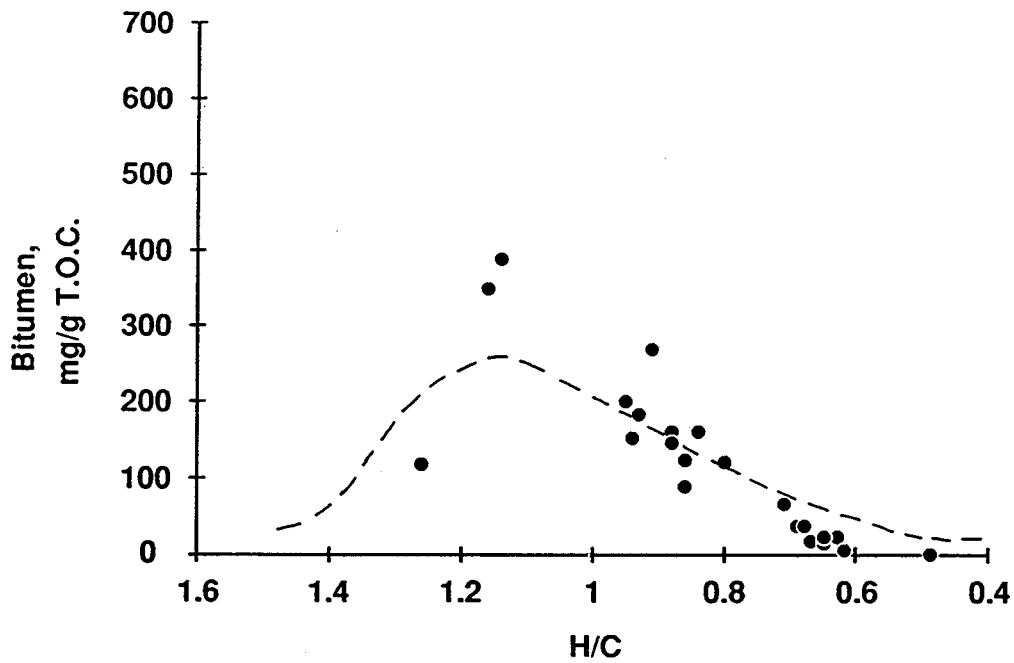


Figure 54. Calculated bitumen versus calculated atomic H/C ratio of the kerogen for the leaky system case (same parameters as Fig. 52). The outline of the general trend of the measured values (from Talukdar *et al.*, 1987, Fig. 7) is shown by the dashed line.

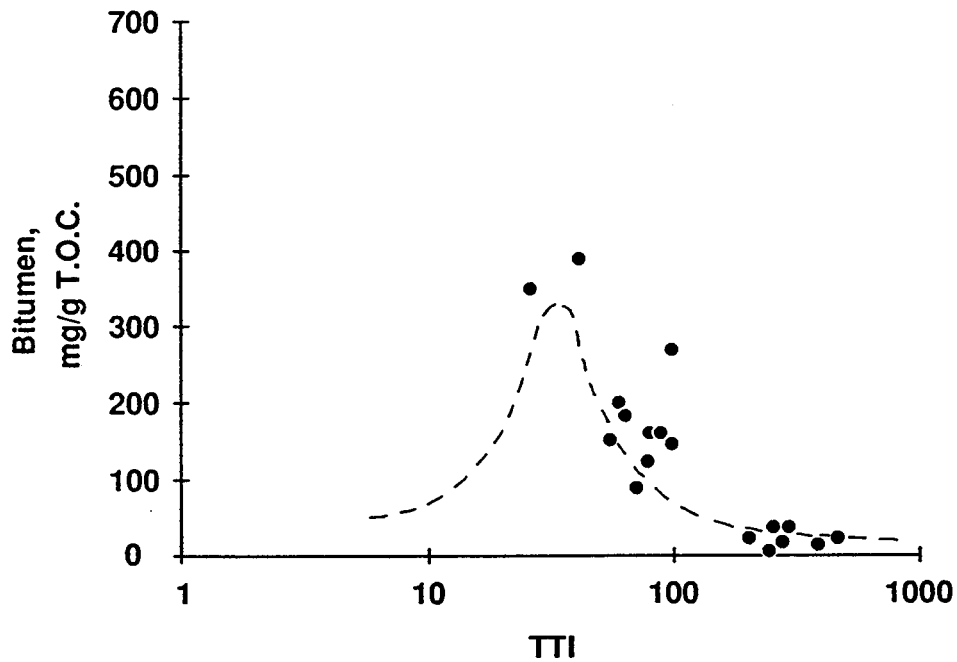


Figure 55. Calculated bitumen versus TTI for the leaky system case (same parameters as Fig. 52). The outline of the general trend of the measured values (from Talukdar *et al.*, 1986, Fig. 5) is shown by the dashed line.

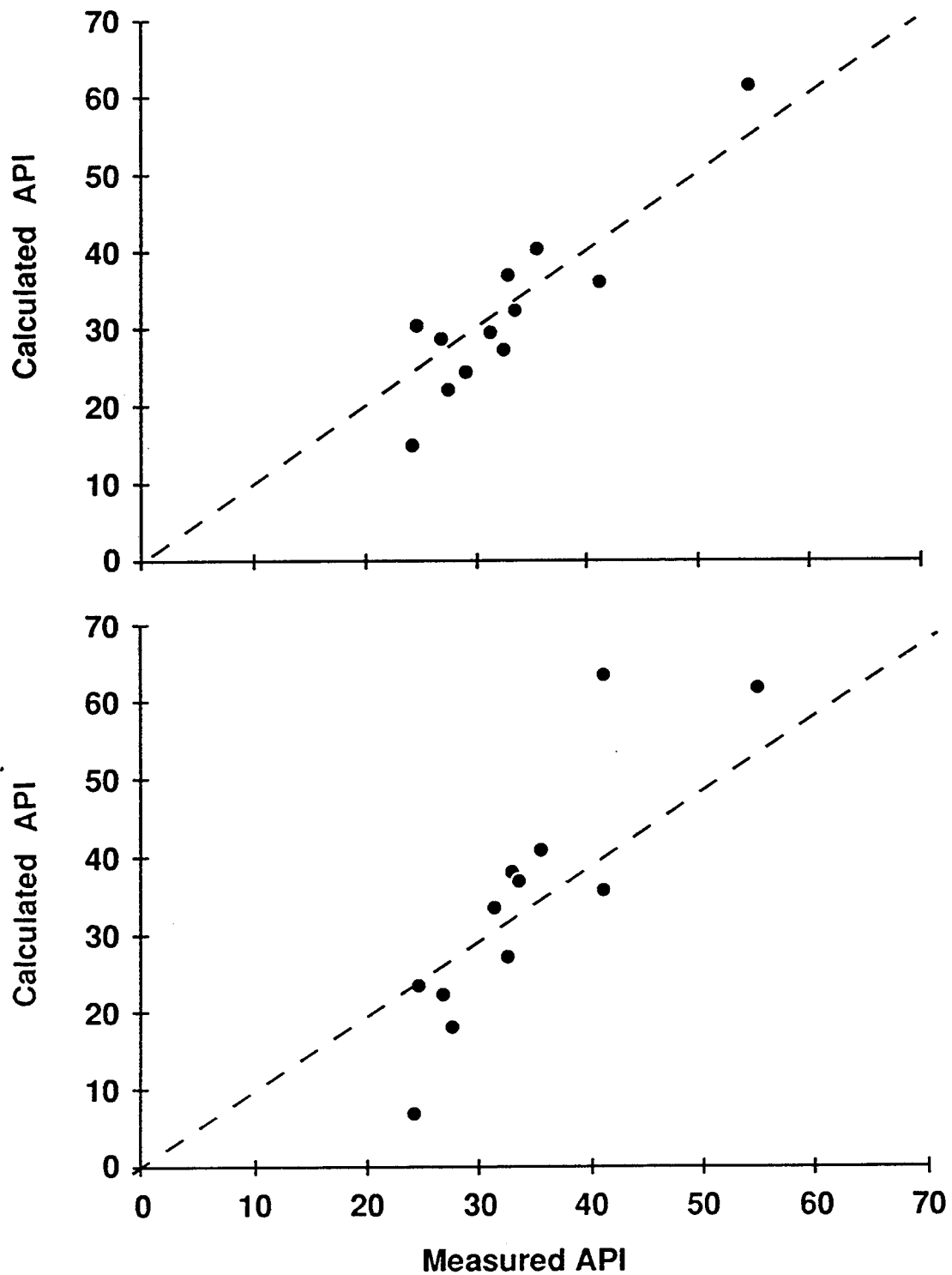


Figure 56. (a) Comparison of calculated and measured API gravity for the leaky system (same parameters as Fig. 52). Calculations of both differential and cumulative gravity are shown. (b) Similar plot for the closed system case. Perfect agreement between calculated and measured values would result in points following the diagonal dashed line.

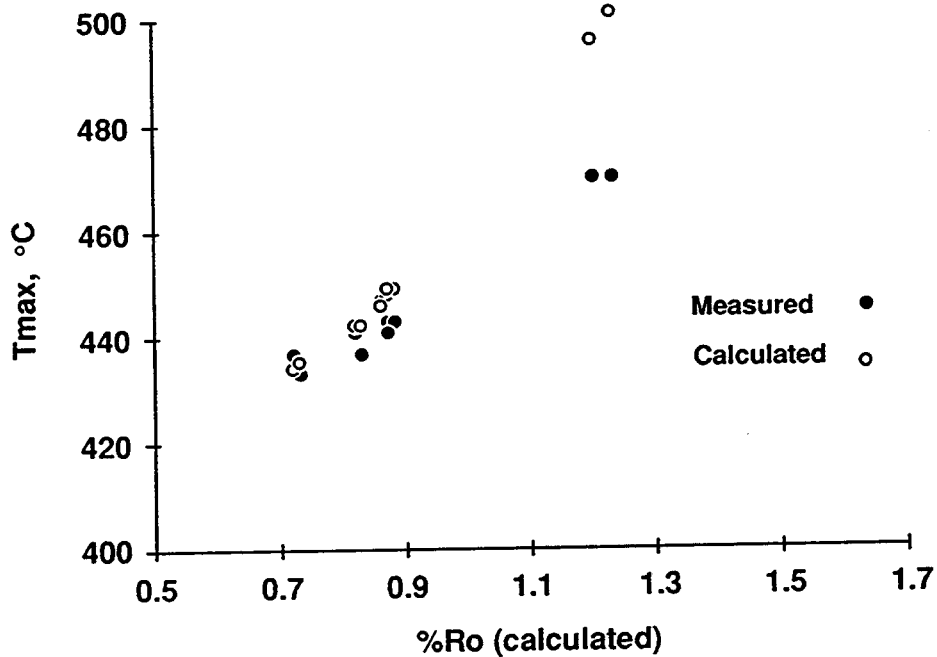


Figure 57. Comparison of calculated and measured  $T_{max}$  as a function of calculated vitrinite reflectance (results are essentially the same for leaky and closed system cases).

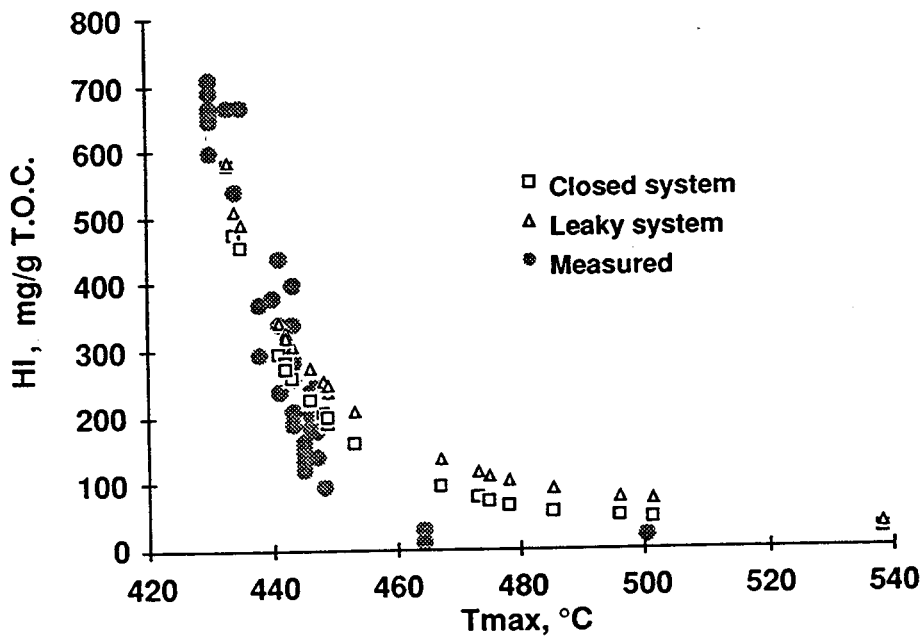


Figure 58. Measured HI (shaded dots) versus measured  $T_{max}$  for wells in the Maracaibo Basin compared with calculated HI versus calculated  $T_{max}$  for all of the wells modeled with PMOD, for both the leaky and closed system cases.

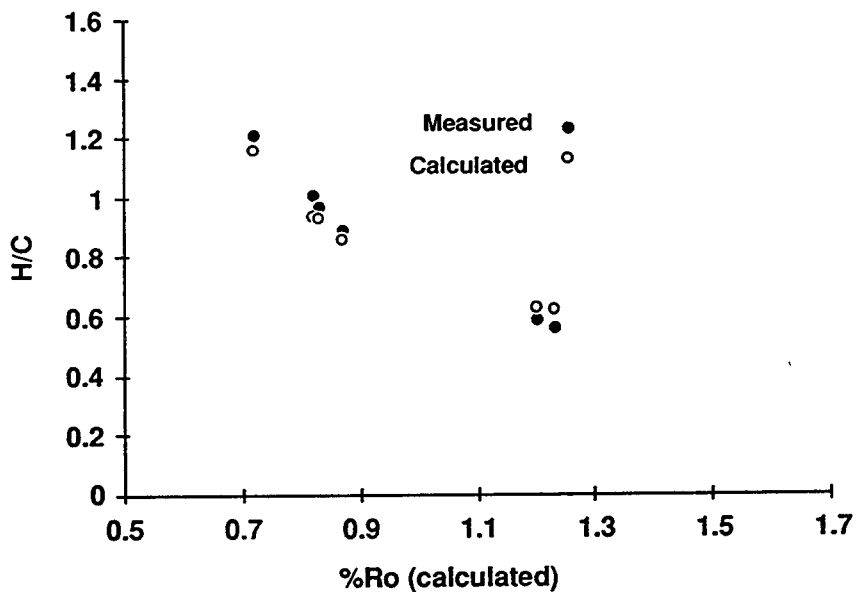


Figure 59. Comparison of measured and calculated H/C ratio of organic matter remaining in the source rock versus calculated vitrinite reflectance.

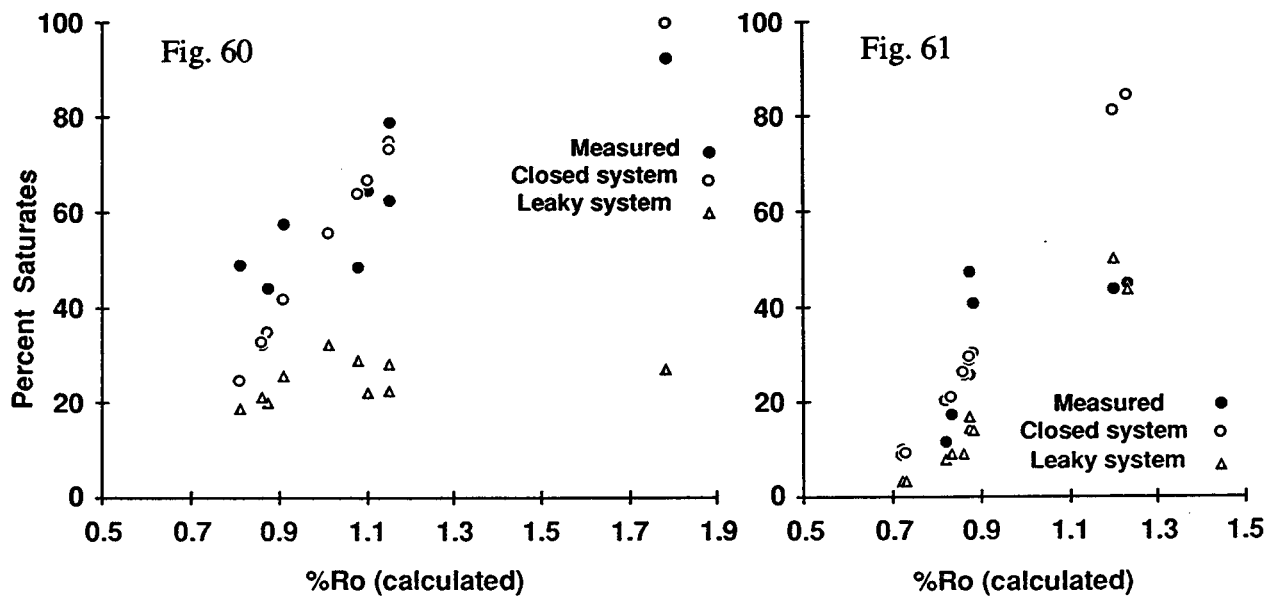


Figure 60. Calculated and measured values of saturate content of oils from Cretaceous reservoirs plotted versus calculated vitrinite reflectance. Leaky system case is for  $ESPC = 2 \times 10^{-7} \text{ Pa}^{-1}$  and  $KPRES = 1 \times 10^{-20}$ .

Figure 61. Calculated and measured values of saturate content of extracts from the La Luna source rock plotted versus calculated vitrinite reflectance. Leaky system case uses parameters of Fig. 60.

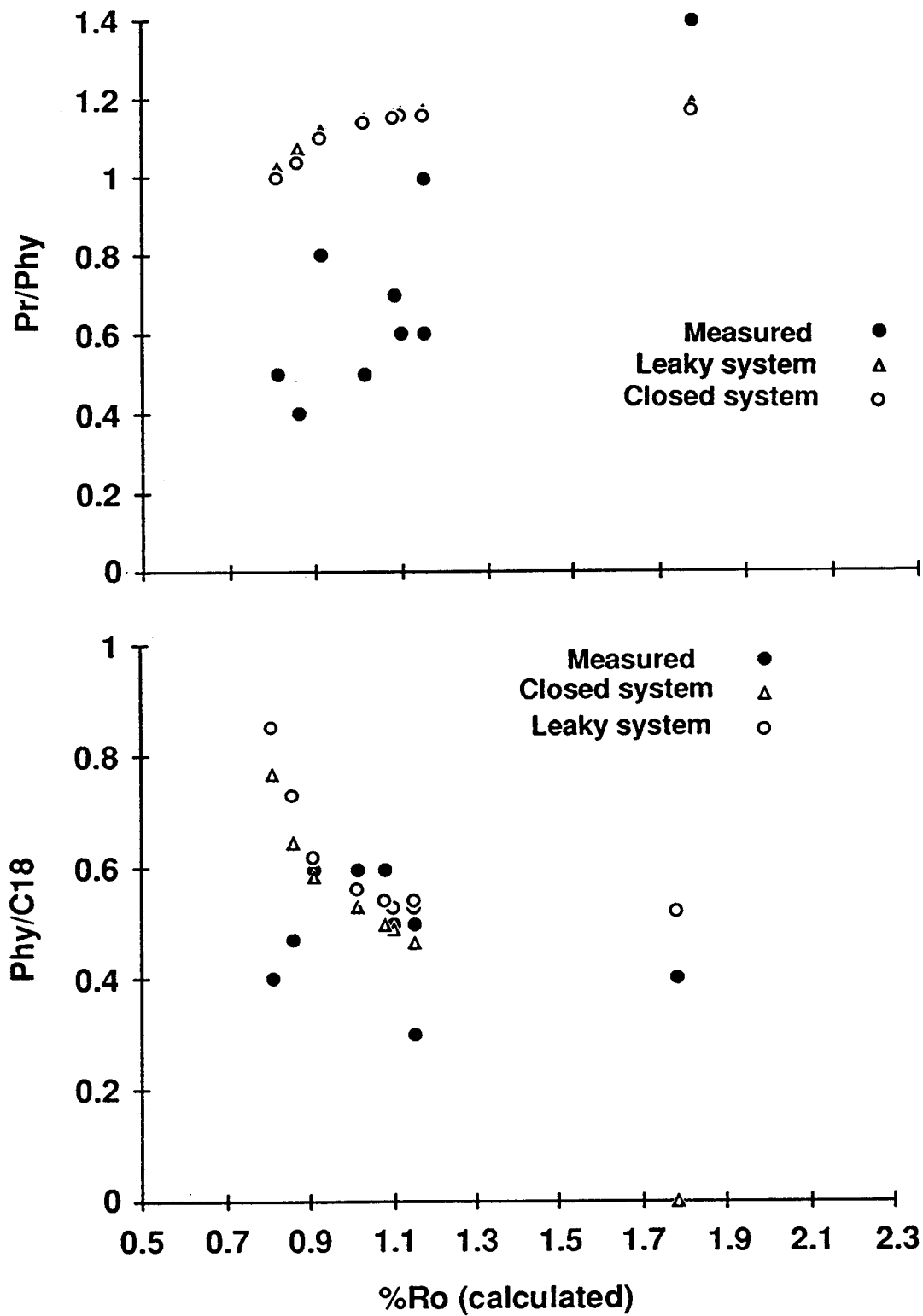


Figure 62. Comparison of calculated and measured values of the pristane/phytane and phytane/C<sub>18</sub> ratios of oils from Cretaceous reservoirs plotted versus calculated vitrinite reflectance. Leaky system case uses parameters of Fig. 60.

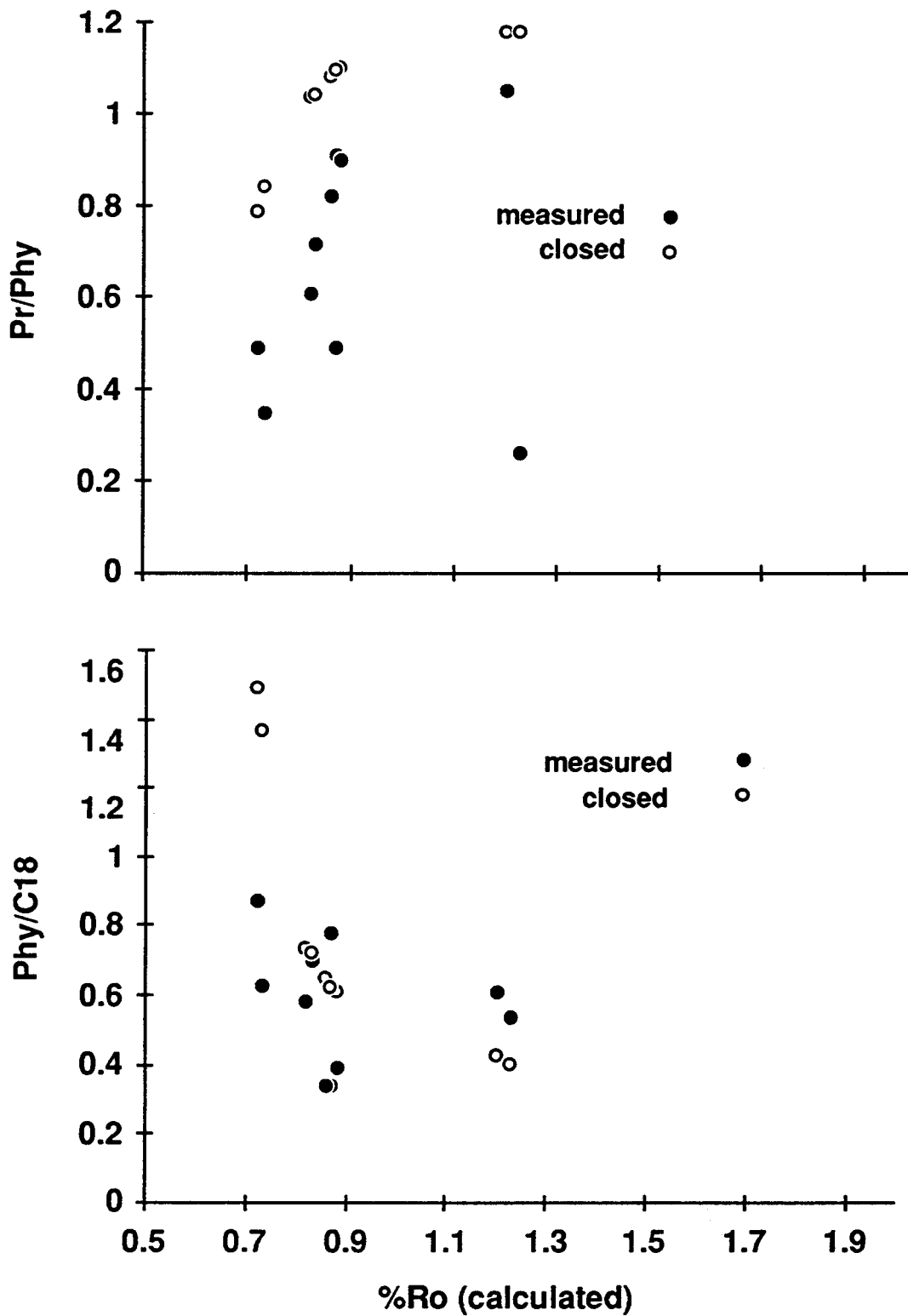


Figure 63. Comparison of calculated and measured values of the pristane/phytane and phytane/C<sub>18</sub> ratios of extracts from the La Luna source rock plotted versus calculated vitrinite reflectance.

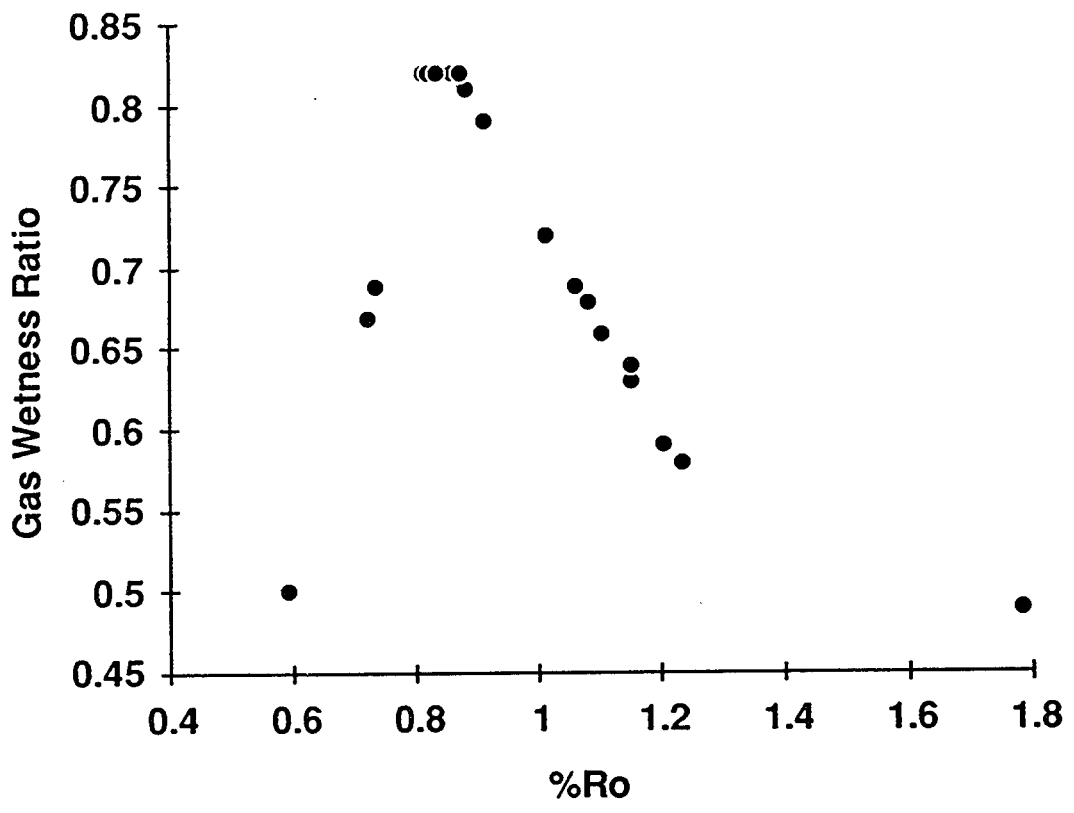


Figure 64. Calculated gas wetness ratio versus calculated vitrinite reflectance for all of the wells modeled with PMOD.

ANNEX XII  
OF THE  
IMPLEMENTING AGREEMENT  
BETWEEN  
THE DEPARTMENT OF ENERGY OF THE UNITED STATES OF AMERICA  
AND  
THE MINISTRY OF ENERGY AND MINES OF THE REPUBLIC OF VENEZUELA  
IN THE AREA OF  
G E O C H E M I S T R Y

WHEREAS, the United States Department of Energy (hereinafter referred to as DOE) and the Ministry of Energy and Mines of Venezuela (hereinafter referred to as MEMV) desire to cooperate in the field of energy research and development;

WHEREAS, in the furtherance of their mutual interest DOE and MEMV entered into the Agreement in the field of Energy Research and Development signed March 6, 1980 (hereinafter referred to as the Energy R&D Agreement);

WHEREAS, DOE and MEMV have a mutual interest in technology exchange on the prediction of petroleum occurrence;

WHEREAS, DOE and MEMV have a mutual interest in improving their present modeling capability to predict the occurrence of petroleum from the thermal maturation of kerogen bearing source rocks in geologic formations;

WHEREAS, Venezuelan basins are known to be prolific petroleum producing areas and therefore prime candidates for source rock maturation and petroleum occurrence studies;

It is agreed as follows:

Article 1

In accordance with Article V of the Energy R&D Agreement, the Venezuelan representatives of the Steering Committee have designated INTEVEP, S.A. to act

on behalf of MEMV under this Implementing Agreement. INTEVEP and DOE shall be hereinafter referred to as the Parties to this Implementing Agreement. The Assistant Secretary for Fossil Energy shall be primarily responsible for the programmatic aspects of this Implementing Agreement for DOE. Lawrence Livermore National Laboratory shall carry out DOE's technical responsibilities under Paragraphs B, C, D, E and F of Article 2 of this Implementing Agreement. Each Party shall designate one Project Manager for this Implementing Agreement; the Project Managers shall provide technical management and coordination of the tasks described in this Implementing Agreement.

## Article 2

The Parties shall cooperate in research in the area of petroleum generation in the Maracaibo Basin as set forth below:

INTEVEP and LLNL shall perform a series of tasks over an initial period of 18 months. Further work may be required to complete all tasks at the end of the initial 18 month period. Any further work will be the subject of a further Amendment and Extension to this Annex XII.

### A. INTEVEP Experimental Tasks

#### Task 1: Sealed-Bomb Pyrolysis

INTEVEP shall perform several sealed-bomb pyrolysis experiments using La Luna Shale samples from the Maracaibo Basin. The heating temperatures and times shall be chosen so that, at the lowest extreme, the conversion of kerogen to bitumen and gas is less than 25% of the kerogen, and the highest extreme, at least 75% of the generated oil is cracked to gas. Data and results shall be recorded and bitumen, oil and gas samples taken for further analysis.

#### Task 2: Simulated Distillation, GC-MS, C13 NMR Analysis

INTEVEP shall perform simulated distillation, gas chromatography-mass spectrometry and carbon isotope 13 nuclear magnetic resonance analyses on the various oil and bitumen products resulting from Task 1. Data and results shall be recorded for use in pyrolysis interpretation and modeling.

#### Task 3: GPC Analysis

INTEVEP shall perform gel permeation chromatography analysis on bitumen products resulting from Task 1. Data results shall be recorded for use in pyrolysis interpretation and modeling.

## B. LLNL Experimental Tasks

### Task 1: High Pressure Pyrolysis

LLNL shall perform high pressure pyrolysis experiments of the Burnham and Singleton type on La Luna shale samples provided by INTEVEP. The tests will be conducted in a self purging reactor at 2 different pressures and 3 different heating rates. Oil and gas evolution rates will be measured for use in determining oil and gas evolution kinetics. INTEVEP personnel shall participate in acquiring the data and information.

### Task 2: FIMS Analysis

LLNL shall acquire field ionization mass spectrometry analysis on extracted bitumen samples from Task A1 to determine molecular weight distributions. Part of the task shall be accomplished by subcontract to a laboratory with specialized expertise in FIMS analysis. The data and results will be used to determine stoichiometric coefficients in pyrolysis modeling.

### Task 3: Gas Evolution Kinetics

LLNL shall perform gas evolution rate experiments on samples of La Luna shale, isolated kerogens and bitumen intermediates. Individual gas species will be identified using an on-line mass spectrometer. The data will be analyzed and rate expressions developed for the gas generation reactions. Gas samples will be taken and provided to INTEVEP for isotope analysis. INTEVEP personnel will participate in the experimentation.

## C. Interpretation of the Pyrolysis Results

INTEVEP and LLNL shall jointly combine the results from paragraphs A and B and develop a numerical model of the pyrolysis chemistry to run on a VAX or equivalent computer. Modification of the existing LLNL general pyrolysis model for Green River shale will be attempted to describe pyrolysis of the La Luna shale. If successful, the general model will be used to check results of the less complex VAX model. If modification of the general model for La Luna shale is not routinely accomplished further effort and funds will be required. Further work requirements will be proposed at the discretion of the INTEVEP and LLNL Project Manager and subject to approval by the Steering Committee.

## D. Calculation of Pore Pressures

LLNL shall determine a method to calculate pore pressures that are generated by hydrocarbon maturation and shall incorporate the appropriate equations into the general pyrolysis model. Solubilities and densities as a function of

temperature and pressure will be estimated from literature data. The model will then be used to calculate over-pressured zones and primary migration fractions. Further work may entail comparisons with field data, and additional experiments may be required. Further work will be proposed at the discretion of the Project Managers and subject to approval by the Steering Committee.

#### E. Determination of Sulfur Reactions

LLNL shall examine the literature on sulfur chemistry and combine the information obtained with data paragraphs A and B to determine the possibility of developing kinetic models for the fate of sulfur compounds underground. Additional experiments will be devised that would further define sulfur compound reaction during oil and gas generation. Completion of this work will likely require further effort. Further work will be proposed at the discretion of the Project Managers and subject to Steering Committee approval.

#### F. Application to Geologic Basins

INTEVEP and LLNL shall jointly determine a thermal history for the Maracaibo Basin and compute hydrocarbon characteristics in the various parts of the Basin. Using corehole data supplied by INTEVEP, LLNL and INTEVEP personnel will jointly compare model predictions with hydrocarbon characteristics observed in the Basin. Completion of this work will likely require further effort. Further work will be proposed at the discretion of the Project Managers and subject to approval by the Steering Committee. All work under Paragraphs A and B is anticipated to be completed by the end of the first year of the project. Work under Paragraphs C, D, E and F will extend, at minimum, 6 months into year two of the project. Technical reports on the tasks of this Implementing Agreement will be issued by the party or parties concerned every four months which will include experimental conditions, raw laboratory data or other supporting data and their interpretation with the details of computer programs and/or physical or chemical model used. The Project Managers will report to the Steering Committee at the end of year one and propose the effort in man-years and funds required of the participants to complete the project.

#### Article 3

- A. The performance of Article 2, Paragraph A, will be by INTEVEP and all costs pertaining to Paragraph A, including approximately 1700 man-hours of personnel effort, will be borne by INTEVEP.
- B. The performance of Article 2, Paragraphs B, D, and E will be done by LLNL and all costs, including approximately 4000 man-hours of personnel effort, pertaining to Paragraphs B, D and E will be borne by DOE, with the

exception of shipping costs for any shale, bitumen or oil samples required, and the expenses of any visiting INTEVEP personnel, which will be borne by INTEVEP. Obtaining and shipping the samples from Venezuela to Livermore, CA, will be the responsibility of INTEVEP.

C. The costs of performing joint tasks C and F shall be borne as follows:

1. INTEVEP Costs. INTEVEP shall provide approximately 1300 man-hours of INTEVEP personnel effort for Paragraph C work and approximately 1900 man-hours of INTEVEP personnel effort for Paragraph F work.
2. DOE Costs. DOE shall provide approximately 900 man-hours of LLNL personnel effort for paragraph C work and approximately 1000 man-hours of LLNL personnel effort for Paragraph F work.
3. Other costs. Further work in addition to the above listed man-hours and financial contributions may be required to complete Paragraphs C through F. Any additional completion costs shall be identified by the Project Managers and proposed to the Steering Committee for approval at the end of the first year of the project.

#### Article 4

The Parties shall support the widest possible dissemination of information arising from this Implementing Agreement in accordance with Article 2 of the Annex to the Energy R&D Agreement. If a Party has access to proprietary information as defined in Article 2 of the Annex to the Energy R&D Agreement which would be useful to the activities under this Implementing Agreement, such information shall be accepted for the task only on terms and conditions as agreed in writing by the Parties.

#### Article 5

Rights to any invention or discovery made or conceived in the course of or under this Implementing Agreement shall be distributed as provided in Paragraph 1 of Article VI of the Energy R&D Agreement. As to third countries, rights to such inventions shall be decided by the Joint Steering Committee.

Each Party shall take all necessary steps to provide the cooperation from its inventors required to carry out this Article. Each Party shall assume the responsibility to pay awards to compensation required to be paid to its own nationals according to its own laws.

#### Article 6

The existing terms and conditions of the Energy R&D Agreement shall continue and remain in full force and effect notwithstanding the terms of this Annex XII.

Article 7

This Annex XII to the Implementing Agreement shall enter into force upon the later date of signature and shall remain in force for a period of 18 months. It may be amended or extended by mutual written consent of the Parties in accordance with Article V of the Energy R&D Agreement.

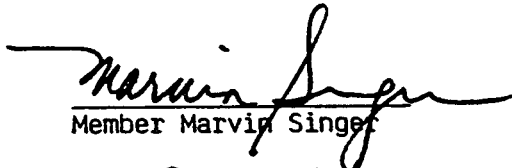
Article 8

This Annex XII may be terminated at any time at the discretion of either Party, upon six (6) months advance notification in writing to the other Party by the Party seeking to terminate. Such termination shall be without prejudice to the rights which may have accrued under this Annex XII to either Party up to the date of such termination.

Done in Washington, D.C., USA.

THE JOINT STEERING COMMITTEE

On behalf of DOE

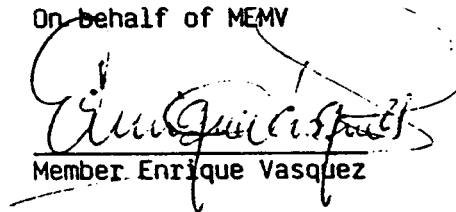
  
Member Marvin Singer

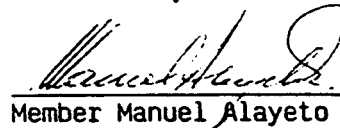
  
Member George Stosur

  
Member Robert Folstein

Aug 14, 1987  
Date

On behalf of MEMV

  
Member Enrique Vasquez

  
Member Manuel Alayeto

  
Member Pedro Diaz

Aug. 14 / 87  
Date

## APPENDIX II: THEORETICAL CONSIDERATIONS FOR PMOD

### Chemical reaction mechanism:

PMOD can handle diverse types of chemical reaction models. The choice of which model to use out of the many possible depends on both the preference of the user and the detail of chemical compositional information desired for a particular purpose. For example, will the mechanism include a chemically distinct bitumen entity related to partial kerogen decomposition, or will bitumen be treated as unexpelled oil? Will the oil contain different fractions, and if so, will they be based on chemical-type properties, boiling-point properties, or both? Will the gas contain separate species for methane and wet gas components and will it contain heteroatomic species? Examples of different types of mechanisms are given in Table II-1. These reaction mechanisms are used singly or in combination to build up more complicated mechanisms for the complete reaction network. Stoichiometry coefficients are calculated for each user-specified reaction by requesting further information about mole ratios of products.

Table II-1. Chemical mechanisms that can be modeled with PMOD

<p><b>Parallel Mechanism:</b></p> <pre> precursor 1  →  product type 1 precursor 2  →  product type 2 precursor 3  →  product type 3                     </pre>	<p><b>Simple Example:</b></p> <pre> heavy oil potential  →  heavy oil light oil potential  →  light oil gas potential        →  gas                     </pre>
<p><b>Serial Mechanism:</b></p> <pre> starting material  →  primary products primary products  →  secondary products secondary products →  tertiary products                     </pre>	<p><b>Simple Example:</b></p> <pre> kerogen → oil + gas + residue oil     → gas + residue residue → gas + inert carbon                     </pre>
<p><b>Synthesis Mechanism:</b></p> <pre> ∑ kerogen element i  →  product j etc.                     </pre>	<p><b>Simple Example:</b></p> <pre> kerogen C + kerogen O  →  CO<sub>2</sub> kerogen C + kerogen H  →  CH<sub>4</sub> kerogen H + kerogen S  →  H<sub>2</sub>S                     </pre>
<p><b>Competing Pathways:</b></p> <pre> starting material  →  intermediate                     ↙   ↘                     products                     </pre>	<p><b>Simple Example:</b></p> <pre> kerogen → bitumen          ↙   ↘          oil + gas + residue                     </pre>

All reactions are assumed to be independent of pressure and have their temperature dependence described by the Arrhenius equation,

$$k = A e^{-E/RT}$$

The rate expression for a reaction with a single reactant is of the form

$$\partial W_i / \partial t = -k_j W_i,$$

where a solid or fluid species  $i$  is the reactant in reaction  $j$ . These partial derivatives and the known mass stoichiometry coefficients for the reactions are then used, along with expulsion rates, to formulate the complete derivative for the species remaining in the rock and the species expelled from the rock. The complete set of ordinary differential equations, including equations for pressure and porosity, are numerically integrated by LSODE, the Livermore Solver for Ordinary Differential Equations (Hindmarsh, 1980). The equations explicitly observe only mass balance, but the \*.KEM files developed with the KEMMOD program also implicitly satisfy elemental balance. It is possible by using a text editor to create \*.KEM files that consider mass balance only, but we do not recommend this practice.

#### **Rock Eval simulation:**

PMOD can simulate Rock Eval analysis of the remaining material at specific times during a run. Either a rigorous or an approximate Rock Eval calculation can be done. A rigorous Rock Eval simulation is always done for output to the PRN file, but it is done for output to the PLT file only when parameter NTMAX = 1 in the MIS file. To account for serial reaction effects, the rigorous simulation is done by numerically integrating the rate equations. This is a time-intensive calculation, since it is tantamount to doing a separate, full PMOD run within the main run each time the rigorous Rock Eval output is wanted. When NTMAX = 0, only the quicker, approximate Rock Eval calculation is done for output to the PLT file.

In a rigorous simulation, the remaining material is heated from 300 to 625 °C at 25 °C/min and the rates and integrals of hydrocarbon evolution are calculated. From this, S1, S2, S2CH4, TMAX, and TMAXCH4 are obtained. S1 consists of the volatile oil present and S2 consists of the volatile oil potential and the hydrocarbon gas potential from the solid organic matter and from any non-volatile oil reactants. Oil volatility factors in the FIZ file are used in these calculations.

In an approximate Rock Eval calculation, S1 again consists of the volatile oil present, but S2 is only estimated from the stoichiometry coefficients of the reaction network without a detailed integration of the reaction rates. We include contributions to S2 from KER\* species and non-volatile oil reactants. We exclude any possible contributions from any RES\* species, since without a detailed rate calculation the extent of its pyrolysis

is unknown. No estimates are made for S2CH4, TMAX, or TMAXCH4 and the nonappearance of these items in the plotting menu, when PLOTMOD is later executed, indicates that the other Rock Eval parameters were determined by the approximate calculation. Furthermore, the approximate S2 will be set to zero if Rock Eval analysis of extracted material is requested or if an oil volatility factor or extractability factor other than 1 is used for any oil species, as indicated by the appearance of only the S1 Rock Eval parameter in the plotting menu.

When possible, several Rock Eval diagnostics are calculated from S1, S2, TOC, and their derivatives. When unextracted material is specified for the Rock Eval calculation, the hydrogen index is

$$HI = S2/TOC,$$

the production index is

$$PI = S1/(S1 + S2),$$

the petroleum expulsion efficiency is

$$PEE = (S2_0 - S2 + S1_0 - S1)/(S2_0 - S2 + S1_0),$$

an estimation of the TOC at zero time is

$$TOC_0 = TOC + 0.00083(S2_0 - S2 + S1_0 - S1),$$

and the transformation ratio is

$$TR = 1200(HI_0 - HI)/[HI_0(1200 - HI)].$$

In the above equations, TOC is the organic carbon in the solid organic matter and oil at the start of the Rock Eval calculation and the subscript *o* refers to zero time of compaction and expulsion.

When extracted material is specified for the Rock Eval calculation, the hydrogen index is

$$HI = S2/TOCIOM,$$

where TOCIOM is the organic carbon in the solid organic matter and oil, but only in proportion to the non-extractability factor (1 - extractability) for each oil species. In this case, no estimates are made for PI, PEE, or TOC<sub>0</sub>.

### Compaction:

The porosity of compacting sediments can be estimated from the Athy equation (Athy, 1930)

$$\epsilon_A = \epsilon_o \exp(-KZ)$$

or from the effective stress (Hubbert and Rubey, 1959)

$$\epsilon_{eff} = \epsilon_o \exp[-K_e(P_L - P)].$$

In the absence of overpressuring, these two equations are identical. We wish to allow overpressuring for one of our system configurations, but the latter equation would be valid for the complete burial history only if both compaction and decompaction were allowed to occur to the full extent stated by the equation. It would not be realistic, however, to allow decompaction to occur to a greater extent than the creation of new porosity from the disappearance of solid material by pyrolysis reactions.

In PMOD, porosity is therefore calculated by integrating the rate of porosity change over the burial history. For normal burial, the rate is usually described by the derivative of  $\varepsilon_{eff}$ , namely

$$\dot{\varepsilon}_{eff} = -\varepsilon K_{\varepsilon} (\dot{P}_L - \dot{P}).$$

However, the decompaction constraint mentioned in the preceding paragraph implies that any positive rate of change of the porosity of the source rock,  $\dot{\varepsilon}$ , should be limited by the rate of change of porosity due to disappearance of organic and inorganic solid material,

$$\dot{\varepsilon}_{sol} = -\rho \left( V_{sj} \sum \dot{W}_{sj} + \dot{V}_{sj} \sum W_{sj} + V_{si} \sum \dot{W}_{si} \right).$$

The specific volume of the inorganic matter is assumed to be constant at the user input value, while the specific volume of the organic matter and its rate of change are calculated from an empirical function of the hydrogen content. The rates of disappearance of inorganic and organic solids ( $\dot{W}_{si}$  and  $\dot{W}_{sj}$ , respectively) are obtained from the chemical reaction rates. To determine whether  $\dot{\varepsilon}_{sol}$  or  $\dot{\varepsilon}_{eff}$  is the correct rate of change of porosity to use in advancing porosity to the next time step, the integrated porosity ( $\varepsilon$ ) at any given time must be compared with the *target* porosity ( $\varepsilon_{eff}$ ) at that time. If  $\varepsilon < \varepsilon_{eff}$ , then  $\dot{\varepsilon} = \dot{\varepsilon}_{sol}$ . If  $\varepsilon \geq \varepsilon_{eff}$ , then the magnitudes of  $\dot{\varepsilon}_{eff}$  and  $\dot{\varepsilon}_{sol}$  must be compared. That is, if  $\dot{\varepsilon}_{eff} > \dot{\varepsilon}_{sol}$ , then  $\dot{\varepsilon} = \dot{\varepsilon}_{sol}$ , otherwise  $\dot{\varepsilon} = \dot{\varepsilon}_{eff}$ .

### Expulsion:

There are four options for the expulsion model, defined by the system configuration parameter ISYS. Modeling laboratory pyrolysis will usually use the simple open system (ISYS = 1 or closed system ISYS = 2). Modeling geological conditions will usually use one of the compaction/expulsion options (ISYS = 3 or 4). Although ISYS = 1 or 2 can also be used for geological heating rates, they do not consider compaction.

Before discussing the two compaction/expulsion models in detail, the following points regarding the open and closed system models should be noted. These are both very simple models. The closed system model does not do a complete closed system

calculation, since it does not calculate pressure. To the extent that the chemical reactions are independent of pressure, the results should still be meaningful. The open system model calculates the amount of fluid expulsion by considering any gas product and volatile portion of any oil product (defined by the volatility factors) to be immediately expelled. Only the solid species and non-volatile portions of oil continue to react. Thus, the reaction of volatile pore fluids is not taken into account, but this should be relatively insignificant. Alternative ways of calculating the open and closed systems are discussed more in connection with the compaction/expulsion models.

Two compaction/expulsion models are available: ISYS = 3 uses constant fluid densities that are input by the user, and ISYS = 4 uses an equation of state to calculate fluid densities as a function of temperature, pressure, and composition. Both models are based on volume conservation, but only ISYS = 4 calculates overpressuring.

For the simpler model (ISYS = 3), the rate of fluid expulsion is solved from the volume conservation equation:

$$R_E = \frac{\dot{\epsilon}}{\rho} \left( \frac{1}{1 - \epsilon} \right) + \dot{N}_1 V_1 + \dot{N}_2 V_2,$$

where  $\dot{N}_1$  and  $\dot{N}_2$  are obtained from the chemical reaction rates.  $R_E$  is then partitioned between the fluid phases in proportion to the normalized relative permeability to viscosity ratios of each phase.

For the more rigorous model (ISYS = 4), the rate of expulsion of each fluid phase is determined by the excess pore pressure:

$$R_{Ei} = \frac{K_P}{\rho} (P - P_H) \frac{r_i}{\mu_i}$$

and the total rate of fluid expulsion is then

$$R_E = \sum R_{Ei}.$$

For this model we use the volume conservation equation

$$\frac{\dot{\epsilon}}{\rho} \left( \frac{1}{1 - \epsilon} \right) + \dot{N}_1 V_1 + N_1 \dot{V}_1 + \dot{N}_2 V_2 + N_2 \dot{V}_2 - R_E = 0,$$

along with the equations of state for the fluid phases to determine the pore pressure and the specific volumes of each phase. The derivatives  $\dot{V}_1$  and  $\dot{V}_2$  are needed, since the specific volumes are not constant for this model.

Before discussing the equations of state, it should be pointed out that the calculated rate of expulsion for ISYS = 4 is subject to a fracture criterion; namely, the pore pressure is not permitted to exceed the fracture pressure. The fracture pressure is a user-supplied fraction (FLITH) of the lithostatic pressure, which is a user-supplied factor (RLITH) times the known hydrostatic pressure. If the pore pressure becomes equal to the fracture pressure, the calculated rate of expulsion is increased sufficiently to keep the pore pressure from exceeding the fracture pressure.

An empirical equation of state was derived for water by simultaneous linear regression on specific volume, isothermal compressibility, and isobaric thermal expansivity. Specific volume data for pure water (Kennedy and Holser, 1966) were used in the regression and were numerically differentiated to obtain the compressibility and expansivity values. The derived equation for specific volume is

$$V_1 = 0.001 + T_c^2(a + bP^2) + P(c + dT_c^3),$$

where  $a = 3.85 \times 10^{-09}$ ,  $b = 3.45 \times 10^{-26}$ ,  $c = -4.32 \times 10^{-13}$ , and  $d = -5.42 \times 10^{-20}$ . This equation is valid for temperatures from 25 to 250 °C and for pressures from 0.1 to 160 MPa. The agreement between measured and calculated specific volume and thermal expansivity are shown in Figure II-1. Good agreement was also obtained for compressibility.

A modified Redlich-Kwong-Soave equation of state (Soave, 1972; Pénélox, *et al.*, 1982) is used for the organic fluid.

$$P = \frac{RT}{V - b + c} - \frac{a}{(V + c)(V + b + c)}.$$

Parameters  $a$ ,  $b$ , and  $c$  are functions of the following properties of each species in the organic fluid: molecular weight, critical temperature and pressure, acentric factor, and Rackett compressibility factor. Default values for these properties are taken from Braun and Burnham (1990). The molecular weight default values that you will see displayed when making a FIZ file may vary from these, since they depend on the assigned elemental compositions of the species. We often override the critical temperature of CH<sub>4</sub> (190 K) with a higher value (*e.g.*, 370). Using the correct value, in expulsion runs having CH<sub>4</sub> as the principal species remaining after pyrolysis and expulsion is largely completed can cause the numerical integration to proceed very slowly (*e.g.*, at temperatures above 200 °C for geological heating rates). In such runs, using the higher value of 370 K for the critical temperature of CH<sub>4</sub> reduced the execution time by a factor of 3 or more without significantly changing the results.

Relative permeabilities and viscosities are used in both the RKS and the constant-fluid-density expulsion models. Three parameters for each fluid phase are used in calculating the relative permeabilities: (1) water saturation below which the relative permeability is zero (for the aqueous phase) or one (for the non-aqueous phase), (2) water saturation above which the relative permeability is one (for the aqueous phase) or zero (for the non-aqueous phase), and (3) shape of the relative permeability curve between those two limits (1=linear, 2=parabolic, 3=cubic, ...). Figure II-2 shows the relative permeability curves using different limits for each phase.

Empirical viscosity equations were developed for the aqueous and organic fluid phases. The aqueous viscosity is assumed to be only a function of temperature and was derived from viscosity data for 5% brine (Archer and Wall, 1986):

$$\mu_1 = 1.932 \times 10^{-5} \exp(1072/T).$$

The pressure correction for water viscosity is small and was ignored.

The viscosity of the organic fluid phase is taken to be the mass-weighted arithmetic mean of the oil components and the gas components:

$$\mu_2 = f_g \mu_g + f_o \mu_o,$$

where  $\mu_g$  has a constant value of  $3 \times 10^{-5}$  (Pa·s) and  $\mu_o$  is an empirical fit of gas-free crude oil viscosity data (Beal, 1946) as a function of temperature and pressure:

$$\mu_o = \left[ \frac{8 \times 10^5}{(1.051 - \rho_o)^2} \right] \exp(8000\rho_o^4/T - \rho_o/0.024)(1 + 10^{-8}P).$$

The agreement between measured and calculated oil viscosity is shown in Figure II-3. The oil specific gravity at STP,  $\rho_o$ , is calculated from the composition of the oil remaining in the rock at any given time and from the known STP specific gravities for the oil species.

The *leaky* system configuration (ISYS = 4) should also be useable for modeling open or closed systems. By making  $K_p^o$  relatively large (*e.g.*,  $1 \times 10^{-12}$ ) compared to the normal value ( $1 \times 10^{-20}$ ), an open system should be approximated more correctly than done by ISYS = 1. Too large a value, however, will make the system of equations too stiff to solve with a reasonable computer execution time. Conversely, by making  $K_p^o$  smaller, a lower expulsion rate is be obtained. Using  $K_p^o = 0$  should simulate a closed system more correctly than done by ISYS = 2, but we have not yet fully tested that approach.

## NOMENCLATURE

$A$	frequency factor ( $s^{-1}$ )
$E$	activation energy (cal/mol)
$f_g$	mass fraction of gas components in organic fluid
$f_o$	mass fraction of oil components in organic fluid
$K$	depth coefficient of porosity ( $m^{-1}$ )
$K_\epsilon$	pressure coefficient of porosity ( $Pa^{-1}$ )
$K_P$	effective hydraulic conductivity
$K_P^\circ$	hydraulic conductivity coefficient
$N_i$	quantity of fluid phase $i$ (kg fluid/kg rock)
$P$	pore pressure (Pa)
$P_H$	hydrostatic pressure (Pa)
$P_L$	lithostatic pressure (Pa)
$r_i$	relative permeability for fluid phase $i$
$R_E$	total rate of fluid expulsion ( $m^3$ fluid/kg rock·s)
$R_{Ei}$	rate of expulsion of fluid phase $i$ ( $m^3$ fluid/kg rock·s)
$T$	temperature (K)
$T_c$	temperature ( $^{\circ}C$ )
$V_i$	specific volume of fluid phase $i$ ( $m^3$ fluid/kg fluid)
$V_{si}$	specific volume of solid inorganic species $i$ ( $m^3$ solid/kg solid)
$V_{sj}$	specific volume of solid organic species $j$ ( $m^3$ solid/kg solid)
$W_{fi}$	quantity of fluid species $i$ (kg fluid species/kg rock)
$W_{si}$	quantity of solid inorganic species $i$ (kg solid species/kg rock)
$W_{sj}$	quantity of solid organic species $j$ (kg solid species/kg rock)
$Z$	depth (m)

### Greek

$\epsilon$	porosity ( $m^3$ pore volume/ $m^3$ rock)
$\epsilon_{eff}$	target porosity ( $m^3$ pore volume/ $m^3$ rock)
$\mu_i$	viscosity of fluid phase $i$ (Pa·s)
$\mu_g$	viscosity of gas components of organic fluid phase (Pa·s)
$\mu_o$	viscosity of oil components of organic fluid phase (Pa·s)
$\rho$	bulk density of dry, unreacted rock (kg rock/ $m^3$ rock)
$\rho_o$	specific gravity of oil at STP

## REFERENCES

- Archer, J. S.; Wall, C. G. (1986) *Petroleum Engineering Principles and Practice*, Graham and Trotman Inc., Gaithersburg, MD.
- Athy, L. F. (1930) *Am. Assoc. Petroleum Geologists Bull.* **14**, 1–24.
- Beal, C. (1946) *Trans. AIME*, **13**, 94–115.
- Bjorøy, M.; Williams, J. A.; Dolcater, D. L.; Winters, J. C. (1988) *Org. Geochem.*, **13**, 901–913.
- Braun, R. L.; Burnham, A. K. (1988) *Lawrence Livermore Nat. Lab. Report UCID-21507*.
- Braun, R. L.; Burnham, A. K. (1990) *Energy & Fuels*, **4**, 132–146.
- Braun, R. L.; Burnham, A. K.; Reynolds, J. G.; Clarkson, J. E. (1991) *Energy & Fuels*, **5**, 192–204.
- Burnham, A. K. (1989) *Lawrence Livermore Nat. Lab. Report UCID-21665*.
- Burnham, A. K.; Braun, R. L.; Sweeney, J. J.; Reynolds, J. G.; Talukdar, S.; Vallejos, C. (1991) *Lawrence Livermore Nat. Lab. Report*, to be published.
- Burnham, A. K.; Sweeney, J. J. (1990) *Lawrence Livermore Nat. Lab. Report UCRL-102602 Rev. 1*, submitted for publication in the *Handbook of Petroleum Geology*.
- Espitalié, J.; Ungerer, P.; Irwin, I.; Marquis, F. (1988) *Org. Geochem.*, **13**, 893–899.
- Hindmarsh, A. C. (1980) *ACM-SIGNUM Newsl.*, **15**, 10–11.
- Hubbert, M. K.; Rubey, W. W. (1959) *Geol. Soc. America Bull.* **70**, 115–166.
- Kennedy, G. C.; Holser, W. T. (1966) In *Handbook of Physical Constants, Revised Edition*; Clark, S. P., Ed.; Geol. Soc. of America, Inc., New York; pp. 371–383.
- Péneloux, A.; Rauzy, E.; Fréze, R. (1982) *Fluid Phase Equilib.*, **8**, 7–23.
- Soave, G. (1972) *Chem. Eng. Sci.*, **27**, 1197–1203.
- Ungerer, P.; Behar, F.; Villalba, M.; Heum, O. R.; Audibert, A. (1988) *Org. Geochem.*, **13**, 857–868.

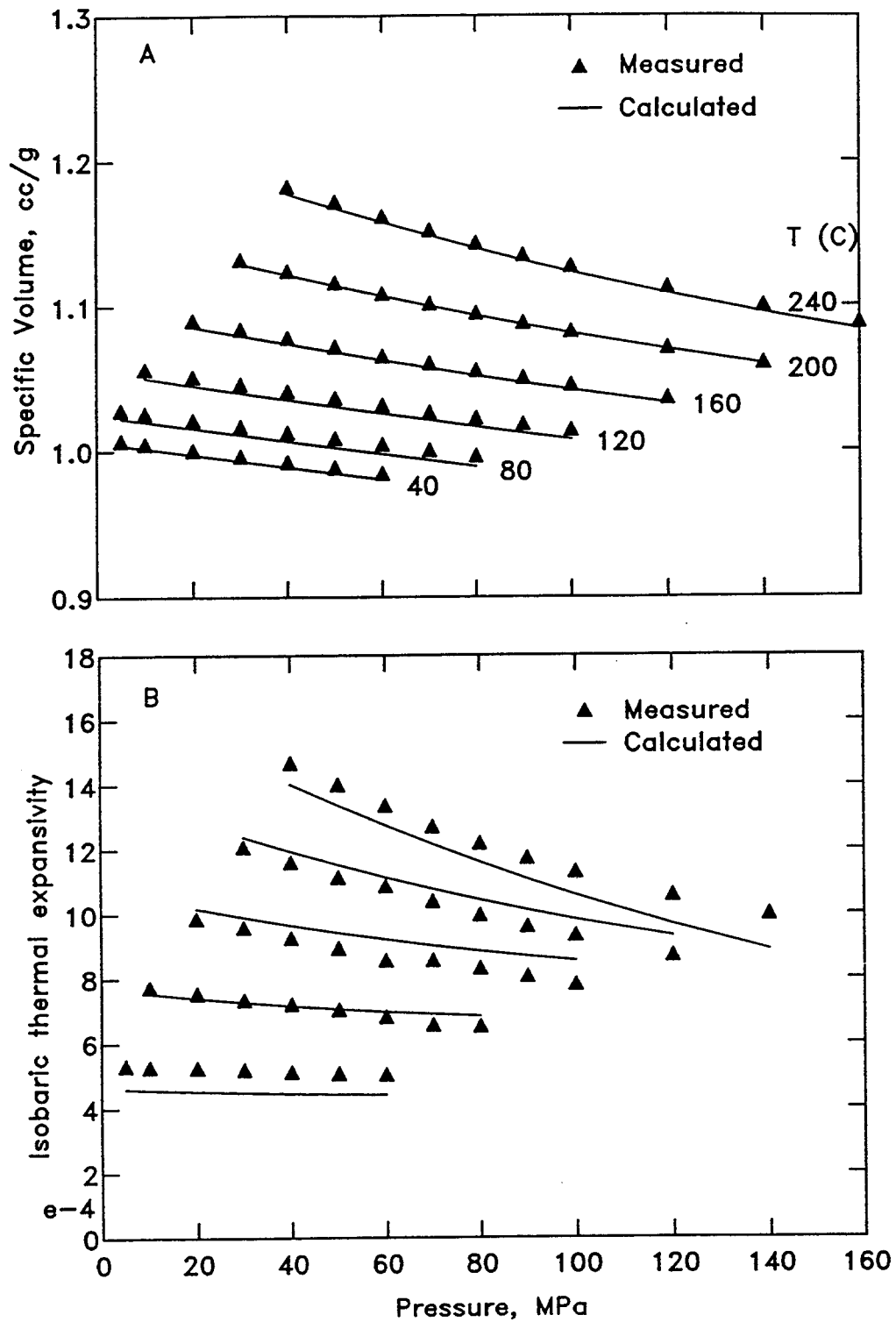


Figure II-1. Comparison of measured specific volume (A) and thermal expansivity (B) with that calculated from an empirical T-P fit (from simultaneous linear regression on specific volume, compressibility, and thermal expansivity).

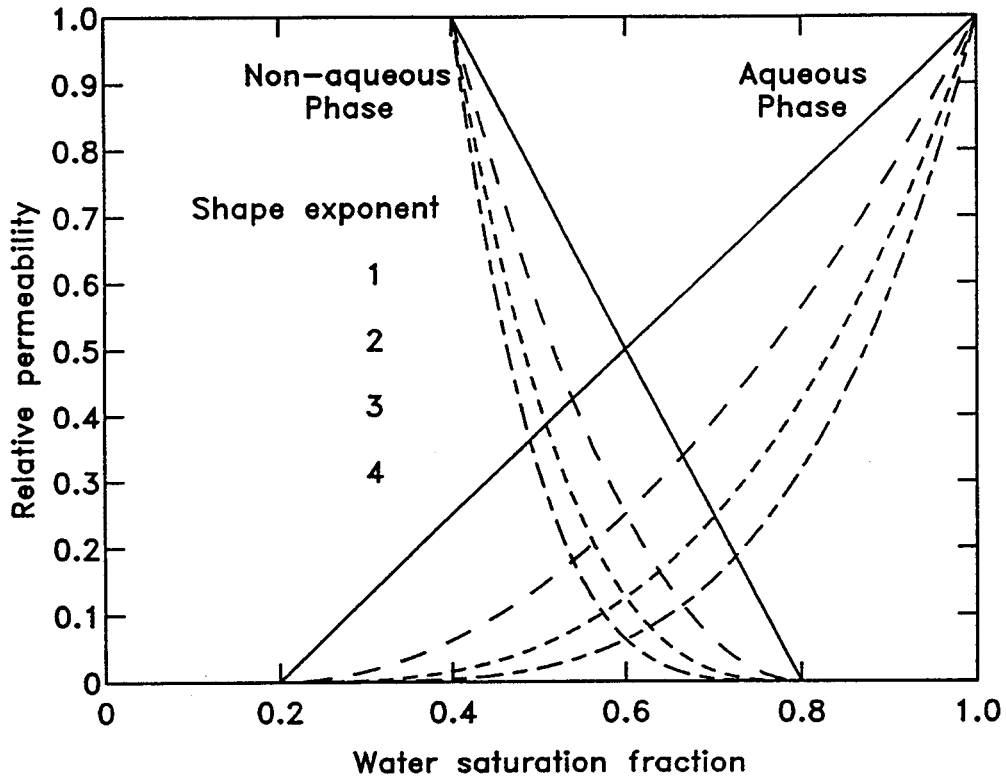


Figure II-2. Relative permeability options for the aqueous and nonaqueous fluid phases. The endpoints and shape of the curve for each phase can be selected.

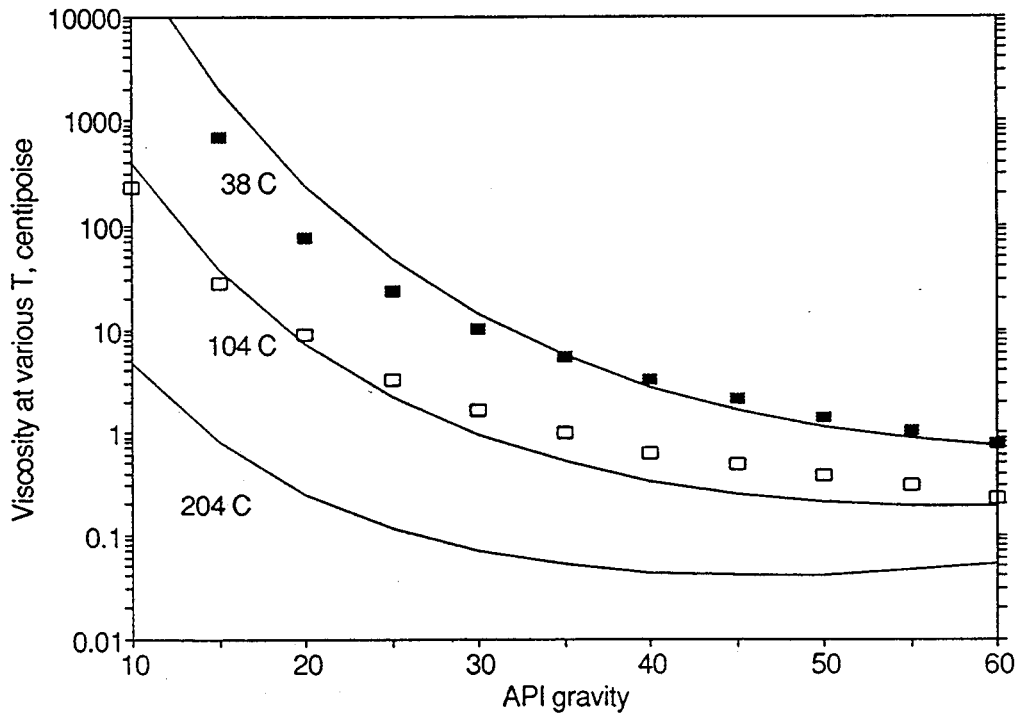


Figure II-3. Comparison of measured viscosity of gas-free crude oil (Beal, 1946) with that calculated from an empirical T-P fit (approximate, not least-squares).









